University of Trieste

35th cycle of PhD Program in Nanotechnology

Oxidizability and catalytic properties of Platinum nanoclusters: unraveling the role of cluster size and type of supporting surface

PhD STUDENT:
Mina Taleblou

PhD SUPERVISOR:
Dr. Simone Piccinin
Dr. Matteo Farnesi Camellone
Dr. Stefano Fabris

PhD COORDINATOR:
Prof. Alberto Morgante

Anno Accademico 2022/2023

Dedication

I would like to dedicate this work to the strongest woman in my life, my mother; for her continuous love and encouragement.

Acknowledgement

I would like to express my gratitude to Simone and Matteo for supervising me for the last three years. I highly appreciate their patience, kindness, and the knowledge they shared with me.

Many thanks to CINECA supercomputer facilities for giving me access to computational resources to accomplish my PhD project.

Thanks to my friends and colleagues for all the care and support. I had a great time with them and learned a lot about different cultures. My love and special thanks to my family, particularly my mother who always believed in me and brightened my life with her unconditional love.

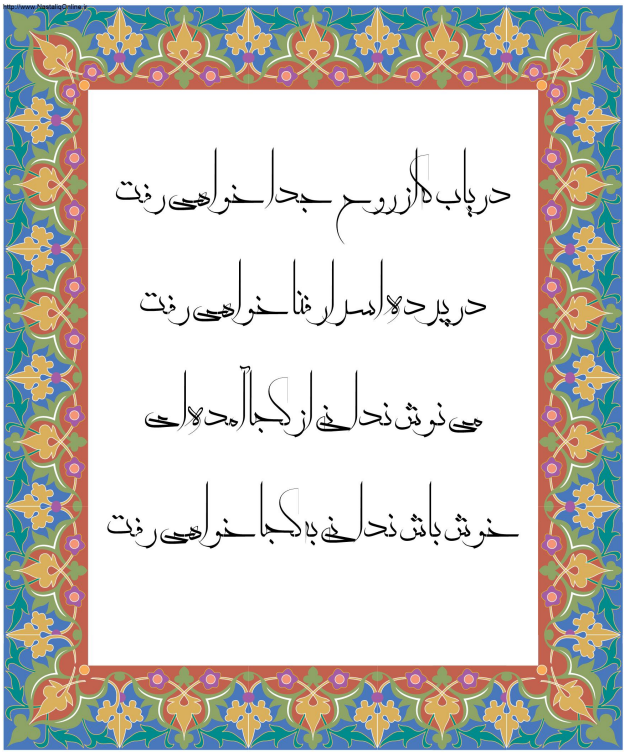

Abstract

This work presents a systematic computational investigation of oxidation and potential catalytic performance of Pt nanoclusters supported on two types of metal oxides. Ab initio calculations were performed based on Density Functional Theory.

Pt nanoclusters in the present work consisted of a few Pt atoms and were simulated both in gas-phase and supported on brookite $TiO_2(210)$ and $Co_3O_4(111)$.

First, the oxidation of free-standing and supported Pt clusters for different sizes was investigated. Gas-phase and supported clusters were found to be more prone to oxidation compared to bulk Pt. A size-dependent oxidation trend was predicted for Pt clusters as a smaller cluster was easier to oxidize, independent of the type of support. The same size-dependent oxidation trend was found for gas-phase and supported Pt clusters.

Next, the oxidation of CO was modeled on Pt clusters to examine the catalytic performance of these systems. Prior to modeling the reaction, we employed ab initio thermodynamics to find the possible oxidation degree of the clusters at the reaction condition. Our calculations showed that from the thermodynamics standpoint, in finite temperatures and pressure of oxygen and carbon monoxide, clusters would be partially oxidized regardless of the type of support. However, the kinetic studies on partially oxidized clusters revealed that they would almost reduce to a more metallic catalyst. Then, we focused on modeling the CO oxidation reaction on metallic clusters and single-atom Pt. To this end, Langmuir-Hinshelwood and Mars-Van Krevelen oxidation mechanisms were simulated on different sizes of Pt catalysts over titanium and cobalt oxide. On brookite, single-atom Pt catalysts, whether anchored on the surface or substituting an atom from the surface lattice, exhibited lower activation energy for converting CO into CO_2. The predicted activation energy was higher on the larger Pt cluster, and the smaller cluster performed even weaker. On the other hand, single-atom Pt on Co_3O_4 was not predicted to be an active catalyst unless it substitutes a Co atom from the surface. This implies the key role of the type of supporting surface in the catalytic properties of the catalyst.

By comparing two oxidation mechanisms on Pt clusters, we concluded that the L-H mechanism is more probable on Co_3O_4 supported Pt clusters rather than TiO_2. However, the MvK mechanism seems to be a more facile oxidation mechanism on adsorbed Pt catalysts on TiO_2. Our findings emphasize the importance of the supporting surface and size of the clusters in the catalytic properties of Pt at subnano scale.

Contents

List of Tables

List of Figures

1 Introduction

Carbon monoxide: Carbon monoxide, CO(g), is a colorless and tasteless gas that can be toxic to humans by entering the lungs; inhaling too much CO can saturate hemoglobin hence it fails in delivering oxygen to the cells.

The current amount of CO in the atmosphere is a result of natural reasons such as bushfires and volcanoes, as well as human activities. A large portion of CO is usually produced by incomplete combustion in vehicles that burn fossil fuels and petrochemical industries; this means insufficient oxygen or too much carbon during the combustion. CO is relatively inert towards oxidation, so the typical lifespan of CO can be up to several months before it reacts with O_2 to form CO_2:

$$2CO(g) + O_2(g) \longrightarrow 2CO_2(g) \tag{1}$$

The reactants of reaction (1) have a total spin of 1 (O_2 is in triplet ground state), but the product (CO_2) has zero spin. So, from an electronic structure standpoint, oxidation of CO is spin-forbidden. This means the reactants and product are in different spin states and this causes a high activation energy [1].

How to oxidize Carbon monoxide? Probably one way to oxidize CO would be increasing the temperature to accelerate the reaction. But a high temperature is not a desirable solution for this problem. The toxic nature of CO prompted immediate research studies to explore methods for oxidizing it at a lower temperature. This means the oxidation of CO should be assisted by a catalyst. Catalysts are functional materials that affect the path and energy profile of a reaction: Catalysts help to initiate or speed up a reaction by decreasing the activation energy. They also affect the direction and selectivity of a reaction. Oxidation of CO into CO_2 is a well-studied reaction on catalysts [1]. It

was noticed that in presence of moisture, the oxidation reaction is more easily activated [2]. Later, surfaces of noble metals such as Pd, Pt, Ag, and Ir were used successfully to convert CO [3, 4, 5, 6].

Yet, the increasing cost of commercial catalysts made from noble metals and the considerable amount of produced CO urges altering bulk noble metals with a more affordable form of catalysts.

Supported catalysts: It has been observed that deposition of noble metals in form of ultra-fine (nanoparticles) particles on a surface can change the chemical behavior of the metal dramatically and lead to raising novel properties. An original example is gold which is not an active catalyst as bulk [7], but a change in chemical behavior was observed when the size of the gold particles decreased to 10 nm [8]. The catalytic behavior of Nanoparticles (NPs) is a function of many parameters: particle size [9, 10], type of the supporting surface [11, 12], environment temperature [13], and shape and chemical composition [14]. Numerous research studies have been conducted to investigate and engineer the catalytic properties of these supported catalysts, both theoretically and experimentally [15, 16, 17, 18, 19, 20, 21]. Oxidation of CO has been vastly studied in the field of supported catalysts: deposited NPs of noble metals such as gold [22], palladium [23], platinum [24], Iridium [25], copper [26], and silver [27] have shown catalytic activities towards this reaction. Regarding the CO oxidation reaction, we consider two main mechanisms: Mars-Van Krevelen (MvK) if lattice oxygen is participating in CO oxidation and Langmuir-Hinshelwood (LH) if all the reactants (CO and oxygen) are chemisorbed on the catalyst from the ambient before activation (see Figure 1).

Nanoparticles:

Au supported catalysts are highly investigated for CO oxidation application [28, 21]. The interface between Au particles

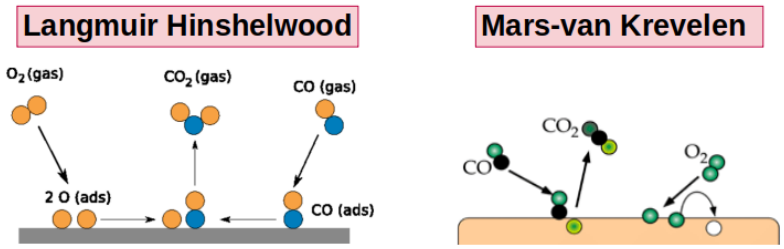

Figure 1: Two fundamental CO oxidation mechanisms: 1) MvK: CO reacts with lattice oxygen, 2) LH: Both gas-phase reactants are adsorbed on the catalyst and then react.

and oxide was found to be crucial for catalytic activity [29]. The environmental effect on the activity of Au particles was studied; dual catalytic sites were observed on Au NPs, depending on the temperature: it was possible to activate O_2 on Au nanoparticles at T $\geq$ 80°C. At lower temperatures, however, O_2 was activated at the interface of nanoparticle–oxide [30]. Tuning the size of the nanocatalyst is of high importance. While bilayer gold films exhibited higher activity relative to Au NPs ($\sim$ 3 nm) [31], smaller Au NPs (average size $\sim$ 2 nm) were reported to have the highest activity [32].

Size effect can vary when the type of the metal changes; while smaller Au particles were more active, Ru particles exhibited higher oxidation activity when the particle size increased from 2 to 6 nm [33]. Moreover, the composition of Ru particles was affected by particle size; spectroscopic characterization revealed that smaller Ru particles contained more amount of RuO_2 [34].

Pd_{38} particle and Pd slab were modeled by DFT to study their performance for CO oxidation; the rate-determining step of reaction was found to be O_2 dissociation on Pd particle and CO_2 formation on Pd slab, with Pd cluster showing higher activity [35]. The activation energy of CO oxidation on a Pd(111) single crystal was measured twice as the one on $\sim$ 2 nm Pd nanoparticles. Moreover, comparing large Pd particles (27 nm) with the

2 nm particles, the small ones were reported to be more reactive [36]. The type of supporting surface was found to have an influence on the oxidation mechanism: on graphene-supported dispersed Pd particles, CO oxidation followed Langmuir- Hinshelwood mechanism [37]. On an oxide such as CeO_2, in addition to Langmuir- Hinshelwood, the Mars-Van Krevelen oxidation mechanism was also observed [38].

The profound impact of particle surface interface on catalytic performance was observed also on TiO_2 supported Cu NPs, on which the interface acted as an active site for the reaction to happen. Highly dispersed Cu particles were synthesized by the deposition-precipitation method, yielding a remarkable number of interfacial sites which made the catalysts active for temperatures from 120 to 240 °C [39]. Cu particles supported on aerogel TiO_2 assisted extraction of lattice oxygen and CO oxidation proceeded Mars-Van Krevelen mechanism [40].

Platinum particles have been vastly investigated; numerous experimental and theoretical studies have been conducted to better understand the properties and performance of these particles for different applications such as in fuel cells [41, 42], conversion of exhaust gases [43, 44], and oxidation of hydrocarbons [45]. Oxidation of CO is one of the most common chemical reactions which has been studied on these catalysts.

In an experiment, Pt NPs ($1 \sim 3$ nm) were synthesized via a chemical colloid deposition method on Fe_2O_3 under oxygen-rich condition, with 2 nm particles showing the highest activity [16]. In another experimental study, a large range of Pt particles ($2 \leq$size≤ 16 nm) was synthesized at different temperatures (300-700 °C); those prepared at higher temperature had smaller diameter and a higher ratio of $Pt_{metallic}/Pt_{total}$. Pt atoms in contact with the support could be in a partially oxidized state ($Pt^{+\delta}$) due to charge transfer from the metallic cluster to the surface. However, Pt atoms with a metallic state were found to be active

sites for catalytic reaction since the turnover frequency (TOF) of the reaction increased at a higher ratio of $Pt_{metallic}/Pt_{total}$. TOF is a measure of the catalyst efficiency; which is stated as reaction progress normalized by active sites with respect to time. The role of supporting surface in catalytic activity was studied also for Pt catalysts. The reaction rate of CO oxidation was higher on Pt particles supported on reducible transition metal oxides such as Co_3O_4, Mn_3O_4, TiO_2 and NiO, compared to inert surfaces like SiO_2 [46]. A similar result was obtained by comparing reducible TiO_2 and irreducible Al_2O_3 [47]. Also, interfacial sites of ceria and Pt particles were found to be active sites for oxidation reaction [48]. Deposition of Pt NPs on Fe_3O_4 surface enhanced reducibility of the surface and creation of lattice oxygen vacancy, so the Mars-Van Krevelen mechanism was also involved in the oxidation reaction [49].

Single atoms: The smallest size of metallic catalysts, highly dispersed single-atom catalysts (SACs), have the most efficient utilization geometry [50, 51]. In a theoretical simulation, oxidation of CO over Ir_1 supported on FeO_x was compared to Pt_1 on the same surface, and Pt_1 showed higher activity regarding CO conversion [52]. In experimental investigations, Pt_1/FeO_x system was reported to be highly stable and an efficient catalyst [53, 54]. CO oxidation was observed over Pt single atoms supported on zeolite at 150 °C with moderate activity [55]. On TiO_2 nanowires, Pt SACs were found to be remarkably active for CO oxidation and 90 % of CO conversion happened at temperature $\sim$ 160 °C [56].

One of the difficulties in synthesizing single-atom catalysts is the homogeneity and stability of single atoms. In the case of Pt_1/CeO_2, lowering the temperature in a reducing environment led to agglomeration of Pt atoms into Pt particles [57]. One of the successful approaches to synthesizing the Pt SACs was a wet impregnation technique (strong electrostatic adsorption)

[50]. Low Pt loading and a large volume of the solution including TiO_2 particles as well as controlling the pH resulted in the homogeneous deposition of 1 Pt per TiO_2 particle which in turn were stable through reductive and oxidative conditions.

Nanoclusters: Nanoclusters bridge the size gap between the nanoparticles and single-atom catalysts. Reported properties of nanoclusters can be controversial, since adding or removing one atom can change the chemical properties and catalytic behavior of the system [58]. Hence, extrapolation of the nanoparticle properties to clusters is not possible and one needs to study each system individually.

A theoretical study on Pt_{11} and Au_{11} cluster supported on TiO_2 predicted two different reaction paths for oxidation of CO; while activation of CO was found to be directly possible on O_2 adsorbed on Au_{11}, dissociation of O_2 was found to be an additional step on Pt_{11} prior to the formation of CO_2 [59]. In the same work, the dissociation of oxygen molecules on the pure Au cluster was predicted to require activation energy almost three times higher than (activation energy = 1.53 eV) compared to the Pt cluster (activation energy = 0.52 eV). On the other hand, the oxidation of CO was more activated on the Pt cluster than on the Au cluster by 0.75 eV. Yet, considering the whole oxidation path, CO oxidation was predicted to be less demanding on Pt_{11}; also Pt cluster was bonded to the surface more strongly.

Subnano scale Pt_x clusters (x from 4 to 35) were deposited on TiO_2 by magnetron sputtering and quadrupole mass filter; the contribution of a different mechanism in the oxidation of CO was discussed by isotopically labeling the reactants. It was suggested that Pt atoms at the edge of the clusters are active sites for the reaction; yet an atomic-level model was not provided to support this claim [60].

Size selected Pt clusters (Pt_5 and Pt_{19}) were adsorbed on Fe_3O_4 to study the mechanism of CO oxidation reaction. Mars-

Van Krevelen and migration of lattice oxygen were discussed, but DFT modeling was limited to the first step of the reaction (extracting the oxygen from the lattice) and kinetics of the reaction on the system remained to be further cleared[61].

Schneider et. al. [62] studied the oxidation of CO on small Pt clusters. They investigated the energetics of interaction between Pt clusters and molecular oxygen. Latter work did not cover the kinetics of the reaction, and Pt clusters were studied only in the gas-phase and not on the surface.

A small Pt cluster (Pt_4) was modeled on TiO_2 [63], and a study regarding the kinetics of CO oxidation via the Mars-Van Krevelen mechanism was provided. But no more insight was provided regarding other oxidation mechanisms.

There are many studies focusing on the Pt NPs [24, 64, 65, 66]; but Pt clusters are not as well-studied as Pt NPs. In particular, a systematic study on the performance of subnano scale Pt catalysts (few atoms) on the atomic scale is missing.

Oxidation of nanocluster: One important possibility which should be considered for nanoparticles and clusters is their oxidation in catalytic conditions [67, 68]. It has been reported that the oxidation state of Pt NPs has an impact on the catalytic properties of the particles [69, 70]. Hence, it is important to understand the factors that affect the oxidation degree of Pt NPs. Studies show that the size of NPs, their interaction with the supporting surface, the nature of the supporting surface, and the temperature and pressure of the gas-phase atmosphere can change the propensity of Pt NPs for oxygen [71, 72, 73, 57, 74, 75, 76]. CO oxidation was investigated on Pd NPs and at higher temperature ($\geq$ 500 K) dynamic formation and decomposition of oxides was observed, leading to suppression of CO oxidation [77].

An ab initio investigation on Pt_7 reported the most stable structures of Pt_7O_x with x varying from 1 to 7 [78]; however, this

study does not provide a trend for the oxidation of Pt clusters. The correlation between the cluster size and oxidation of clusters remains unclear.

About this work: The aim of the present work is first to computationally investigate the oxidation of Pt_x clusters ($x \leq 8$) in gas-phase and supported on two metal oxides: brookite TiO_2 and Co_3O_4. Anatase and rutile TiO_2 are more studied surfaces for the Pt supported catalysts rather than brookite [79, 65, 80, 76]. Also, we are studying Pt clusters supported on Co_3O_4 for the first time, and comparing the properties of Pt clusters on these two different surfaces would be interesting and informative. Then, the catalytic performance of supported clusters will be discussed through different oxidation mechanisms. In addition to Pt clusters, we also conducted a comprehensive study on the performance of single-atom supported Pt regarding the oxidation of CO. Moreover, we elucidate the possibility of CO oxidation over a supporting surface that is doped with atomic Pt.

This thesis consists of seven chapters: The first and last ones are the introduction and conclusion, the second chapter explains the applied computational approaches, and the rest discuss the results. The thesis is organized as follows:

Chapter 2 (Computational methods) In this chapter, we explain methods, theories, and approximations that have been used for simulations in this thesis.

Chapter 3 (Global minima of Pt clusters) This chapter represents the structures of global minima of gas-phase and supported Pt catalysts, with different sizes and oxidation degrees.

Chapter 4 (Oxidation of Pt clusters) In this chapter, the tendency of Pt nanoclusters for oxidation is discussed and compared to bulk Pt. Also, the correlation between cluster size and oxidation degree is explained. Last, the role of support and in-

teraction between the metallic clusters and surface is discussed.

Chapter 5 (CO oxidation via MvK mechanism) CO oxidation reaction was modeled to probe the catalytic performance of Pt clusters as well as single Pt catalysts. Here, we consider the oxidation reaction to proceed through the Mars-Van Krevelen mechanism, which involves oxygen atoms from the surface lattice.

Chapter 6 (CO oxidation via LH mechanism) In this chapter we explain the reaction of CO oxidation via the Langmuir-Hinshelwood mechanism. This chapter ends with a discussion of the findings of this work and makes a comparison to the findings of other researchers.

2 Computational Methods

This chapter presents the theory and methodology which have been applied for simulations in this thesis. Density functional theory (DFT), as a widely used approach for the simulation of materials, is the main tool employed in this work to compute the energy and features of the systems. Concepts, approximations, and computational details are discussed thoroughly in the present chapter.

2.1 Density Functional Theory

Density functional theory [81, 82] is a method based on quantum mechanics (QM) which is useful in chemistry and physics to compute the electronic structure of different systems such as atoms, molecules, and bulk solids. DFT is accurate in principle, however for application purposes and to make it computationally possible, it is necessary to make approximations. Developing these approximations is the goal of many research studies. Yet, DFT is applicable to calculate many physical and chemical properties. Since DFT provides a proper balance between computational accuracy and cost, it has been widely used as a standard electronic structure method.

In this chapter, we summarize the basic theorems, concepts, and approximations in DFT and the computational methods used in the present work.

2.1.1 The Born-Oppenheimer approximation

For a system composed of atoms or molecules, there are several nuclei and electrons that should be treated as quantum particles. One of the problems with the many-body system is that the Hamiltonian is not solvable because the degrees of freedom of N_e electrons and N_n nuclei are coupled. However, since nuclei

are almost 1000 times heavier than electrons, their motion is too slow to affect the electronic configuration. Thus, it is possible to treat the atomic nuclei and electrons separately. So, here nuclei are considered as points in space with specific mass and charge from which the motion of electrons is independent. This approximation, also known as Born-Oppenheimer (BO) approximation or adiabatic approximation [81], proposes to express the total wavefunction as a product of the ionic $\Psi(\mathbf{R})$ and the electronic $\psi(\mathbf{r})$ wavefunction:

$$\Phi(\mathbf{r}, \mathbf{R}) = \Psi(\mathbf{R})\psi_{\mathbf{R}}(\mathbf{r}) \tag{2.1.1}$$

The wavefunction of nuclei is found by solving the Schrödinger equation:

$$(-\sum_{I} \frac{\hbar}{2M_I} \frac{\partial^2}{\partial \mathbf{R}_I^2} + E(\mathbf{R}))\Psi(\mathbf{R}) = \epsilon\Psi(\mathbf{R}) \tag{2.1.2}$$

where $\mathrm{E}(\mathbf{R})$ is the ground-state energy of electronic Schrödinger equation and $\mathrm{M_I}$ presents the mass of the i-th nucleus. The electronic Schrödinger equation can be expressed as:

$$\begin{aligned}(-\textstyle\sum_i \frac{\hbar}{2m_i}\frac{\partial^2}{\partial \mathbf{r}_i^2} + \frac{e^2}{2}\sum_{i\neq j}\frac{1}{|\mathbf{r}_i-\mathbf{r}_j|} - \sum_{i,j}\frac{Z_I e^2}{|\mathbf{r}_i-\mathbf{R}_j|} \\ + \frac{e^2}{2}\sum_{I\neq J}\frac{Z_I Z_J}{|\mathbf{R}_I-\mathbf{R}_J|})\psi_{\mathbf{R}}(\mathbf{r}) = E(\mathbf{R})\psi_{\mathbf{R}}(\mathbf{r})\end{aligned} \tag{2.1.3}$$

Here e and m stand for the charge and mass of the electron. Adiabatic methods are easier to be implemented than non-adiabatic ones and yield reasonable and cost-effective results. Yet, by applying the BO approximation one can not solve the many-body problem analytically. After factorizing the ionic and electronic wavefunction, we still remain with the electronic problem which is a challenge to solve due to the interaction among electrons.

2.1.2 Hohenberg-Kohn Theorems

The Hohenberg and Kohn theorems are valid for a many-particle system and map the interacting electron system into non-interacting electrons in an external potential originating from the atomic nuclei. According to the first Hohenberg-Kohn theorem, for any interacting system of particles, there is a one-to-one correspondence between the ground state electron density $n_0(\mathbf{r})$ and the external potential $v_{\text{ext}}(\mathbf{r})$, and the Hamiltonian is uniquely determined by the electron density. So, for any external potential $v_{\text{ext}}(\mathbf{r})$, it is possible to define the energy of the system as a unique functional of the density $n(\mathbf{r})$: $E = E[\text{n}(\mathbf{r})]$. The energy functional in terms of the external potential $v_{\text{ext}}(\mathbf{r})$ can be expressed as:

$$E[n(\mathbf{r})] = \int v_{\text{ext}}(\mathbf{r}) n(\mathbf{r}) dr + F[n(\mathbf{r})] \tag{2.1.4}$$

where F$[n(\mathbf{r})]$ is an unknown/ the universal functional of the charge density. This functional is independent of the external potential and contains only the kinetic energy and the interaction among electrons: $F[n(\mathbf{r})] = T[n(\mathbf{r})] + V_{e-e}[n(\mathbf{r})]$. The second Hohenberg-Kohn theorem determines an important property of the energy functional: The true electron density is the one that minimizes the energy of the overall functional. In practice, based on the variational principle, the ground-state electron density is found by changing the electron density until it minimizes the energy functional. In principle, all ground state properties are determined from the minimization of the functional E[n($\mathbf{r}$)].

2.1.3 Kohn-Sham Equations

The main idea of Kohn and Sham (KS) is to replace the many-body system of interacting electrons with a non-interacting auxiliary system. They approximated the ground-state density of interacting electrons with that of a non-interacting auxiliary system. Thus, equation 2.1.4 can be written as bellow:

$$E[n(\mathbf{r})] = T_s[n(\mathbf{r})] + \int v_{\text{ext}}(\mathbf{r})n(\mathbf{r})dr + E_{Hartree}[n(\mathbf{r})] \\ + E_{N-N} + E_{xc}[n(\mathbf{r})] \tag{2.1.5}$$

Considering the spin (σ) of N^σ independent electrons, the ground-state energy of the system can be obtained by summing over all Kohn- Sham orbitals ($\psi_i^\sigma(\mathbf{r})$):

$$n(\mathbf{r}) = \sum_{\sigma=\uparrow,\downarrow} n^\sigma(\mathbf{r}) = \sum_{\sigma=\uparrow,\downarrow} \sum_{\mathbf{i=1}}^{\mathbf{N}^\sigma} |\psi_{\mathbf{i}}^\sigma(\mathbf{r})|^{\mathbf{2}} \tag{2.1.6}$$

$T_s[n(\mathbf{r})]$ is the kinetic energy of the auxiliary system:

$$T_s[n(\mathbf{r})] = \tfrac{1}{2} \sum_{\sigma=\uparrow,\downarrow} \sum_{i=1}^{N^\sigma} \psi_i^{*\sigma}(\mathbf{r})(\tfrac{-\hbar}{2m}\overrightarrow{\nabla})\psi_i^\sigma(\ \mathbf{r}) \tag{2.1.7}$$

and $\mathrm{E}_{Hartree}$ [n($\mathbf{r}$)] is the Coulomb energy of charge density interacting with itself:

$$E_{Hartree}[n(\mathbf{r})] = \tfrac{e^2}{2} \int \tfrac{n(\mathbf{r})n(\mathbf{r\prime})}{|\mathbf{r}-\mathbf{r\prime}|} d\mathbf{r}d\mathbf{r\prime} \tag{2.1.8}$$

The unknown exchange-correlation caused by many-body effects is presented as exchange-correlation energy E_{xc}(n($\mathbf{r}$)):

$$E_{xc}[n(\mathbf{r})] = T[n(\mathbf{r})] - T_s[n(\mathbf{r})] + V_{ee}[n(\mathbf{r})] - E_{Hartree}[n(\mathbf{r})] \tag{2.1.9}$$

The first two terms refer to the difference in kinetic energy of the interacting and non- interacting systems. Minimizing

equation 2.1.5 leads to Schrödinger-like equations corresponding to Kohn- Sham orbitals:

$$H_{KS}^{\sigma}\psi_i^{\sigma}(\mathbf{r}) = \epsilon_i^{\sigma}\psi_i^{\sigma}(\mathbf{r}) \tag{2.1.10}$$

where H_{KS}^{σ} is defined as:

$$H_{KS}^{\sigma} = -\frac{\hbar}{2m}\nabla^2 + v_{eff}^{\sigma}(\mathbf{r}) \tag{2.1.11}$$

and effective potential is defined as:

$$v_{eff}^{\sigma}(\mathbf{r}) = v_{ext}(\mathbf{r}) + e^2 \int \frac{n(\mathbf{r\prime})}{|\mathbf{r}-\mathbf{r\prime}|} d\mathbf{r\prime} + \mathbf{v}_{\mathbf{xc}}^{\sigma}[\mathbf{n}(\mathbf{r})] \tag{2.1.12}$$

The unknown term $v_{xc}^{\sigma}[n(\mathbf{r})]$ includes all non- classical electronic interactions:

$$v_{xc}^{\sigma}[n(\mathbf{r})] = \frac{\delta E_{xc}[n(\mathbf{r})]}{\delta n(\mathbf{r})} \tag{2.1.13}$$

So far we have not approximated any term, hence if we knew the exact functional $E_{xc}[n]$, the Kohn-Sham equations would lead to the exact ground-state density and energy of the interacting system.

2.1.4 Exchange-correlation functionals

The Kohn-Sham equations map the interacting many-body system onto a set of independent single-particle equations successfully and make the problem much easier. Although, without knowing the exact form of the exchange-correlation energy functional E_{xc}[n], the KS equations are not solvable. A class of approximations to the exchange-correlation is the Local Density Approximation (LDA), which assumes that each small volume of the system behaves as a homogeneous electron gas with a density equal to the local density of the inhomogeneous system [82]:

$$E_{xc}^{LDA}[n(\mathbf{r})] = \int \epsilon_{xc}^{hom}(n(\mathbf{r}))n(\mathbf{r})d\mathbf{r}, \tag{2.1.14}$$

where $\epsilon_{xc}^{hom}(n(\mathbf{r}))$ stands for the exchange-correlation energy of each electron in the homogeneous electron gas with a density of n($\mathbf{r}$). Also, exchange-correlation potential is a functional derivative of exchange-correlation energy:

$$V_{xc}^{LDA}[(\mathbf{r})] = \frac{\delta E_{xc}^{LDA}[n(\mathbf{r})]}{\delta n(\mathbf{r})} = \epsilon_{xc}^{hom}(n(\mathbf{r})) + n(\mathbf{r})\frac{\partial \epsilon_{xc}^{hom}(n(\mathbf{r}))}{\partial n(\mathbf{r})}, \tag{2.1.15}$$

In spite of LDA efficiency for systems with slow changes in spatial density, there is the problem of bond-length underestimation and binding energy overestimation with LDA. Here, Generalized gradient approximation (GGA) corrections help with these limitations in terms of density gradient [83].

$$E_{xc}^{GGA}[n(\mathbf{r})] = \int \epsilon_{xc}^{GGA}((n(\mathbf{r})), \nabla n(\mathbf{r}))n(\mathbf{r})d\mathbf{r}, \tag{2.1.16}$$

GGA provides better values for binding energy and bond length compared to LDA and delivers a better description of the inhomogeneous system which is a failure of LDA. Many forms of GGA functional have been proposed [84, 85, 86, 87], and among them Perdew formulation [84] is the most used form.

2.1.5 Numerical implementation of the Kohn-Sham equations

To use DFT for practical purposes, the Kohn-Sham equations must be transformed into an algebraic form to be solved numerically by computers. In periodic crystalline solid systems, the electronic wavefunction and all the operators in the Hamiltonian can be expanded in a plane wave basis set. According to the Bloch theorem, the Kohn-Sham electronic wavefunctions in a periodic potential, V ($\mathbf{r}$ + $\mathbf{R}$) = V ($\mathbf{r}$), can be written in

the momentum space as a plane wave modulated by a periodic function $u_{nk(\mathbf{r})}$, with the same periodicity $u_{nk(\mathbf{r}+\mathbf{R})} = u_{nk(\mathbf{r})}$:

$$\psi_{n,\mathbf{k}(\mathbf{r})} = e^{i\mathbf{k}.\mathbf{r}} u_{n,\mathbf{k}(\mathbf{r})}, \tag{2.1.17}$$

here $\mathbf{k}$ is the electron crystal momentum and it is defined in the first Brillouin zone of the reciprocal lattice, and n is the band index. The periodic part is expandable in a basis set of plane waves:

$$u_{n,\mathbf{k}}(\mathbf{r}) = \frac{1}{\sqrt{\Omega}} \sum_{\mathbf{G}} c_{n,\mathbf{k}+\mathbf{G}} e^{i\mathbf{G}.\mathbf{r}} \tag{2.1.18}$$

Here Ω represents the cell volume, G is a vector in reciprocal space and $c_{n,\mathbf{k}+\mathbf{G}}$ is the coefficient of the plane waves. So the Kohn Sham orbitals are described as:

$$\psi_{n,\mathbf{k}}(\mathbf{r}) = \frac{1}{\sqrt{\Omega}} \sum_{\mathbf{G}} c_{n,\mathbf{k}+\mathbf{G}} e^{i(\mathbf{k}+\mathbf{G}).\mathbf{r}} \tag{2.1.19}$$

This is an exact expansion if we have an infinite plane wave basis set. In practice, the number of plane waves should be finite due to computational limitations. Thus, the latter summation is truncated by cutoff energy (E_{cut}) which is the kinetic energy:

$$\frac{\hbar^2}{2m} |\mathbf{k} + \mathbf{G}|^2 \leq E_{cut} \tag{2.1.20}$$

Only $\mathbf{G}$ vectors with kinetic energy lower than E_{cut} are included. The sufficient size for the plane wave basis set is determined by convergence tests of total energy, adsorption energy, etc., as a function of E_{cut}. This way the required accuracy for each type of calculation is obtained.

In a similar fashion, the ground-state density is also expandable in plane waves:

$$n_0(\mathbf{r}) = \sum_{G} n_0(\mathbf{G}) e^{i\mathbf{G}.\mathbf{r}} \tag{2.1.21}$$

where $n_0(\mathbf{G})$ is the charge density in the reciprocal space:

$$n_0(\mathbf{G}) = \frac{1}{\Omega}\sum_n \int_{BZ} f_{n,\mathbf{k}} \sum_{\mathbf{G\prime}} c^*_{n,\mathbf{k}+(\mathbf{G\prime}-\mathbf{G})} c_{n,\mathbf{k}+\mathbf{G\prime}} d\mathbf{k} \qquad (2.1.22)$$

The modulus of the largest $\mathbf{G}$ vector in equation 2.1.21 can be twice the maximum $\mathbf{G}$ vector defined by E_{cut}. Thus the kinetic energy cut off of n_0 ($\mathbf{r}$) can be 4 times larger than the one of the wavefunction. Another numerical approximation is to replace the integral over BZ with a summation over a discrete grid of $\mathbf{k}$-points. This grid is used to sample the BZ, and one of the most popular schemes is Monkhorst- Pack grid [88]. It is possible to solve the KS equations consistently since the effective potential in the KS equations and the n($\mathbf{r}$) are related. Figure 2 shows the self-consistent iterative method to numerically find the solution of the KS equations.

Since the effective potential and n($\mathbf{r}$) are both unknown, the algorithm starts with an initial guess of n($\mathbf{r}$), which usually is the superposition of atomic n($\mathbf{r}$), and then effective KS potential is calculated and the KS equation is solved with single-particle eigenvalues and wavefunctions, a new electron density is then calculated from the wave functions. The convergency is achieved when changes in the total energy of the atomic system are less than the pre-defined criteria. Otherwise, the calculated (new) n($\mathbf{r}$) is mixed with the initial guessed n($\mathbf{r}$) (old) and the outcome n($\mathbf{r}$) will be used for the next iteration.

2.1.6 Pseudopotentials

Another problem is the strong localization of the wave function of core electrons. A large number of plane waves are required to describe these electrons. Moreover, core electrons do not contribute to chemical reactions. These lead to the idea of using pseudopotentials [90]. Pseudopotentials are used to freeze the core electrons and replace the potential of the nuclei plus core

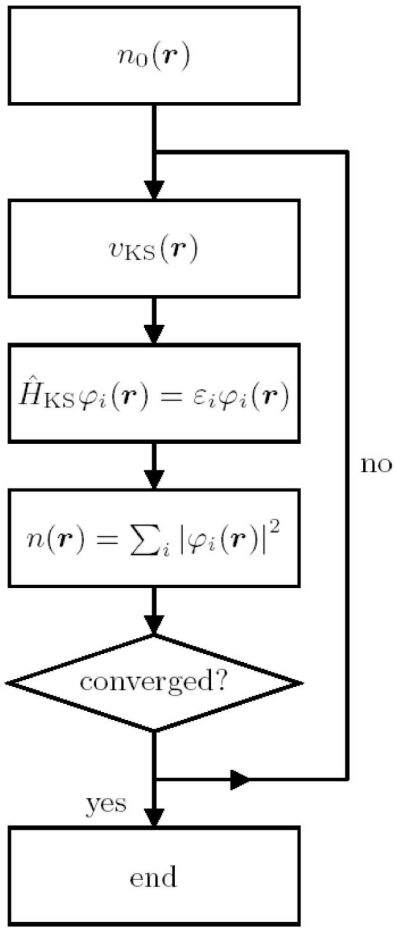

Figure 2: Schematic diagram of the self- consistent algorithm for solving the KS equation[89].

electrons with a fictitious potential, in a way that the behavior of the valence electrons is not affected beyond the cutoff radius r_c away from the nucleus. The resultant pseudo-wave function must be equal to all wavefunctions after r_c and smooth before r_c; this way a smaller number of plane waves are required.

2.1.7 DFT + U

For many systems such as transition metal oxides, DFT fails to give a correct prediction for the ground-state [91, 92, 93]. Semi-

local exchange-correlation approximations exhibit both one-electron and many-electron self-interaction error [94, 95, 96]. The cause of this error originates in localized, highly correlated electrons of d and f-orbitals in transition metals and the fact that potentials in LDA and Generalized Gradient Approximation (GGA) approximations are orbital-independent. Thus, to properly describe the properties of strongly correlated systems, one should use orbital-dependent potentials for d- orbitals electrons. One way to incorporate the electron-electron correlation is to directly add a term to Hamiltonian [97, 98]. DFT calculations corrected in this way are called LDA+U or GGA+U. DFT+U separates the electrons into two groups: s and p- orbital electrons which are described by orbital-independent potential and localized d-orbital electrons whose Coulomb interaction should be described by orbital-dependent potential. DFT+U Hamiltonian is written as [91]:

$$E^{DFT+U} = E^{DFT} + \sum_I [\frac{U}{2} \sum_{m,\sigma \neq m\prime,\sigma\prime} n_m^{I\sigma} n_m^{I\sigma\prime} - \frac{U}{2} n^I (n^I - 1)] \tag{2.1.23}$$

here n denotes the atomic orbital occupation, I represents the ion, m, and σ are the orbital and spin. U term (also Hubbard term) favors integer occupation numbers and creates Highest Occupied Molecular Orbital (HOMO)/Lowest Unoccupied Molecular Orbital (LUMO) gap in insulator materials which are incorrectly described by DFT. Determining the proper U term for each system is challenging, though it is possible to find through a self-consistent approach. Following our previous works [99] and other work [100], the values we have used in this work are 3.0 and 3.5 eV for Co and Ti, respectively.

2.2 Genetic algorithm

New properties and size-dependent behaviors of nanoscale particles have drawn remarkable attention to studying these systems. The first step of any computational investigation is to find an atomic configuration that is energetically close to the ground state or global minima (GM) structure. This task is manually possible for a few numbers of atoms; however finding the GM of a larger number of atoms is spatially complicated and very difficult, since the number of the possible generated structures increases exponentially with respect to the number of atoms ($\mathcal{O}(N^3)$). Moreover, it is required to find the GM within a reasonable amount of time and computational resources. The total energy of different configurations of a set of atoms as a function of their positions creates their potential energy surface (PES). Finding the GM means finding a point in PES that corresponds to the lowest energy. The main challenge is to find the lowest point on this surface among other local minima. Many algorithms have been developed to build the PES and find the GM. One can categorize these algorithms into thermodynamics and evolutionary-based ones. Algorithms driven by thermodynamics are molecular dynamics [101] and Monte Carlo algorithms such as the popular Basin Hopping method [102]. The algorithm applied in this work is one of the evolutionary genetic algorithms, which is based on the evolution of the structures through the mutual pairing of a population of candidates. One of the most important developments in these algorithms was the introduction of the cut-and-splice pairing operator [103]. To find the structural GM of Pt and PtO_x clusters we used the genetic algorithm (GA) as implemented in Atomic Simulation Environment (ASE) package [104, 105]. This algorithm is applicable in structural optimization of both gas-phase and supported clusters [106, 107, 108].

Before starting the algorithm, a set of random initial candidates are generated in a defined simulation cell. Typical size of $10 \sim 20$ (depending on the size of the cluster) candidates was chosen to keep the diversity of structures. Required minimum and maximum distances between atoms are specified in order to avoid detachment or overlapping of the atoms. As the algorithm starts running, a population (size varied from 10 to 20 structures) of the most stable and different structures is maintained to be used for further cutting and pairing. To satisfy these conditions, energy and interatomic distances are constantly compared. The selection of a pair of structures is as follows: Every structure is assigned with a fitness (F_i) and a probability (ρ_i) to be chosen according to the fitness shown in equation 2.2.2.

$$F_i = \frac{1}{2}[1 - tanh(2\rho_i - 1)], \tag{2.2.1}$$

$$\rho_i = \frac{E_i - E_{min}}{E_{max} - E_{min}} \tag{2.2.2}$$

Moreover, a uniqueness factor is considered for each candidate which tends to zero the more the structure is selected for pairing. The most important step in the algorithm is pairing two structures, in a way that the best part of them is preserved. Also, it should be ensured that the PES is sufficiently explored. Pairing step is done via the cut-and-splice operator, which cut the clusters into their halves through their center of mass and keeping the stoichiometry of the clusters by removing or adding atoms (Figure 3).

Finally, the interatomic distances are evaluated again to make sure that atoms are not too far or close, otherwise they are discarded and a new cutting operation is performed.
To avoid a degenerate population and keep the diversity of the structures, four types of mutations are applied to the new candidates after they are generated from pairing and before their

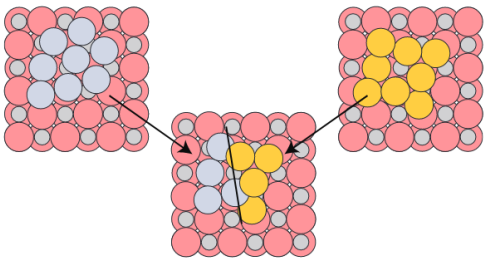

Figure 3: Cut-and-splice operator [104]

structure is locally optimized. By default 30% of new candidates are mutated; this is an optimal value and if the candidates are too mutated convergence of the GA would take longer. Implemented mutations in the algorithm are as follows:
Rattle: A random distance between 0 and 0.8 Å along a random direction is chosen to translate 40% of atoms in the cluster.
Twist: Applied on clusters supported on a surface; this mutation rotates the cluster with a random angle respected to surface normal.
Permutation: This mutation permutes the atomic number of one-third of the atoms and keeps the geometry of the cluster.
Mirror: Half of the cluster is selected and mirrored across a mirror plane which passes through the center of mass randomly. The stoichiometry of the cluster remains the same by adding or removing atoms.

The next step is to locally relax the candidates and update the population with new candidates. The criterion for convergence is arbitrary and based on the total number of structures computed, on the fact that the energy of the most stable structure does not change anymore for a sufficiently large number of steps, and on visual inspection of the geometry of the putative GM. The schematic performance of the GA is shown in Figure 4.

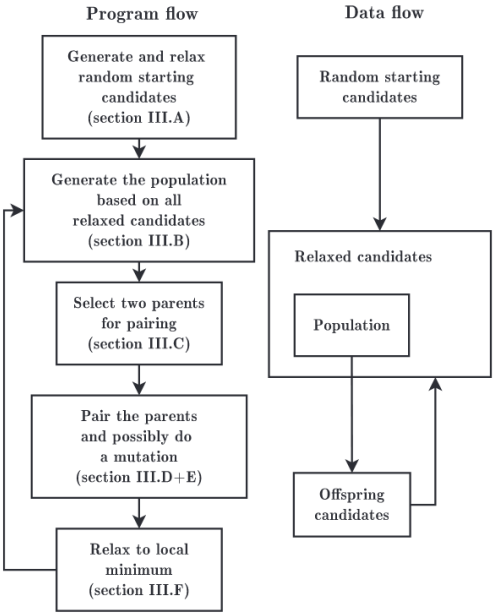

Figure 4: Overall steps of the algorithm and data flow [104].

2.3 Ab-initio thermodynamics

DFT calculations predict the electronic structure and material properties at zero temperature and pressure. Ab initio thermodynamics is a framework to connect the DFT results in microscale to macroscopic properties at finite temperature and pressure [109]. Gibbs free energy (G) is the appropriate type of potential to describe a system at finite temperature and pressure.

Change of the Gibbs free energy of a reaction can be calculated as:

$$\Delta G = G_{products} - G_{reactants} \tag{2.3.1}$$

A reaction with a negative (positive) value of ΔG is exothermic (endothermic), meaning that the conversion of reactants into products is thermodynamically favorable (unfavorable).

The Gibbs free energy of an atomic system can be decom-

posed as:

$$G = E_{tot} + F_{vib} + F_{rot} + F_{trans} + F_{elec} + pV \tag{2.3.2}$$

Here E_{tot} represents the internal (DFT total) energy of the optimized system which is the minimum of PES. We are interested in changes in the total energies and not the absolute values, since the absolute value of the total energy depends on the type of the pseudopotential and does not have a physical meaning. F_{vib}, F_{rot}, and F_{trans} are the vibrational, rotational and translational energies, and F_{elec} is the electronic energy of the system. The energy corresponding to the vibrational frequency of a system including the zero-point energy is defined as [110]:

$$F_{vib} \simeq k_B T \sum_i \frac{h\nu_i}{2k_B T} \tag{2.3.3}$$

in which i denotes all the vibrational modes. The rest of the components usually have a small contribution and hence are neglected for supported clusters. But, for gas-phase clusters, a large contribution comes from translational and rotational entropy, which cannot be ignored. Therefore, we computed these contributions. It was found that for gas-phase clusters the Gibbs free energy of formation is not affected by the entropic contributions significantly. That is because the entropic contribution in metallic and oxidized clusters are quantitatively very similar and enter in equation 2.3.6 and cancel out each other. As an example, in the case of Pt_4O_8 entropy contribution at 600 K was calculated to be of the order of 10 meV, which is negligible.

The chemical potential of the species is the quantity that connects the DFT results with Gibbs free energy. The chemical potential of an element is the change in the total energy of a system due change in the number of atoms of the given elements. In the present work, the reactants (O_2 and CO) are in

the gas-phase and are treated as ideal gases. Hence, the chemical potential of oxygen, μ_O, (and CO) depends on temperature and pressure according to:

$$\mu_O(T, p) = \mu_O(T, p^\circ) + \frac{1}{2} k_B T \ln\left(\frac{p}{p^\circ}\right), \tag{2.3.4}$$

where p° is the standard pressure, 1 bar, and k_B is the Boltzmann constant. The temperature dependence of μ_O at p° is obtained from the JANAF thermochemical tables [111]. We define the change in the chemical potential of oxygen relative to its zero-temperature value as:

$$\Delta\mu_O(T, p) = \mu_O(T, p) - \frac{1}{2} E(O_2) \tag{2.3.5}$$

To compute the Gibbs free energy of formation (oxidation energy) as a function of the oxygen chemical potential, we write:

$$\begin{aligned} \Delta G(T, p) &= G(Pt_xO_y) - G(Pt_x) - y\mu_O(T, p) \\ &\simeq E(Pt_xO_y) - E(Pt_x) - y\left(\tfrac{1}{2}E(O_2) + \Delta\mu_O(T, p)\right) \\ &= yE_{form}(Pt_xO_y) - y\Delta\mu_O(T, p) \end{aligned} \tag{2.3.6}$$

Where $E(Pt_x)$ and $E(Pt_xO_y)$ are total energies of metallic and oxide Pt clusters. Here we have approximated the free energy of metal and oxide clusters with their DFT total energy. While this approximation is reasonable for supported clusters, gas-phase clusters have large contributions from translational and rotational entropy, which cannot be ignored.

To check explicitly the effects of such contributions, we computed the rotational, vibrational, and translational entropic contributions according to statistical mechanics [110]. We found out that these entropic contributions have a negligible effect on the Gibbs free energy of the formation of gas-phase clusters.

The reason for this is that the value of entropic contribution in metallic and oxidized clusters are very similar; they enter in Eq. 2.3.6 with an opposite sign and so they cancel out. For example, for the Pt_4O_8 system, such entropic effects at 600 K are of the order of 10 meV, which is negligibly small. Vibrational frequencies were computed according to a finite difference scheme: atoms are shifted with 0.01 Å displacement along three dimensions and forces on atoms are computed. At zero temperature, the vibrational energy or zero point energy (ZPE) of the system is a non-zero value. The effect of ZPE in the total energy of the clusters is less than 0.05 eV/O for all the systems, hence it is not included in thermodynamics calculations.

2.4 Nudged elastic band method

Let us consider the PES corresponding to a reaction. Using local optimization, one can find the initial and final states of the reaction steps. Now the challenge is to find the minimum energy path (MEP) on PES and connect these two states. Figure 5 shows two local minima on the surface energy of a reaction.

The line connecting these two local minima passes through a transition state which is the saddle point of the presented surface energy. The method which was employed in the present work for finding the MEP and TS configuration of the reaction elementary steps is Nudged Elastic Band (NEB), developed by Henkelman et. al. and implemented in QE [113]. The idea is to create an initial linear interpolation between the reactant and product, discretized by a number of "images". These images are connected with an elastic spring so they do not collapse into the initial or final state. Depending on the complexity of the step, the number of images can vary from 5 to even 20. Figure 6 demonstrates a simple example of an initial guess of the code regarding the reaction path.

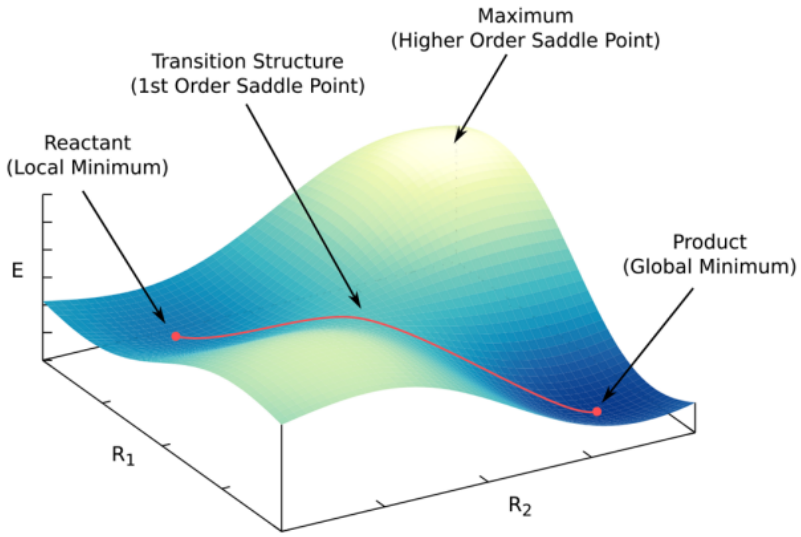

Figure 5: Schematic of PES of a fictional system [112]. Local minima of reactant and product is connected through a path which is shown by red line (MEP). The first order saddle point along the red line with the maximum energy is called the Transition state (TS).

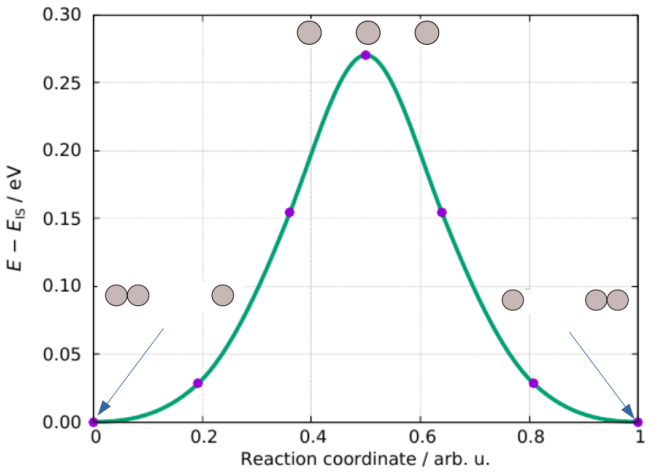

Figure 6: Linear interpolation of a simple chemical reaction,

NEB is a refinement of Elastic Band method [114], in which each atom feels a force defined as:

$$\mathbf{F_i} = -\nabla V(\mathbf{r_i}) + \mathbf{F_i^{spring}}, \tag{2.4.1}$$

$\mathbf{F_i^{spring}}$ is the spring constant:

$$\mathbf{F_i^{spring}} = k_{i+1}(\mathbf{r_{i+1}} - \mathbf{r_i}) = \mathbf{k_i}(\mathbf{r_i} - \mathbf{r_{i-1}}) \tag{2.4.2}$$

The climbing image NEB method (CI-NEB) [115] has one modification which drives the image with the highest energy up to the saddle point. First, a sufficient number of NEB algorithm iterations should be done so the reaction path becomes almost defined. Then, by turning on the climbing image option, the image with the highest energy starts climbing up along the elastic band to converge on the highest point of the saddle point.

The theory and the practical methodology employed in the present work were discussed in detail. A theoretical introduction regarding DFT and relevant approximations as well as computer implementation of the approach were presented. Further, ab initio thermodynamics was introduced as an approach to connect the numerical results of DFT calculation to the properties of the atomic system at finite temperature and pressure. Moreover, a systematic method for finding the global minima of atomic clusters was introduced and the setting and important parameters were discussed. Finally, the NEB method was considered in this work to study the kinetics of a reaction on nanoscale atomic clusters.

3 Global minima of Pt clusters

This chapter presents the stable structures of all the free-standing and supported Pt clusters with different numbers of Pt atoms. First, the computational details and bench markings are explained, and the structures and their stability are discussed.

3.1 Computational details and structural model

The DFT calculations were performed with the QUANTUM ESPRESSO (QM) code [116], employing a plane waves basis set and pseudopotentials. We adopted the Perdew–Burke-Ernzerhof (PBE) approximation for the exchange and correlation functional [84].

We employed ultrasoft pseudopotentials to describe Pt, Ti, and Co ions, while a projector-augmented wave pseudopotential was used for oxygen. For all the cluster simulations, k-point sampling of the Brillouin zone was performed at the gamma point and a Marzari-Vanderbilt scheme with a width of 0.136 eV was used to smear the electronic occupations. For nanoclusters, the relativistic effects could be pronounced in defining some properties. The impact of considering the spin-orbit coupling (SOC) was actually studied on Pt_7 cluster [78]. Although the magnetic moment, total energy, and energy scale of isomer clusters were remarkably different depending on considering or neglecting SOC, it was found that SOC has in fact no effect on the structure of the Pt_7 global minima and a negligible effect on the binding energy of Pt atoms in the cluster. Moreover, the phase diagrams obtained by ab initio thermodynamics were almost the same for SOC and non-SOC scenario. Finally, the effect of SOC was not found to be drastic on the catalytic activity of the cluster. Hence, we decided to neglect these effects in our simulations.

We simulated bulk platinum, PtO (Tetragonal, P42/mmc), and β-PtO_2 (Orthorhombic, Pnnm) as a reference, using the primitive unit cells, a $8 \times 8 \times 8$ k-point mesh, and a cutoff of 410 eV. The lattice parameter of optimized bulk Pt was found to be 3.96 Å, overestimated by 1% with respect to the experimental value of 3.92 Å[117]. As shown in table 1, the structural parameters of PtO and β-PtO_2 compare favorably with the experimental measurements [118, 119]. The cohesive energy of Pt bulk system was calculated to be -5.58 eV, in good agreement with the experimental value of -5.85 eV [120]. The calculated heats of formation for bulk PtO and β-PtO_2 with respect to the total energy of bulk Pt and molecular oxygen, are -0.48 eV/Pt and -1.44 eV/Pt, respectively. These values are consistent with previous theoretical works, -0.68 eV/-1.42 eV [72] and -0.55 eV/-1.57 eV [121].

Bulk	calculated lattice constants (Å)	exp. lattice constants (Å)
Pt	3.96	3.92
PtO	a = 3.149	a = 3.08
	c = 5.331	c = 5.34
β-PtO_2	a = 4.438	a = 4.48
	b = 4.533	b = 4.53
	c = 3.131	c = 3.13

Table 1: Structural computed parameters of bulk Pt, PtO and PtO_2.

The GA was employed in interface with QE in the present work to find the GM of small metallic and oxide Pt clusters, both in gas-phase and supported on surfaces of TiO_2 and Co_3O_4.

Supported clusters were modeled on the surface of Co_3O_4 (111) and brookite TiO_2 (210). Periodic slabs of TiO_2(210) and Co_3O_4(111) were modeled using (1×2, with 96 atoms) and (2×2, with 108 atoms) supercells, respectively (see figure 7). To model the TiO_2 (210) surface we considered a stoichiometric slab, consisting of 4 Ti-layers. To model the polar Co_3O_4(111) surface we employed a symmetric, non-stoichiometric slab, as

done in one of our previous works on this system [99]. Here we use a slab that includes a total of 11 layers, terminating with Co^{+2} (tetrahedral sites), Co^{+3} (octahedral sites) and O^{-2} atoms, the same model used by Yan et al. [122]. The surface is charged and has a dipole moment. Hence, one can consider Co_3O_4 (111) surface to be a Taskar type III polar surface [123].

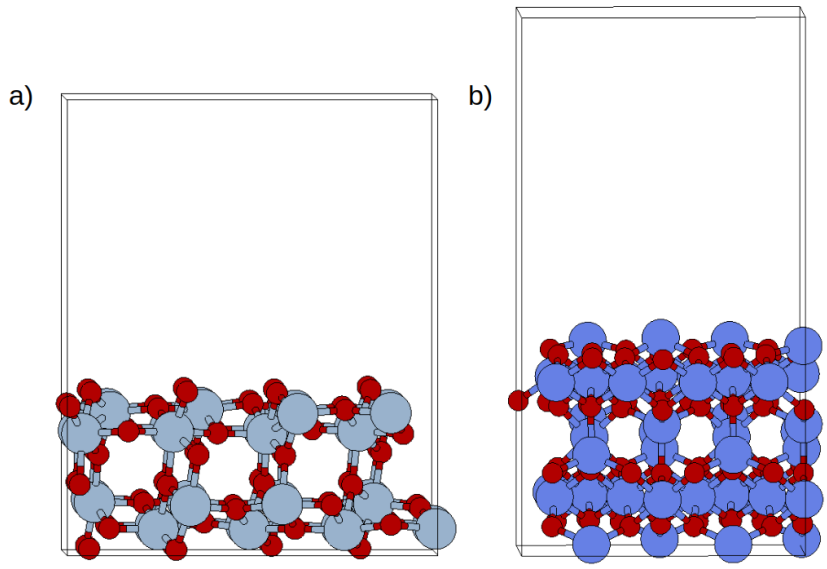

Figure 7: The slab models used in present work. a) Brookite TiO_2 (210) and b) Co_3O_4 (111) .

In all the calculations, the bottom two layers of the slabs were fixed, while the rest of the layers were allowed to relax. To avoid spurious interactions among periodic replicas of the slabs, we included 12 Å of vacuum in the direction normal to the surface. To model Co_3O_4 we used the DFT+U approach, adding a Hubbard term (3 eV) on the d states of Co atoms. In the case of stoichiometric TiO_2, we verified that the effect of adding a U=3.5 eV Hubbard term on the formation energy of Pt oxide clusters is negligible, therefore, we performed a PBE calculation. Whereas in the presence of oxygen vacancies (i.e. reduction of Ti^{4+} to Ti^{3+}) on the brookite surface, the addition of Hubbard term (U=3.5 eV) is necessary to calculate the formation energy

of oxygen vacancy.

Gas-phase Pt and Pt oxide clusters were simulated in a large $20 \times 20 \times 20$ Å^3 cubic cell. To model the oxidation of Pt clusters we considered five different stoichiometries, namely Pt_xO_y clusters with y/x = 0, 0.5, 1, 1.5, and 2, and considered clusters containing up to 8 Pt atoms. The search for the GM of gas-phase clusters is carried out in three steps: First, the GA algorithm was used in combination with the LAMMPS program to exploit the efficient reactive force field developed for the Pt-O system by Fantauzzi and co-workers [124]. The 20 most stable structures found from this step were then used as initial candidates for GA calculations at the DFT level. To perform the structural relaxation within the GA calculations we used loose criteria for the plane wave cutoff and forces: The Kohn-Sham orbitals are expanded up to a kinetic energy of 25 Ry for the wave function and 200 Ry for the charge density, and the maximum convergence force criterion for geometry optimization is 0.05 eV/Å per atom. The GM is then further optimized by a more stringent cutoff energy of 50/500 Ry and a force threshold of 0.026 eV/Å. The cohesive energy of gas-phase metallic clusters, normalized per Pt atom, is calculated as:

$$E_{coh} = (E(Pt_x) - xE(Pt_{iso}))/x \tag{3.1.1}$$

where $E(Pt_x)$ is the total energy of the gas-phase cluster, $E(Pt_{iso})$ is the total energy of an isolated Pt atom, and x is the number of Pt atoms in the cluster. Using the total energy of the Pt atom in the bulk form instead of isolated Pt, would result in positive cohesive energy.

Also in the case of supported clusters we adopted a two-step procedure. We first performed GA calculations with a cutoff of 25/200 Ry and a maximum force threshold of 0.05−0.2 eV/Å, depending on the size of the system. We then optimized the most stable structure with the same parameters of gas-phase

clusters (cutoff of 50/500 Ry and force threshold of 0.026 eV/Å).

When modeling the TiO_2/Pt_8 and the Co_3O_4/Pt_8, Co_3O_4/Pt_8O_8 systems, in order to avoid the interaction between periodic replicas of the clusters, the size of the cells were doubled, i.e. we employed (1×4) and (2×4) supercells, respectively. All calculations are spin polarized, with the exception of supported clusters on TiO_2, where we found negligible effects (less than 0.1 eV) of spin polarization on the formation energy of the supported clusters. We quantify the stability of the clusters by calculating the adsorption energy. The adsorption energy of metallic clusters on the TiO_2 and Co_3O_4 surface is calculated as [125]:

$$E_{ads} = (E(Pt_x@slab) - E(slab) - E(Pt_x)). \tag{3.1.2}$$

Here, $E(Pt_x@slab)$ is the total energy of the support + adsorbed Pt cluster, E(slab) is the total energy of the clean surface and $E(Pt_x)$ is the total energy of the metallic cluster in gas-phase where all systems have been relaxed.

More practical details about how to use the GA code is as below:

The starting population of 20 initial candidates was generated by GA according to criteria implemented in *StartGenerator* module of ASE. After DFT optimization of the initial candidates, new candidates were generated by pairing initial candidates using operations of mirror, rattle and permutation mutation (permutation only for oxidized clusters) with 0.3 probability. Interatomic distances and energy of structures were compared with the default values in *InteratomicDistanceComparator* module of ASE (pair_cor_cum_diff=0.015, pair _max=0.7, δE=0.02). To illustrate how a genetic algorithm (GA) optimization proceeds, in Figure 8 we show as an example the evolution of the total energy of the most stable structure encountered during

the (GA) calculation, relative to the putative global minimum (GM), as the GA is progressing, i.e. as a function of the number of structures computed. Figure 8.a refers to Pt_6O_6 in gas-phase, while Figure 8.c refers to Pt_6O_6 supported on Co_3O_4. Figure 8.b and 8.d illustrate the total energy of all the structures optimized during the GA calculation, ordered according to their total energy and referenced to the total energy of the putative GM. Figure 8.b refers to Pt_6O_6 in gas-phase, while Figure 8.d refers to Pt_6O_6 supported on Co_3O_4.

These examples show that, even in the case of small clusters with only 10 to 20 atoms, identifying a putative GM involves several hundred geometry optimizations. Since each of these optimizations is approximately $\mathcal{O}(N^3)$ in the number of atoms, global optimization of larger clusters becomes quickly prohibitively expensive as N increases.

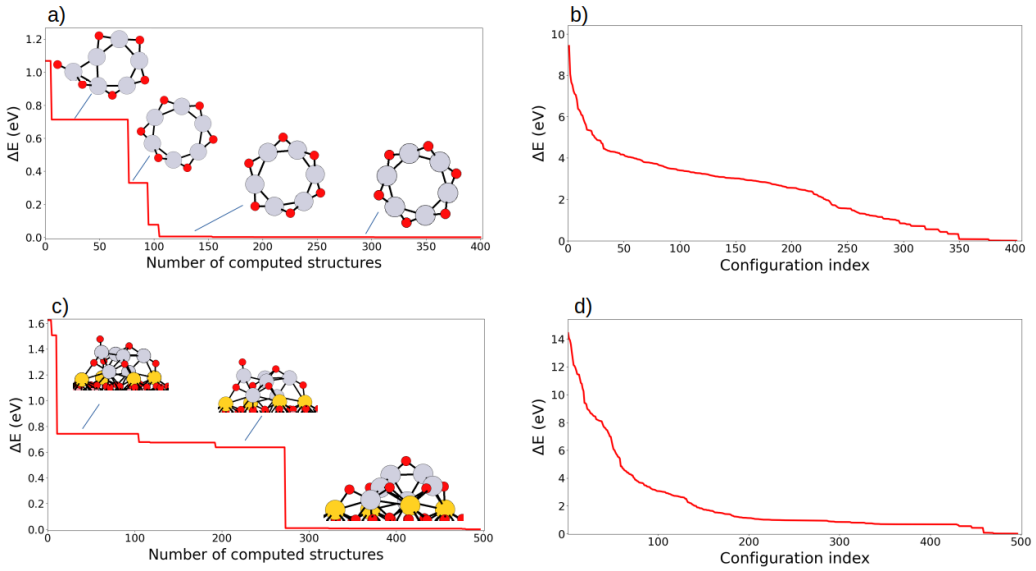

Figure 8: Energy of the most stable structure encountered as the GA calculation is progressing, relative to the putative GM structure, for a) Pt_6O_6 in gas-phase, and c) Pt_6O_6 supported on Co_3O_4. The total energy of all the structures computed during the GA optimization, ordered according to their total energy relative to the putative GM for: b) gas-phase Pt_6O_6 and d) Pt_6O_6 supported on Co_3O_4.

3.2 Results and discussion

3.2.1 Gas-phase clusters

The GA algorithm was applied to search for the most stable structures of Pt and Pt_xO_y clusters in gas-phase. The lowest energy configurations for pure Pt_x clusters (x=2, 4, 6, 7, 8, 10) are shown in Fig. 9.

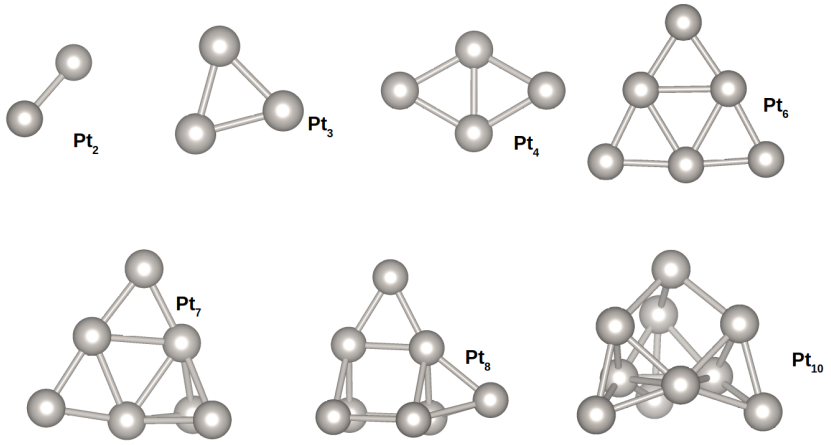

Figure 9: Global minima of metallic Pt clusters in gas- phase predicted by GA.

The computed bond length of the Pt_2 dimer is 2.31 Å, slightly shorter than what was reported experimentally [126]. For larger clusters the average bond length of Pt- Pt bond increases, reaching to 2.57 Å for Pt_{10} (see table 2).

Pt_3 is an equilateral triangle in agreement with previous studies [127, 72, 128]. Our calculations suggest that the most stable structure for Pt_4 is planar, even though the 3D tetrahedron structure is only 0.1 eV higher in energy. This result is in line with other studies [129, 72, 130] where the lowest energy Pt_4 structure is found to be either the planar or the 3D one, depending on the details of the calculation, suggesting that these two structures are indeed very close in energy. The calculations show that a 2D to 3D transition occurs from Pt_6 to Pt_7. Pt_6

Cluster	Average bond length (Å)	Cohesive energy (eV/Pt)
Pt_2	2.31	-1.91
Pt_3	2.45	-2.44
Pt_4	2.48	-2.77
Pt_6	2.50	-3.31
Pt_7	2.54	-3.39
Pt_8	2.53	-3.48
Pt_{10}	2.57	-3.75

Table 2: Average Pt- Pt bond length for each Pt cluster and the cohesive energy of the clusters normalized by the number of Pt atoms.

exhibits a 2D planar triangular structure, whereas Pt_7 has a 3D structure. The structure of Pt_7 has the same planar geometry of Pt_6 with an additional Pt atom at one corner which forms a triangle vertical to the rest planar atoms. A similar structure was predicted for Pt_7 in a recent study [78].

Pt_8 and Pt_{10} clusters exhibit a pyramid-like tetrahedral structure. The computed average Pt-Pt bond length of all the Pt clusters is found to be 2.53 Å. Our morphological studies are comparable with previous theoretical works [72, 131]. Comparing the structure of Pt clusters predicted by GA with the structures reported in other works, we found the energy of the former to be equal to or slightly lower than the latter, showing the reliability of GA.

Fig. 10 shows a plot of the cohesive energy of the gas-phase Pt metallic clusters as a function of the cluster size, computed according to Eq. 3.1.1. We considered also larger Pt NPs, containing 19 to 79 atoms, in order to partially bridge the gap between small Pt clusters and Pt bulk. In this case, we did not optimize the NPs using the GA, but we simply built the structures from bulk coordinates using the NanoCrystal tool [132] and then performed a structural optimization.

Our calculations clearly show that the cohesive energy de-

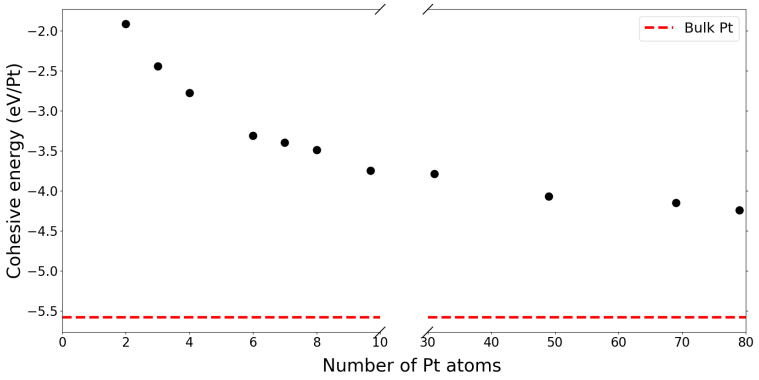

Figure 10: cohesive energy of metallic Pt clusters in gas-phase.

creases monotonically with increasing cluster size, in agreement with the work of Schneider et. al [72]. As reported by previous studies [133, 127, 72], the tendency of larger Pt_x ($x > 6$) clusters to adopt a 3D structure is related to the strong interaction between Pt atoms.

Having investigated the structure and stability of gas-phase Pt clusters, we begin finding the GM of Pt oxide clusters in gas-phase. Since there are more number of atoms and species in oxidized clusters, the quest for finding GM is more complicated now and GA should be run more.

Fig. 11 shows the lowest energy configurations of Pt_xO_y clusters.

The Pt_2O_y and Pt_4O_y oxide clusters adopt a linear and almost symmetric configuration. Larger Pt oxide clusters, Pt_xO_y ($x \geq 6$), exhibit a ring shape structure, in agreement with previous studies [72]. O atoms of the oxidized clusters, in most cases, prefer to bind to two Pt atoms, minimizing the number of O-O bonds. The exceptions are large clusters with the Pt_xO_{2x} stoichiometry (i.e. Pt_6O_{12}, Pt_7O_{14}, Pt_8O_{16}) where several O-O bonds are present.

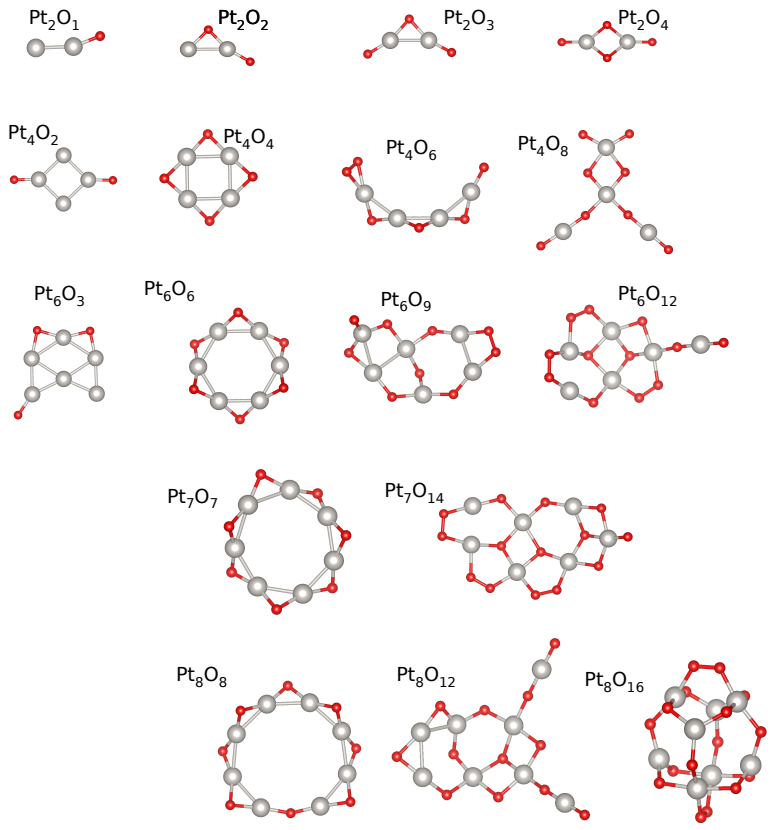

Figure 11: Global minima structures of Pt oxide clusters in gas-phase

3.2.2 Supported clusters

Similar to gas-phase clusters, the GM of clusters adsorbed on the $TiO_2(210)$ and $Co_3O_4(111)$ were found employing GA. In addition to clusters, now top layers of the slabs also should be optimized. Hence, running GA for supported clusters is more computationally demanding. Due to this, we limited the size of the clusters up to Pt_6O_{12}. Figure 12.a shows the GM of supported clusters on both types of supports.

The Pt metallic clusters adsorb more strongly on $Co_3O_4(111)$ compared to $TiO_2(210)$, and the larger the Pt cluster the stronger

the interaction with the support, with the exception of the Pt_1 on $TiO_2(210)$.

The metallic Pt_4 cluster has an almost planar structure on both supports that is similar to the gas-phase case. Instead, the Pt_6 and Pt_8 metallic clusters adopt a bilayer structure in agreement with a previous theoretical study [134]. This is in contrast with the results reported in an experimental study [135] where it is shown that Pt_4 and Pt_7 metallic clusters supported on a rutile TiO_2 (110) surface are flat and bilayer structures are observed for larger Pt clusters. The adsorption energies of the Pt metallic clusters supported on the $TiO_2(210)$ and $Co_3O_4(111)$ surfaces are computed using eq 3.1.2 and are reported in Fig. 12.b as a function of the cluster size.

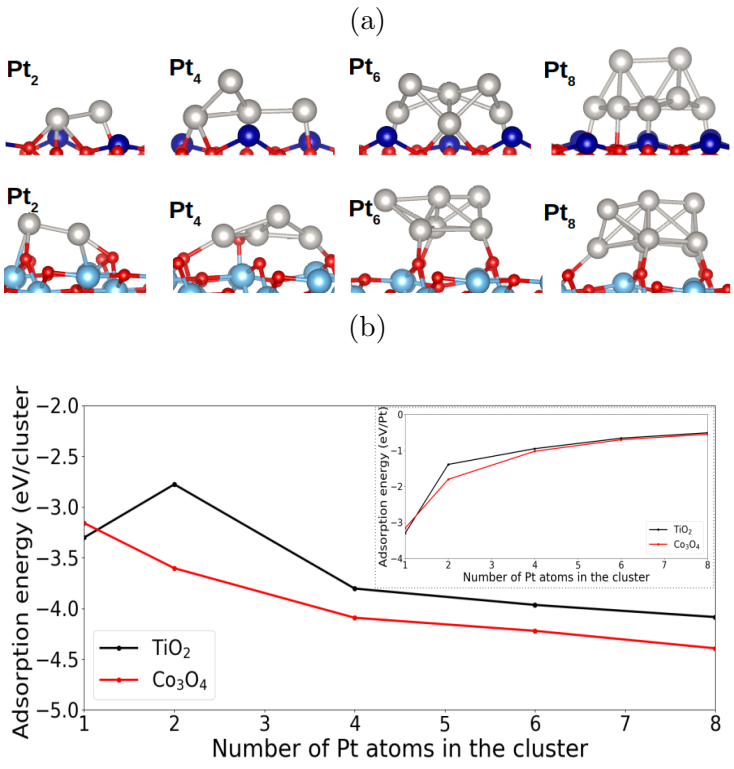

Figure 12: Global minima and Adsorption energy of Pt clusters supported on TiO_2 and Co_3O_4. The inset shows the adsorption energy per Pt atom.

In a similar study [136], Wanbayor and Ruangpornvisuti have shown that the Pt adatom binds strongly on the surface of anatase $TiO_2(001)$ (the adsorption energy was -2.6 eV), whereas other metal adatoms such as Au and Pd adsorb more weakly on the same surface (with adsorption energies of -1.51 and -1.39 eV, respectively). In the work of Wang et al. the computed adsorption energies of a single Pt atom and a dimer Pt_2 on the same anatase $TiO_2(001)$ support are found to be -2.5 and -1.6 eV, respectively.

When considering larger Pt clusters, it has been shown that the adsorption energy (using the total energy of the Pt cluster as reference) of a Pt_5 nanocluster supported on the $Co_3O_4(220)$ surface is -4.75 eV [137]. The corresponding quantities in our study for Pt_4 and Pt_6 on $Co_3O_4(111)$ are -5.47 eV and -5.65 eV.

GMs of oxidized Pt clusters are shown in Figure 13 with different oxygen content. As one can see, the structures with a high number of oxygen atoms exhibit a lower tendency for being adsorbed on the surface of the support.

The oxidized Pt_4O_y clusters exhibit 3D structures when adsorbed on both the supports. When adsorbed on the $TiO_2(210)$ surface the Pt_6O_6 cluster presents a ring-like shape, similar to the gas-phase case, whereas it assumes a 3D shape on the $Co_3O_4(111)$ support. On both the supports, the oxidized Pt_6O_9 and Pt_8O_8 clusters have a ring-like structure.

In summary, numerical details regarding the simulation of bulk and nanoscale systems were discussed. The cohesion of metallic Pt clusters and adsorption of metallic and oxide Pt clusters on the surface of the slabs were examined. Then, the performance of the GA and the process of finding the stable structure of Pt clusters were shown. Next, the GMs of the Pt and Pt oxide clusters in the gas-phase and supported on TiO_2 and Co_3O_4 were exhibited, and the structural change upon ad-

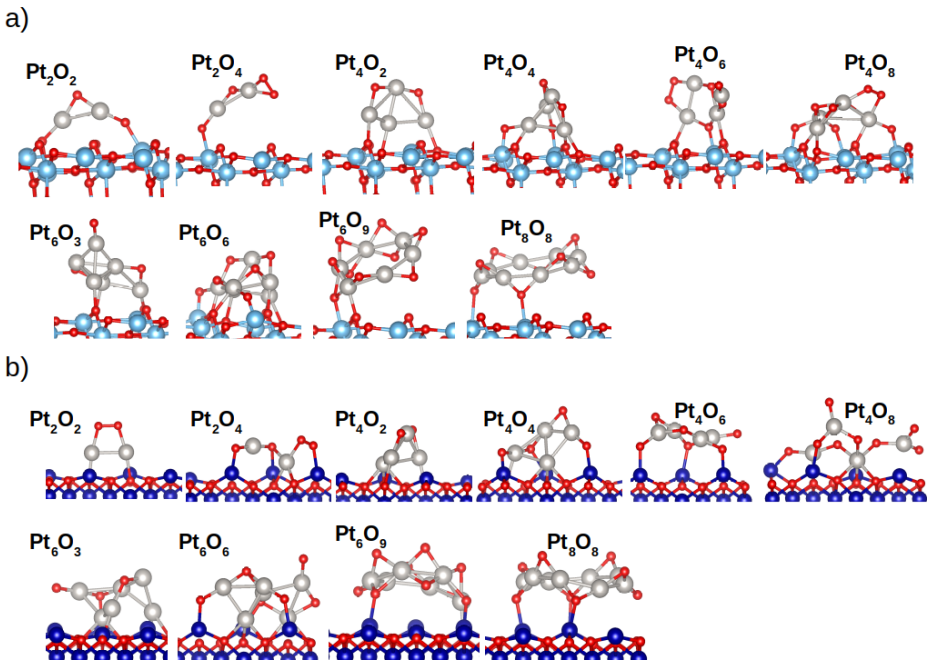

Figure 13: Global minima of Pt oxide clusters supported on a) TiO_2 b) Co_3O_4.

sorption was discussed.

4 Oxidation of Pt clusters

This chapter focuses on exploring the oxidation of Pt clusters at different adsorption states and cluster sizes. First, we discuss the oxidation of Pt clusters in the gas-phase and then we investigate the impact of adsorption on two types of surfaces on the oxidation of clusters.

To study the oxidation of metallic clusters both in the gas-phase and on the supports we computed the oxidation energy or formation energy (E_{form}) of Pt oxide systems using the following formula:

$$E_{form}(Pt_xO_y) = \frac{1}{y}\left(E(Pt_xO_y) - E(Pt_x) - \frac{1}{2}yE(O_2)\right) \quad (4.0.1)$$

Here, $E(Pt_xO_y)$ is the total energy of the oxidized cluster, $E(Pt_x)$ is the total energy of the metallic cluster, $E(O_2)$ is the total energy of the molecular oxygen and y is the number of oxygen atoms in the system.

4.1 Oxidation of gas-phase clusters

We computed formation energies of three different stoichiometries of Pt oxides: Pt_xO_x, $Pt_xO_{1.5x}$ and Pt_xO_{2x}; the results are shown in Fig. 14. E_{form} of clusters can be compared to the PtO and PtO_2 bulk (horizontal green and dark green dashed lines, respectively).

One can see from Fig. 14 that Pt_xO_y nanocluster with any content of oxygen has much lower formation energies than bulk PtO or PtO_2; and more negative E_{form} for clusters means oxidation of clusters is much more favorable than bulk Pt. Moreover, as the size of the clusters increases, the formation energy increases as well and tends to approach the bulk values, in agreement with the work of Xu et al. [72]. The affinity for oxygen

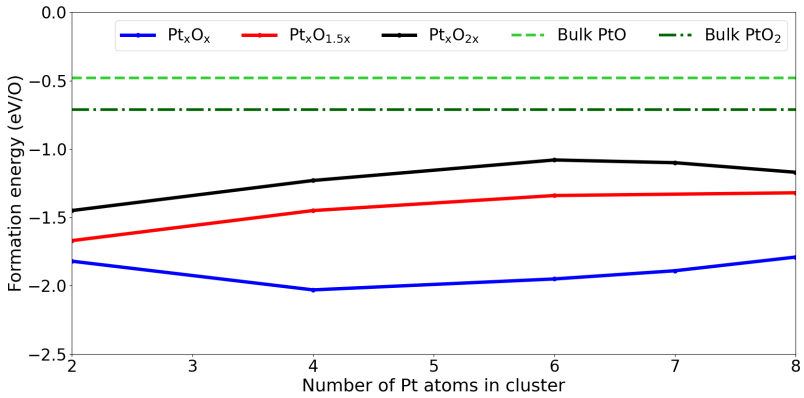

Figure 14: Formation energy of Pt oxide clusters in gas-phase as a function of cluster size.

is therefore larger for smaller Pt clusters. Easier oxidation of smaller Pt clusters can be originated from the fact that all the Pt atoms are susceptible to the environment.

Comparing the formation energy of Pt_xO_x and Pt_xO_{2x} clusters, Fig. 14 shows that at DFT level $E_{form}$of Pt_xO_x is more negative, in line with the previous report [71]. Though, this is the opposite of what happens in the bulk, where PtO_2 showed lower E_{form}. This suggests the stability of Pt_xO_x nanoscale clusters against fully oxidation into Pt_xO_{2x} at DFT condition. This is in line with a previous report [71]; however, is the opposite of what happens in the bulk, where the formation energy of PtO_2 is lower than the one of PtO [138]. Further, we found that the formation energy of clusters with $Pt_xO_{1.5x}$ stoichiometry lies between those of the other two oxides. This suggests that the oxidation of Pt clusters occurs as $Pt_x \rightarrow Pt_xO_x \rightarrow Pt_xO_{1.5x} \rightarrow Pt_xO_{2x}$. According to our findings, PtO is a stable phase in the nanoscale, while the bulk is not thermodynamically stable, as already reported in previous works [138].

4.2 Oxidation of supported clusters

E_{form} of supported clusters was calculated similar to $E_{form}$of the gas- phase clusters using equation 4.0.1. Fig. 15 shows the plot of the formation energies (E_{form}) of the supported oxidized Pt_4O_y and Pt_6O_y clusters as a function of the number of O atoms (y).

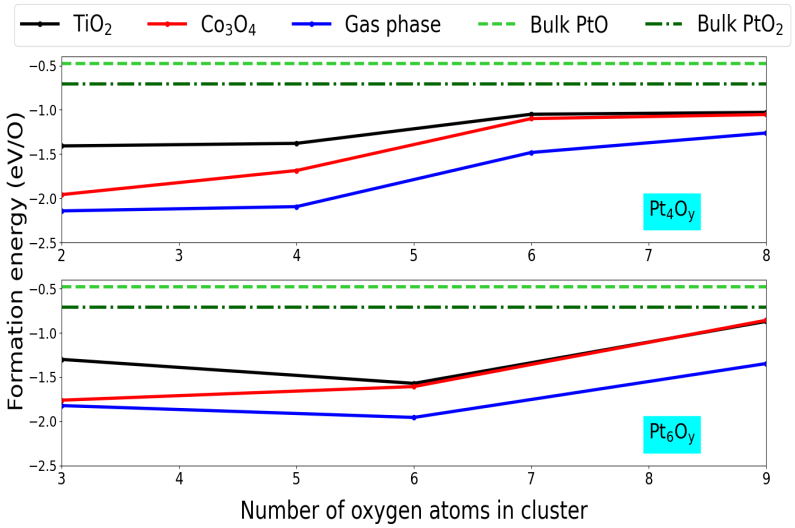

Figure 15: Formation energy of Pt_4 and Pt_6 oxide clusters as a function of oxygen content. The largest cluster considered here is Pt_6O_9.

As one can see from Figure 15, E_{form} of clusters supported on the $Co_3O_4(111)$ and $TiO_2(210)$ surfaces are higher than those in gas-phase; this suggests that it is easier to oxidize gas-phase Pt clusters compared to supported Pt clusters. Also, there is a trend in the oxidation of supported Pt clusters similar to the gas-phase case: Smaller Pt clusters are easier to oxidize compared to larger clusters. Interestingly, a reverse size dependency of oxidation was found for Cu clusters upon adsorption on the Al_2O_3 surface [73]: the smaller the clusters the more difficult it was to oxidize the Cu clusters in the gas-phase, while the opposite happened when they were adsorbed on the support.

A significant finding of this investigation is the comparison shown in Figure 15 between the E_{form} of oxide nanoclusters and

E_{form} of bulk phases. For both gas-phase and supported clusters, the E_{form} is remarkably lower than the E_{form} values of bulk PtO and PtO_2. This implies that small gas-phase or supported Pt clusters are much easier to oxidize rather than Pt bulk. This finding can explain recent experimental evidence of the oxidation of Pt clusters supported on $Co_3O_4(111)$ at conditions of temperature and pressure where oxidation of bulk Pt does not happen [139].

The next important finding is that the effect of the type of support varies by cluster size: The E_{form} of the clusters with a high oxygen content (Pt_4O_6, Pt_4O_8, Pt_6O_6, Pt_6O_9) is very weakly affected by the type of support, whereas some significant differences can be seen at low oxygen content.

The atoms included in the GA optimization include both the atoms of the clusters and also the oxygen atoms of the first layer of the support. We included the oxygen atoms from the surface in GA structural optimization to see if oxidation of Pt clusters by the surface is favorable. However, this was not observed in any of the GMs found by GA. So, the creation of oxygen vacancy by clusters is not favorable. To rationalize this finding, we computed the cost of creating an oxygen vacancy on the pristine brookite surface as well at the interface between the brookite surface and the Pt_6 cluster; the lower values we obtained were 3.52 eV and 3.14 eV, respectively. On the other hand, the formation energy of Pt_6O_y per oxygen atom is never lower than -2 eV, as shown in Figure 15. This means that oxidizing Pt clusters by gas O_2 are thermodynamically favorable, while oxidizing Pt clusters via oxygen from the support is not favorable. Furthermore, to support this conclusion, we created a surface oxygen vacancy in the proximity of the TiO_2/Pt_6 interface and adsorbed the lattice oxygen atom on the Pt_6 cluster. The energy cost with respect to the pristine surface is +1.18 eV, in

line with the previous estimate. This explains why in the global optimization by the GA we never found structures where the Pt clusters were oxidized via the formation of oxygen vacancies on the support.

4.3 Ab initio thermodynamics

Now we can focus on the thermodynamic stability of the oxidized Pt clusters both in gas-phase and supported on $Co_3O_4(111)$ and $TiO_2(210)$ surfaces. The change of the Gibbs free energy of formation as a function of the chemical potential of oxygen, $\Delta\mu_O$ was calculated using equation 2.3.6. The phase diagrams are reported in Figure 16.

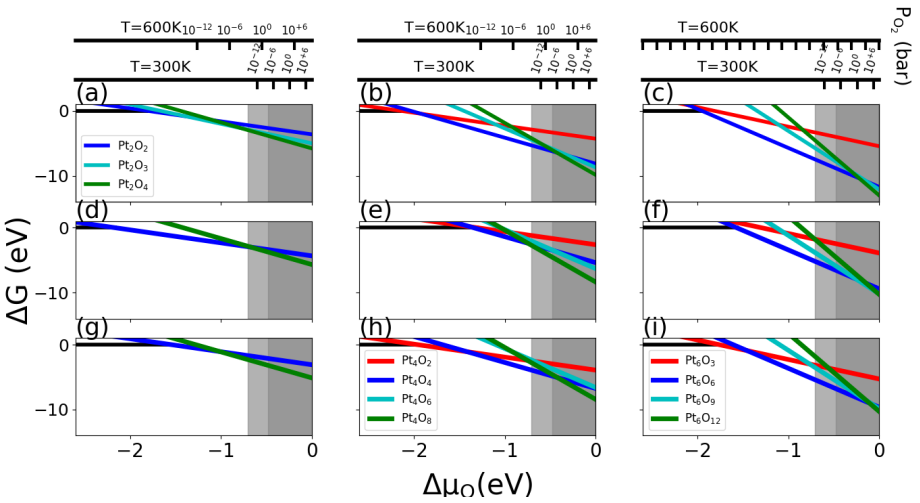

Figure 16: Gibbs free energy of formation of clusters in gas-phase (a-c), supported on TiO_2 (d-f) and supported on Co_3O_4 (g-i). The three panels on the left refer to Pt_2O_x, the three panels in the middle correspond to Pt_4O_x and the three panels on the right refer to Pt_6O_x clusters. The light and dark-shaded areas demonstrate the region of stability of bulk $\beta - PtO_2$ and PtO, respectively.

According to equation 2.3.4 and 2.3.5, lower partial pressure of oxygen and/or higher temperatures correspond to more reducing conditions and lower values of $\Delta\mu_O$ (left side of the phase

diagrams). On the other hand, higher partial pressure of oxygen and/or lower temperatures refer to more oxidizing conditions and higher values of $\Delta\mu_O$ (right side of the phase diagrams). ΔG of all the Pt oxide clusters were compared with metallic Pt clusters. The black line at ΔG=0 represents the metallic state of the system ΔG of oxide clusters plotted with respect to this line. To reach a very low $\Delta\mu_O$, where the most stable phase of the three clusters sizes examined is the metallic phase (Pt_x), the environment should be extremely reducing. In all cases, reducing to metallic state happens at values of $\Delta\mu_O$ lower than -1.5 eV, which is far from practical use; $\Delta\mu_O$=-0.62 eV is reachable at UHV conditions: 10^{-12} bar and room temperature, and to reach a more negative $\Delta\mu_O$ like -1.32 eV temperature should raise to 600 K.

With the increase in $\Delta\mu_O$, oxidized forms of the clusters become thermodynamically stable. The transition to the Pt_xO_{2x} stoichiometry takes place in all cases at negative values of $\Delta\mu_O$. This suggests that at ambient conditions i.e. pressure 1 bar and room temperature, which is corresponding to $\Delta\mu_O$=-0.27 eV, the clusters can be fully oxidized.

Comparing clusters of different sizes, we can see that the transition to the fully oxidized form, Pt_xO_{2x}, requires higher values of $\Delta\mu_O$ for larger clusters. This is consistent with the results displayed in Figure 15, since smaller clusters show more affinity for oxygen. Furthermore, Pt_xO_x stoichiometry is stable in a larger range of chemical potential for larger clusters. This is a common trend for gas-phase and supported clusters. The most evident difference comes from the Pt_6 case, where the formation energy per oxygen atom is considerably lower in the gas- phase compared to the supported clusters. Comparing clusters supported on TiO_2 and Co_3O_4, the differences are minor. These are just another representation of the same findings already highlighted in the previous Section when discussing the

E_{form}in Figure 15. Another interesting finding is that the stability range of the $Pt_xO_{0.5x}$ and $Pt_xO_{1.5x}$ phases is considerably smaller than the Pt_xO_x and Pt_xO_{2x} phases. This is evident also in Figure 17, where the stable phases of the same 9 systems discussed in Figure 16 are shown as a function of temperature and pressure. It is predicted from these phase diagrams that at room temperature and at 600 K, Pt nanoclusters are oxidized in the full range of pressures examined, down to UHV conditions. For Pt_2 and Pt_4, the Pt_xO_{2x} phase appears at room temperature, while the Pt_xO_x phase dominates at 600 K. For the larger Pt_6, on the other hand, only the Pt_xO_x phase appears in the temperature range of 300-600 K.

Similar phase diagrams have been reported by Xu *et al.* for the gas-phase and stationary small Pt nanoclusters (Pt_x, x = 1, 2, and 3), and their findings is in line with the ones reported here [71]. Akhil S. Nair *et al.* reported a similar oxidation trend for Pt_7 [78].

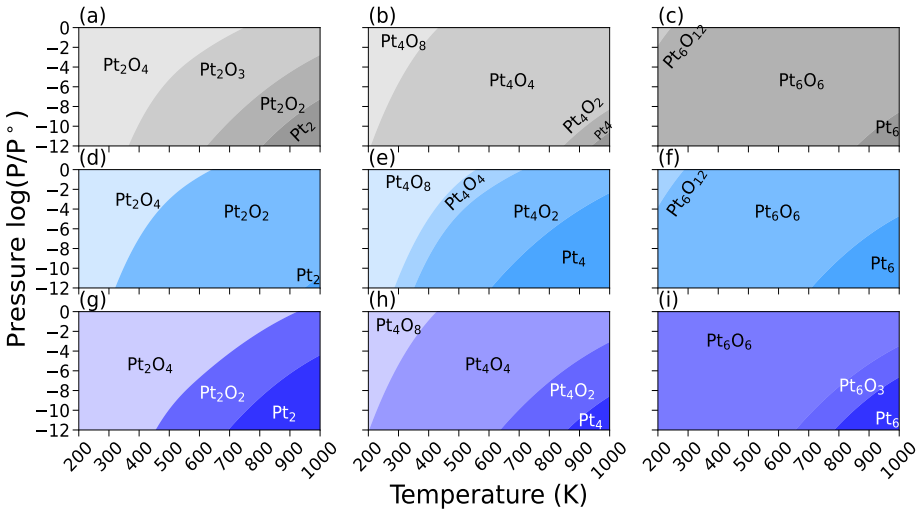

Figure 17: T-P_{O_2} phase diagram of Pt oxide clusters (a-c) in gas-phase (d-f) supported on TiO_2 and (g-i) supported on Co_3O_4.

Our predictions agree with experimental observations. Ono

and coworkers [140] reported the reduction of PtO_2 NPs supported on TiO_2 to metallic Pt at a temperature above 550 K in UHV, while some of the Pt NPs supported on SiO_2 remained oxidized up to 750 K in UHV. The same authors also observed higher temperatures for oxygen desorption on NPs compared to Pt(111), and higher oxygen desorption temperature for smaller nanoparticles [141]. Moreover, the formation of interfacial PtO_x was observed on Pt NPs at temperatures higher than 400 K for low oxygen pressure (10^{-6} bar) on Co_3O_4 [139].

Based on the above discussion, at industrially relevant conditions for catalytic oxidation ($T \sim 300 - 600$ K, $P_{O_2} \sim 0.1 - 1$ bar), we predict supported nanoclusters to be in an oxidized state, on both types of supports considered in this work. Small clusters such as Pt_2O_x are found in a fully oxidized state (i.e. Pt^{4+}). As the size of the clusters increases, Pt clusters are predicted to be both in Pt^{4+} and Pt^{2+} oxidation states (higher oxidation state is reached at lower temperatures). As to the largest clusters (Pt_6O_x), these are mostly found in Pt^{2+} oxidation state only, indicating the role of cluster size in the oxidation state.

Even though in the present work we assumed the system to be in contact with an atmosphere containing only oxygen, in realistic conditions other compounds such as water can also be present and can adsorb and dissociate on the oxide surfaces. In the case of the Co_3O_4 (111) surface, considering oxygen chemical potentials down to -0.5 eV, the surface is partially hydroxylated even in ultra-high vacuum (UHV) conditions at 423 K [122]. The hydroxylation of the brookite TiO_2(210) surface has been investigated in a recent work [142]. While hydroxylation of the surface can have significant effects on the structural and catalytic properties of supported clusters, we did not investigate these effects in the present model.

4.4 Bader charge

There are different methods to partition the charge density and map them into individual atoms. To compute the charge transfer between the surface and clusters we used the Bader partitioning scheme employing Henkelman's code [143]. In this scheme, the electron density is divided at zero flux surfaces and results depend little on the employed basis set.

First, we computed the Bader charge on Pt and O atoms of Pt oxide clusters in the gas-phase. This analysis shows that the amount of transferred charge from Pt to O atoms in the clusters varies from +0.5 to +1.2 e per Pt atom. To have a reference for assigning the oxidation states, we computed the difference between the Bader charge of Pt bulk (Pt^0) and the Bader charges in bulk Pt^{2+} and Pt^{4+} oxides (Δq). In PtO (Pt^{2+}), Δq on Pt is 0.99 e, in α-PtO_2 (Pt^{4+}) 1.69 e, in β-PtO_2 (Pt^{4+}) 1.73 e and in $\beta'-PtO_2$ (Pt^{4+}) 1.81 e. The fingerprint for the Pt^{2+} oxidation state is therefore a value of Δq around 1 e, while for Pt^{4+} it is 1.7- 1.8 e. It is clear from Table 3 that for clusters with a fixed number of Pt_x atoms (x=2, 4, 6) Δq, and thus the oxidation state of Pt, increases with increasing the number of O atoms. Since Δq varies between 0.56 and 1.22 per Pt atom, Pt atoms never reach the formal oxidation state of Pt^{4+} found in bulk of PtO_2 oxides. These values for the Bader charges are in agreement with previous studies where some of the same clusters have been considered [74].

Next, we focus on the charge transfer between the Pt clusters and the Co_3O_4 and TiO_2 supports. The Bader analysis shows that the binding of the clusters on both types of supports leads to small charge rearrangements at the Pt cluster/oxides interface (maximum +0.07 e/Pt on TiO_2 and −0.23 e/Pt on Co_3O_4). Moreover, the values of Δq of the Pt atoms of the supported clusters regarding the number of oxygen atoms fol-

Pt_xO_y	spin	Δq (e)	Pt_xO_y	spin	Δq (e)	Pt_xO_y	spin	Δq (e)
Pt_2O_2	0	+0.59	Pt_4O_6	0	+0.77	Pt_7O_7	0	+0.68
Pt_2O_3	0	+0.64	Pt_4O_8	0	+1.22	Pt_7O_{14}	2	+1.05
Pt_2O_4	0	+0.88	Pt_6O_6	0	+0.69	Pt_8O_8	0	+0.69
Pt_4O_2	2	+0.56	Pt_6O_9	0	+0.89	Pt_8O_{12}	1	+0.70
Pt_4O_4	0	+0.69	Pt_6O_{12}	0	+0.98	Pt_8O_{16}	0	+1.17

Table 3: Average positive Bader charge for each Pt atom and total magnetization (number of up minus down electrons) of gas-phase clusters.

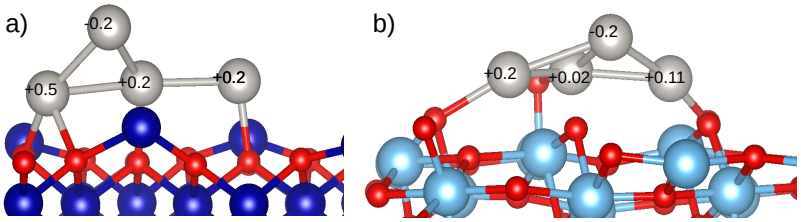

Figure 18: Charge distribution on Pt_4 cluster adsorbed on a) Co_3O_4 and b) TiO_2

low a trend similar to the one observed in the gas-phase case. As an example, we have considered the case of the metallic Pt_4 cluster adsorbed on the Co_3O_4 and TiO_2 oxides, as shown in Figure 18. The positive charge on the metallic cluster is slightly more on Co_3O_4 than on TiO_2, yet this charge is less than 0.5 (e)/ Pt. This small amount of charge is transferred from the metallic cluster to the supports. Here, the values of Δq per Pt atom are 0.16 and 0.04 e on Co_3O_4 and TiO_2, respectively. Similar behavior has been reported in previous studies: Ammal and coworkers reported Bader charge differences of +0.1 e/Pt for Pt_3 cluster supported on rutile TiO_2 [144]; the same has also been observed for a Pt_5 cluster on the $Co_3O_4(220)$ surface [137]. These results suggest that the supports have little influence on the electronic properties of the supported metallic and oxidized subnano Pt clusters. A similar small charge transfer was pre-

dicted on $TiO_2(110)$ for Ag single atoms [145].

For a deeper insight, we provide an analysis of the electronic structure of gas-phase and supported clusters based on the d-band model.

4.5 Electronic structure of the Pt clusters: the d-band model

To find a correlation between the formation energy of the oxidized clusters and their electronic structure, we used the d-band model [146, 147, 148]. We computed the d-band center of metallic Pt_x and oxidized Pt_xO_x clusters with respect to their Fermi level, and we tried to correlate these quantities to the E_{form} of the Pt_xO_x clusters. The data are reported in Table 4 and are graphed in Figure 19.

Cluster size	d-band center for Pt_x (eV)	d-band center for Pt_xO_x (eV)	E_{form} of Pt_xO_x (eV)
2	-1.35	-1.97	-1.82
4	-1.60	-2.40	-2.03
6	-1.86	-2.30	-1.95
7	-1.86	-2.26	-1.89
8	-1.92	-2.25	-1.79
10	-1.79	-	-

Table 4: d-band center of metallic and oxide clusters compared to the size and formation energy of the clusters. Regarding Pt_{10}, the GM of the oxidized cluster was not available.

The center of the d-band of metallic Pt_x clusters approached more negative values as the size of the cluster increased, at least up to Pt_8, while Pt_{10} does not follow this trend. The center of the d-band of the oxidized Pt_xO_x clusters does not follow a clear trend with the size of the cluster.

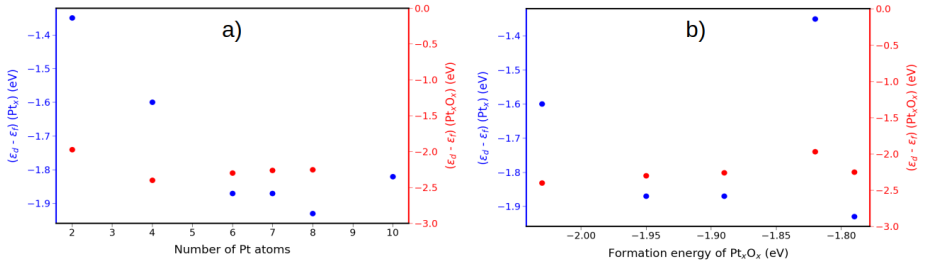

Figure 19: a) d-band center of metallic (Pt_x, left y-axis) and oxidized (Pt_xO_x, right y-axis) clusters as a function of the size of the cluster; b) d-band center of metallic (Pt_x, left y-axis) and oxidized (Pt_xO_x, right y-axis) clusters as a function of the formation energy of the Pt_xO_x clusters.

Plotting the formation energy of the Pt_xO_x clusters against the center of the d-band, we do not see a clear correlation. We, therefore, conclude that the d-band model, developed to describe the interaction of adsorbates on metallic surfaces, does not seem to describe well the properties of very small (sub-nanometer) Pt_xO_x clusters. This is probably due to the very different nature of these systems since we are studying the adsorption of metals on oxides.

In this chapter, we investigated the oxidation of Pt clusters as a function of cluster size and type of support. It was found that Pt shows more affinity for oxygen in the nanoscale compared to the bulk phase. Further, smaller Pt clusters are easier to be oxidized. The type of support can affect the oxidation of Pt clusters, but not majorly in a highly oxidative environment. Ab initio thermodynamics calculations showed that higher pressure of oxygen and lower temperatures favor the oxidation of Pt clusters. The outcome of chapters 3 and 4 was published in the journal of Physical Chemistry C and is accessible at https://doi.org/10.1021/acs.jpcc.2c02176.

5 CO oxidation via Mars-Van Krevelen

In this chapter, we examine the kinetics of CO oxidation over Pt clusters. The elementary steps of the oxidation reaction were simulated on different Pt cluster sizes supported on TiO_2 and Co_3O_4. First, we consider CO oxidation through the MvK mechanism, which involves the oxygen atoms from the support lattice.

To explore the kinetics of reactions and find activation barriers, transition states of CO oxidation mechanisms were searched by means of the climbing-image nudged elastic band (CI-NEB) scheme. Using the Broyden optimization scheme, the reaction paths were optimized until the error on images was less than 0.05 eV/Å, and a minimum number of 9 images was considered for different paths. We define the adsorption energy ($E_{ads(CO)}$) of CO molecules on the system as below:

$$E_{ads(CO)} = (E(system@nCO) - E(system) - nE(CO))/n \tag{5.0.1}$$

where E(system@nCO), E(system) and nE(CO) are the total energies of combined system nCO/Pt$_x$/support, the Pt$_x$/support system and CO molecules, respectively and n is the number of adsorbate CO molecules.

From now on, in the presence of oxygen vacancies (i.e. reduction of Ti^{4+} to Ti^{3+}) on the brookite surface, the addition of Hubbard term (U=3.5 eV) is necessary to calculate the formation energy of oxygen vacancy. A Hubbard term of 3 eV was already considered for all the calculations on Co_3O_4.

The formation energy of the oxygen vacancy (FE_{O_v}) in the lattice is defined as [149]:

$$FE_{O_v} = (E(stoi@system) + 1/2E(O_2) - E(reduced@system)) \tag{5.0.2}$$

where E(stoi@system) and E(reduced@system) represent the total energies of the stoichiometric Pt/support system and reduced Pt/support system, respectively.

As mentioned in section 1, two oxidation mechanisms are considered in the present work: MvK and LH. First, we investigate CO oxidation through MvK mechanism, and in the next chapter, we will discuss the LH oxidation mechanism.

5.1 Adsorption of CO and O_2

The first step of studying CO oxidation is to find out how CO molecules react with the surface and Pt clusters. The bond strength of CO on the catalyst is important since too strong bond strength could lead to CO poisoning and impair the Pt nanoparticles (NPs) catalysts [150]. On the other hand, in case of weak interaction between CO and catalyst, there would be low coverage of CO and hence the oxidation reaction would fail. According to the Sabatier principle, the maximum reaction rate is reachable when the bond strength between the adsorbate and the surface is of medium magnitude. There have been efforts to study and control the adsorption of CO on Pt systems [151, 152, 153]. The bond length of CO on bulk Pt depends on the adsorption site [154, 155] and surface strain [156]. Reducing the size of the bulk Pt system to Pt NPs and a consequential change in the structure of the system, as well as CO coverage, are found to have a considerable impact on CO adsorption [153, 157].

While CO adsorption on pristine TiO_2 is not thermodynamically favorable, it is favorable on Co_3O_4 surface [158]. In the present work, we use a (111) termination, which exposes Co^{+2}, three-fold and two-fold oxygen atoms. Table 5 summarizes the computed adsorption energy of CO on different sites of Co_3O_4 surface.

Adsorption of CO is favorable on Co^{+2} cations and 3-fold co-

Adsorption site	Bond length ($\mathring{A}$)	Adsorption energy (eV)
Co^{+2}	1.93	-1.04
O_{2c}	CO_2 desorption	-
O_{3c}	1.29	-0.78

Table 5: CO bond length and adsorption energy of CO on pristine Co_3O_4 (111). O_{2c} and O_{3c} refer to oxygen atoms in the lattice with a coordination number of 2 and 3.

ordinated lattice oxygen atoms. We found that although bridge oxygen atoms of Co_3O_4 lattice react with CO and form CO_2, the activation barrier we calculated for this step was more than 1.4 eV. This was also experimentally observed on the same surface [159]. The highest activation barrier for CO oxidation on Co_3O_4 (110) surface was predicted to be 1.7 eV [160]. So, CO oxidation over Co_3O_4 would be slow and thus we skip investigating the oxidation path on Co_3O_4 surface.

Pt_6 and Pt_4 clusters supported on TiO_2 and Pt_6 supported on Co_3O_4 were probed by CO molecule in order to find the favorable sites for CO molecule adsorption and predict the CO coverage in the catalytic condition. The top sites of Pt atoms, interfaces between Pt clusters and support, and metallic and oxygen atoms of support nearby the clusters were examined. CO molecules adsorb strongly on supported Pt clusters. The most stable sites for the adsorption of CO were found to be on top of the Pt atoms.

The adsorption energy of a single CO molecule on Pt_6/TiO_2 varied from -1.2 to -2.3 eV with an average of -1.86 eV, in line with previous work [151]; showing that interaction between CO and nanoscale Pt systems is stronger than bulk Pt on which CO adsorption energy is within the range of -1.22 $\sim$ -1.66 eV, depending on the adsorption site [156]. For a smaller cluster, i.e. Pt_4/TiO_2, the average adsorption energy of one CO on different sites was calculated to be -1.95 eV. In full CO coverage, the

average adsorption energy was computed to be -2.13 eV/CO. Adsorption of one CO on Pt/TiO_2 adatom is exothermic by -2.28 eV. On Co_3O_4, Pt- CO interaction was found to be slightly stronger: -1.30 to -2.57 eV on Pt_6 with an average of -2.06 and -2.80 eV on Pt adatom. As one can see, the interaction of CO is stronger with smaller Pt systems. Similarly, CO adsorption was found to be stronger on Pt_5 compared to Pt_{19} supported on Fe_3O_4 [161]. Stronger CO adsorption as well as more cationic sites were observed on Pt particles supported on TiO_2 particles [50].

On the same Pt_6/TiO_2 system, now fully covered by CO (1 CO per Pt), the average adsorption energy was calculated to be -1.85 eV/CO. For Pt_4/TiO_2 under full CO coverage, the average adsorption energy was -2.13 eV/CO. As mentioned above, by increasing CO content on Pt_6 and Pt_4/TiO_2, the average adsorption energy of CO decreased from -2.3 to -1.85 and -2.13 eV, respectively. Figure 20 shows how CO bond strength changes with CO coverage.

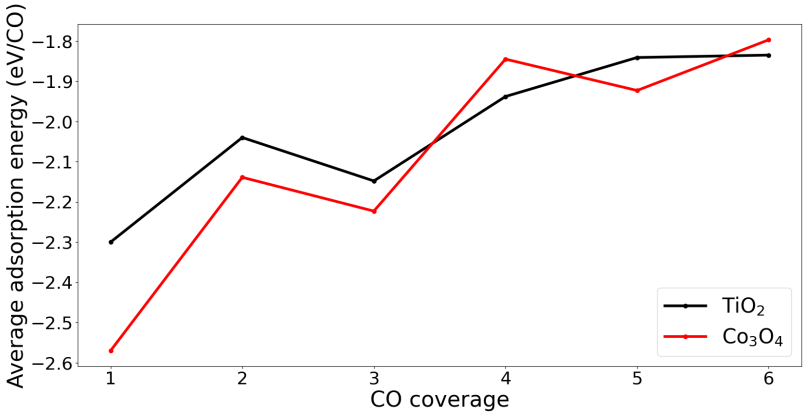

Figure 20: Average adsorption energy of CO molecule on Pt_6 supported on TiO_2 and Co_3O_4.

On Co_3O_4, by adding up to 6 CO molecules, the average adsorption energy of CO increased from -2.57 to -1.80 eV. Sangnier

et. al. reported a similar trend regarding the weakening of the CO- Pt bonding energy as the CO coverage increased on Al_2O_3 supported Pt catalyst [162].

The structure of the clusters underwent a severe deformation after covering the Pt clusters fully with CO molecules, as shown in Figure 21.

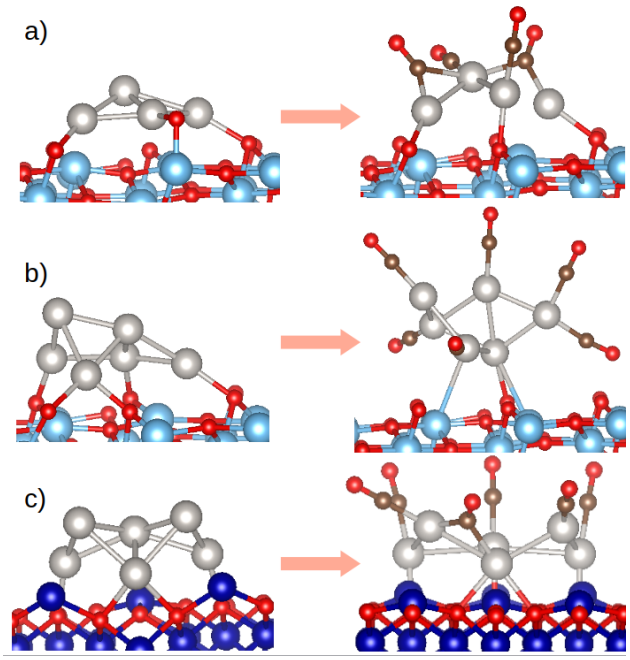

Figure 21: Structure modification of Pt clusters after being covered by CO, a) Pt_4/TiO_2 b) Pt_6/TiO_2 and c) Pt_6/Co_3O_4.

While full CO coverage induced little deformation on the Co_3O_4 supported cluster, it led to the uplifting of the Pt_6/TiO_2 cluster, and in the case of Pt_4/TiO_2, the cluster split into monomer and trimer Pt. Adsorption-induced structural change of the platinum particles supported on Al_2O_3 was observed in a previous experiment as well [163]. CO-induced cluster dissociation was also predicted for Au/CeO_2 catalyst[164]. This is opposed to what was observed on Fe_2O_3, on which adsorption of CO stabilized Pt dimers against dissociating into atomic Pt and induced

agglomeration of Pt atoms into small clusters [153].

Since the adsorption of CO on Pt clusters is more exothermic than the adsorption of O_2 (-1.35 eV), if the partial pressure of the two gases is similar, the catalyst would have higher coverage of CO. Yet, we found the favorable adsorption sites for O_2 molecule on Pt clusters to be interfacial sites (adsorption energy varied from -0.71 to -1.35 eV). This opens a window into the possibility of CO oxidation via the LH mechanism on small Pt clusters.

5.2 Ab initio thermodynamics

Having investigated the CO adsorption energy and possible sites on Pt clusters, now we need to know about the adsorption strength and coverage of CO on Pt clusters at finite pressure of CO. Having the total energy of Pt_6/TiO_2 and Pt_6/Co_3O_4 cluster covered by 1 to 6 CO molecules, we can compute the Gibbs free energy of CO adsorption on Pt_6 cluster as a function of the chemical potential of CO ($\Delta\mu_{\mathrm{CO}}$) using equation 2.3.5. The result is plotted in Figure 22. As one can see, for less negative values of $\Delta\mu_{CO}$ (lower temperature, the higher pressure of CO: CO rich environment) CO coverage is higher, and vice versa.

The range of $\Delta\mu$(CO) in which we are interested varies from -0.5 to -1 eV (corresponding to the experimental catalytic condition of temperature 300 $\sim$ 500 K and CO pressure of 0.2 $\sim$ 0.8 bar). Within the mentioned range of $\Delta\mu_{CO}$, and in presence of only CO, the Pt cluster is fully covered by CO molecules regardless of the type of support, in line with previous study [165] and experiment [166].

Further, we need to know what happens to an oxidized cluster when it is exposed to CO. So, similar to metallic cluster, we studied the CO adsorption on Pt_6O_6 and Pt_6O_3 clusters supported on both types of oxides. When exposed to CO molecules,

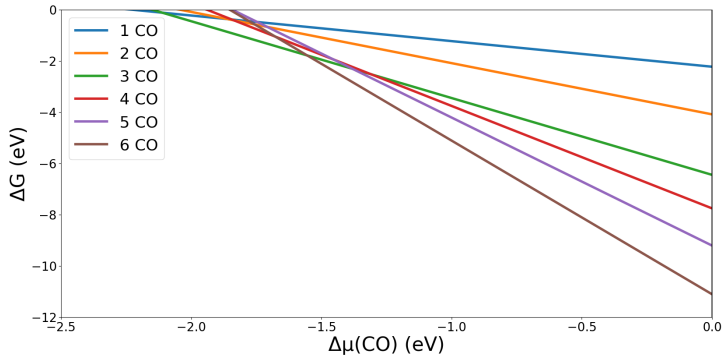

(a)

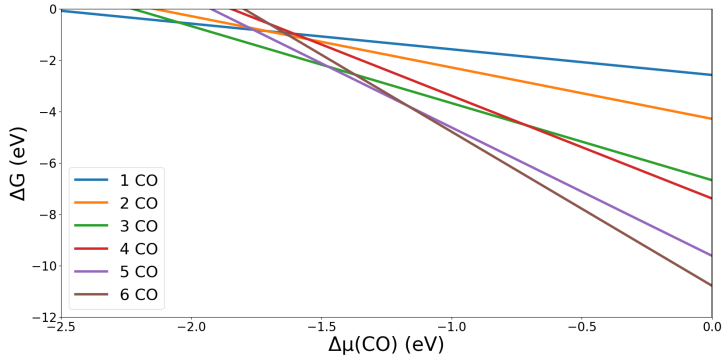

(b)

Figure 22: Different coverage of CO on a) Pt_6/ TiO_2 and b) Pt_6/ Co_3O_4 system. The line corresponding to the metallic systems is $\Delta G = 0$. Right side of the plot corresponds to lower temperature and higher CO pressure, and vice versa.

some of the chemisorbed oxygen atoms of the Pt oxide cluster react with CO immediately and form $*CO_2$ (adsorbed CO_2) or CO_2(g). This reduction reaction is non-activated and occurs after a local optimization, meaning the oxidized clusters in contact with CO(g) would be partially reduced. On the other hand, recalling the results from chapter 4, we found that small Pt clusters were predicted to be fully oxidized in presence of oxygen only. Now we are interested to know how Pt clusters interact with CO and oxygen in a more practical condition, where both

gas-phase species (O_2 and CO) are available.

Using the total energy of clusters with different content of CO and oxygen and equation 2.3.5, we constructed a phase diagram for each type of support as a function of the chemical potential of oxygen ($\Delta\mu_O$) and CO ($\Delta\mu_{CO}$), shown in Figure 23.

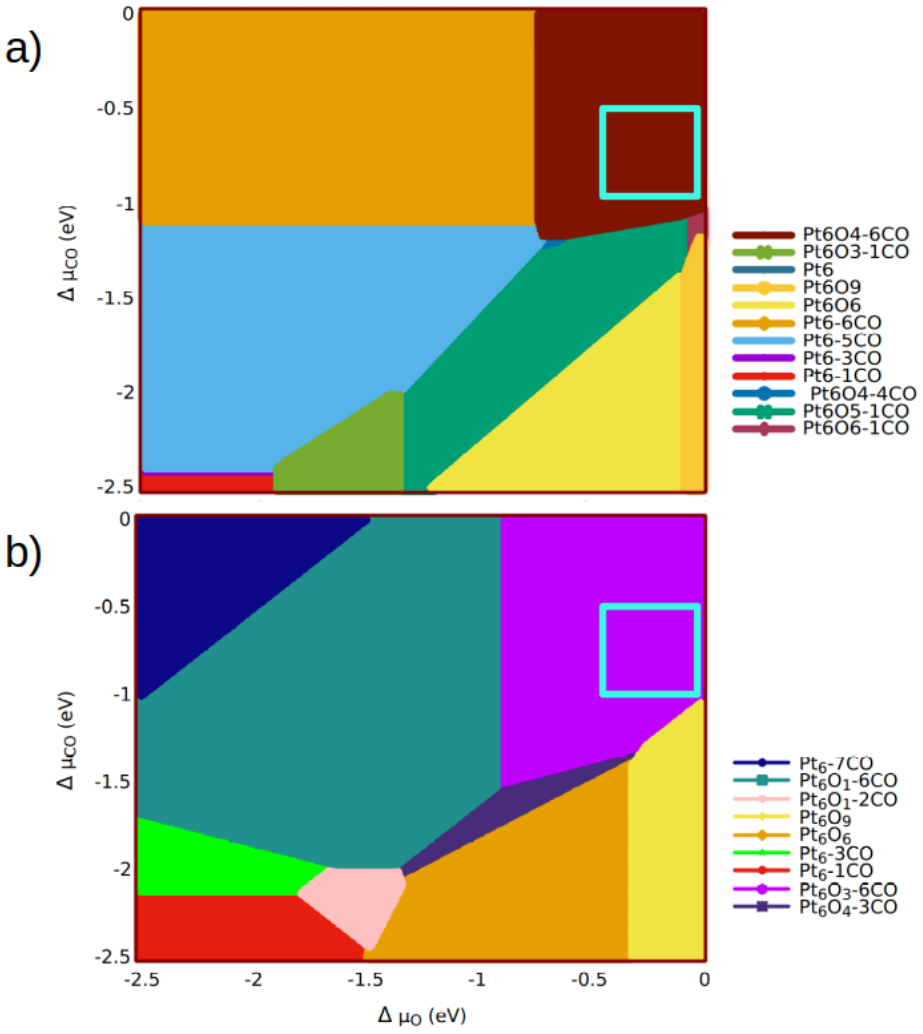

Figure 23: Phase diagram of a) Pt_6/Co_3O_4 and b) Pt_6/TiO_2 cluster in thermodynamic equilibrium with gas-phase O_2 and CO. Here more negative values of $\Delta\mu$ correspond to the higher temperature and lower pressure of the species.

Converting the experimental condition of CO oxidation reac-

tion into chemical potential values of CO and oxygen using equation 2.3.4, we obtain a range of $\Delta\mu$ for gas-phase species: $\Delta\mu_{CO}$ from -0.5 to -1 eV and $\Delta\mu_O$ from -0.3 to -0.5 eV. This window of $\Delta\mu$ is shown on both phase diagrams, where Pt_6O_4/Co_3O_4 and Pt_6O_3/TiO_2 are highlighted. Accordingly, in presence of CO and O_2 within the experimental range of $\Delta\mu$, Pt clusters supported on TiO_2 and Co_3O_4 are partially oxidized and fully covered by CO molecules.

So far our findings are based on thermodynamics only. Hence, finding Pt clusters in a partially oxidized state is energetically possible. An experimental study reported the partial oxidation of the Pt NPs ($\sim$ 1 nm) in catalytic condition [50]. However, this could be different within subnano regime. Now, we move one step forward to study the systems more realistically by taking the kinetics of the reaction into account.

5.3 CO oxidation on supported PtO_x clusters

In the previous section, we found $Pt_6O_3/6CO$ structure to be thermodynamically stable on TiO_2 under experimental conditions. Now we examine this system by considering kinetics, trying to find out if the cluster will remain oxidized. For this purpose, we investigated the interaction between the chemisorbed oxygen atoms on the cluster and adsorbed CO molecules. NEB calculations for $Pt_6O_3/6CO$ showed that adsorbed CO molecules on the Pt cluster react with chemisorbed oxygen atoms and form CO_2. Three oxygen atoms on the cluster react with CO molecules and form CO_2. For the complete reduction of the oxidized cluster, the maximum barrier was found to be 1.65 eV, see Figure 24. Formation and desorption of the first CO_2 show the lowest activation barriers. Formation of CO_2 from second oxygen requires surmounting a higher energy barrier of 1.6 eV. Removal of the last oxygen has a slightly lower activation energy

(1.55 eV for the formation of carbon monoxide).

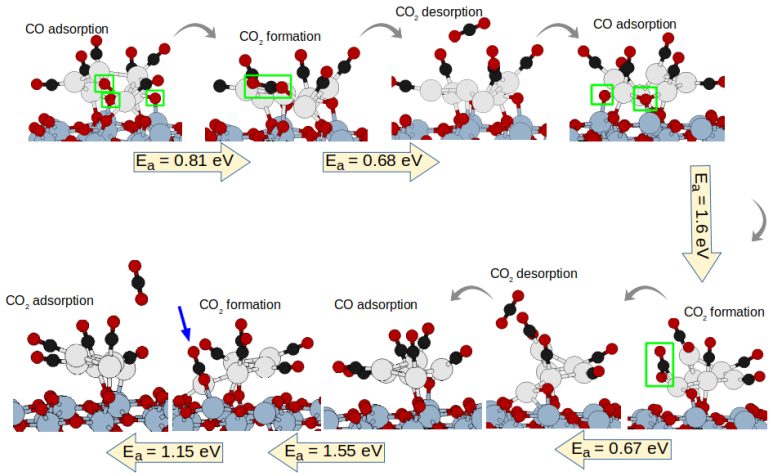

Figure 24: Reaction between adsorbed CO and atomic oxygen on a partially oxidized Pt cluster.

Based on what was mentioned, it is predicted that at finite temperature and CO pressure, a partially oxidized Pt cluster will be mostly reduced. Our attempt to re-oxidize the cluster when it is already covered with CO failed: after the catalyst is reduced, adsorption of CO is thermodynamically more favorable on the reduced system rather than adsorption of O_2. After a partial reduction, local optimization of O_2 adsorbed on the partially oxidized cluster led to the desorption of molecular oxygen, meaning this structure is not a local minimum. Hence, we predict that the reduction of the partially oxidized cluster is irreversible. An experimental attempt to reduce a pre-oxidized Pt cluster ($\sim$ 1 nm) supported on TiO_2 resulted in partial reduction of the cluster by CO while it retains some oxygen [50]. So, the cluster will be predominantly metallic.

A kinetics study on Pt NPs supported by anatase revealed that the activation energy of CO oxidation suddenly changes after the temperature is raised up to a certain value, and this was attributed to the oxidation of Pt NPs at that temperature

and a different channel for CO oxidation [167], but the oxidation mechanism on oxidized particles was not clear. Considering the above discussion, we continue our investigation on metallic clusters only and skip further simulations for partially or fully oxidized clusters, since they are not stable phases in catalytic conditions.

5.4 CO oxidation on supported Pt_x clusters

As already mentioned, the oxidation of CO may proceed via Mars-Van Krevelen or Langmuir Hinshelwood mechanism. First, we discuss the Mars-Van Krevelen mechanism, in which oxygen atoms from the lattice incorporate in CO oxidation.

The key step in this mechanism is the activation of a lattice oxygen atom to interact with a CO molecule in the vicinity. The formation energy of oxygen vacancy (FE_{O_v}) and concentration of oxygen vacancies in the lattice has been considered to be correlated with the catalyst activity [63, 47]; lower FE_{O_v} results in higher activity. For instance, as was observed before [47] TiO_2 supported Pt_1 performed better in converting CO compared to Al_2O_3 supported Pt_1, and $FE(O_v)$ is lower on a reducible surface like TiO_2 rather than irreducible Al_2O_3.

For Pt_6, Pt_4 and Pt_1 systems covered by CO and supported on TiO_2 and Co_3O_4, we computed the $FE(O_v)$ at the cluster-support interface and around the clusters. The presence of the metallic cluster eases the creation of O_v on TiO_2 only in the proximity of the cluster. Table 6 summarizes the lowest FE_{O_v} computed on pristine surface and surface with adsorbed clusters/ adatom according to equation 5.0.2.

The minimum energetic cost of creating an O_v at the interfacial sites (between Pt_6 and TiO_2 surface) was 3.05 eV, less than the pristine brookite (3.9 eV). The latter value was found to

system	FE_{O_v} (eV)	system	FE_{O_v} (eV)
TiO_2 surface	3.9 ~5.2	Co_3O_4 surface	1.9 ~2.1
$Pt_6/TiO_2/6CO$	3.0 ~4.9	$Pt_6/Co_3O_4/6CO$	1.9 ~2.5
$Pt_4/TiO_2/4CO$	2.9 ~4.4	$Pt_4/Co_3O_4/4CO$	-
$Pt_1/TiO_2/1CO$	2.1 ~4.1	$Pt_1/Co_3O_4/1CO$	1.3

Table 6: FE_{O_v} calculated for pristine surface as well as different sizes of Pt clusters supported on TiO_2 and Co_3O_4.

be 2.9 and 2.08 eV for Pt_4/ TiO_2 and Pt_1/ TiO_2, respectively. This is an indication of the metallic particle-assisted formation of O_v. Theoretical and experimental studies show that adsorption of Pt clusters on Fe_3O_4 facilitates the formation of oxygen vacancy [161, 49]. Enhanced reducibility of the surface by the presence of metallic clusters was predicted in other studies as well [168, 169].

Creation of O_v on TiO_2 leads to localization of extra electrons on Ti^{+3}; the charge was mostly distributed between Ti atoms at the vicinity of O_v and a negligible amount of charge was transferred to the cluster. This is similar to what Chen, H.-Y. T et. al reported [170], after adsorption of the Ruthenium cluster on anatase, the charge was only partially transferred to the cluster. On the other hand, for Au NPs supported on TiO_2, the creation of oxygen vacancy resulted in charge transfer to the particles and stabilization of the vacancy [168].

We studied the MvK mechanism on Pt_6, Pt_4 and Pt_1 systems, supported on TiO_2 and Co_3O_4. We also considered another possibility which is substituting one of the atoms from supports with a single Pt. First, we discuss the CO oxidation reaction via MvK on Pt clusters, and in the next section, we explain the oxidation reaction simulation on atomic Pt.

Pt particle-assisted CO oxidation via the MvK mechanism can be divided into two cyclic halves:
1) Abstraction of one lattice oxygen, formation, and desorption

of the first CO_2. At the end of this half cycle, the catalyst is reduced and is left with an oxygen vacancy.
2) Filling the lattice vacancy with molecular oxygen from the environment, dissociation of O_2, formation of the second CO_2 with the extra oxygen atom, desorption of CO_2, and recreation of the initial state of the catalyst.

The energy profiles and full catalytic cycle of CO oxidation on Pt_6/TiO_2 and Pt_4/TiO_2 through the MvK mechanism are shown in Fig. 25. The same mechanism was also simulated on Pt_6/CO_3O_4 to see the role of support in CO oxidation; the corresponding energy profile is displayed in Figure 26. Elementary steps of the oxidation cycle are explained below:

CO adsorption: We considered the first step of CO oxidation to be the adsorption of CO on the system (Figure 25 and 26, $S_1 \longrightarrow S_2$). The adsorption of CO on Pt clusters is exothermic and non-activated, regardless of the type of support. Full CO coverage on Pt_6/TiO_2 causes a drastic deformation, and adsorption of 6CO weakens the cluster/support interaction. However, the structure of Pt_6/Co_3O_4 is less affected by the adsorption of CO (see Figure 26, S_2). In order to check the stability of this system at high temperatures (T), we employed ab initio molecular dynamics (AIMD) at T=400 K for almost 9960 femtoseconds. The results of AIMD simulation for Pt_6 supported on TiO_2 showed that at elevated T, the system becomes slightly mobile.

CO_2 formation: Next, the adsorbed CO molecule (which is close enough to the interface) diffuses to the interface to interact with the nearest lattice oxygen, remove it from the surface and form the first CO_2. Removal of lattice oxygen to form CO_2 is an activated step: this step is the most demanding step of the MvK mechanism on Pt_6/TiO_2 and Pt_4/TiO_2 by exhibiting activation energy (E_a) of 1.46 and 1.77 eV (Figure 25, S_3). Formation of

CO_2 from lattice oxygen is known as an activated step in metal/ reducible oxide heterogeneous catalysts [168, 164, 171, 13].

(a)

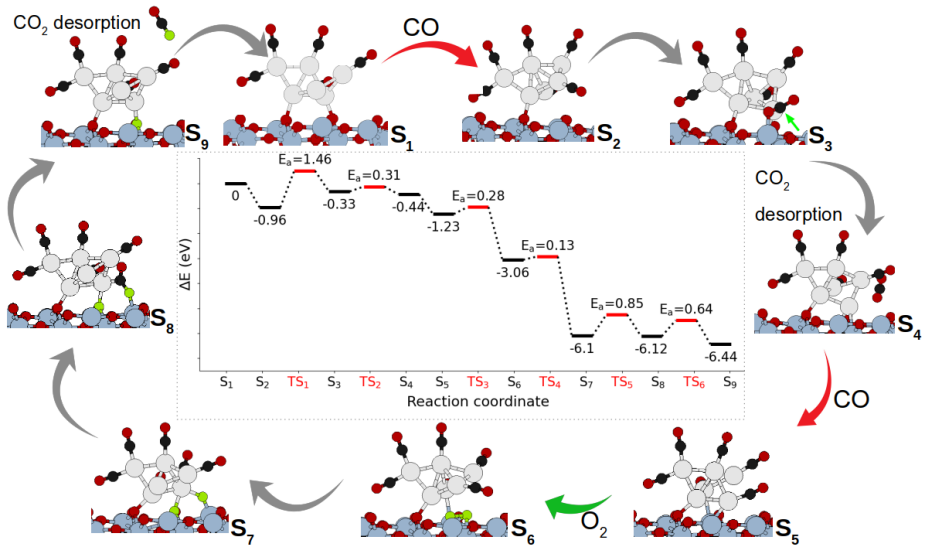

(b)

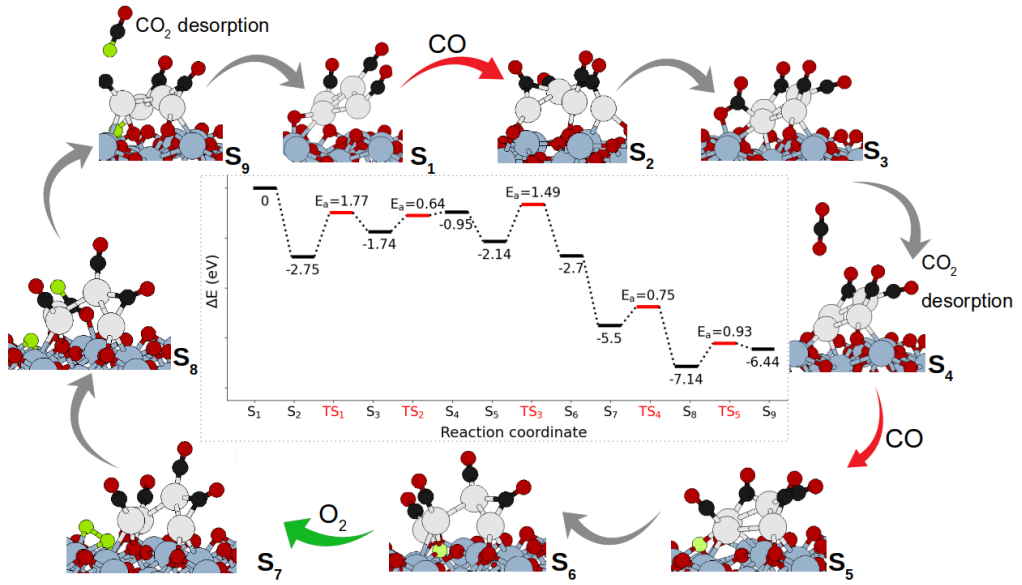

Figure 25: Energy diagrams for CO oxidation via MvK oxidation mechanism on a) TiO_2/Pt_6 and b) TiO_2/Pt_4 systems. Here, E_a is the energy barrier to go from S_i to S_{i+1} step.

On Pt_6/Co_3O_4, for the same step, the activation barrier was predicted to be 1.30 eV, which is slightly lower than the one on TiO_2. This was expected, since removing oxygen from the lattice is easier on Pt_6/Co_3O_4, see Table 6. Formation of CO_2 on Pt_4/TiO_2 requires an oxygen reverse spillover (the oxygen is taken from beneath the cluster). The values that we found on TiO_2 are comparable to the reported barrier of 1.13 eV on CeO_2/Pt_4 [63]. An experimental work on Au/TiO_2 is another evidence that showed as an activated step, removal of lattice oxygen by Au NPs occurs only at higher temperatures $\sim$ 120 °C, and at lower temperatures formation of CO_2 was not observed [13].

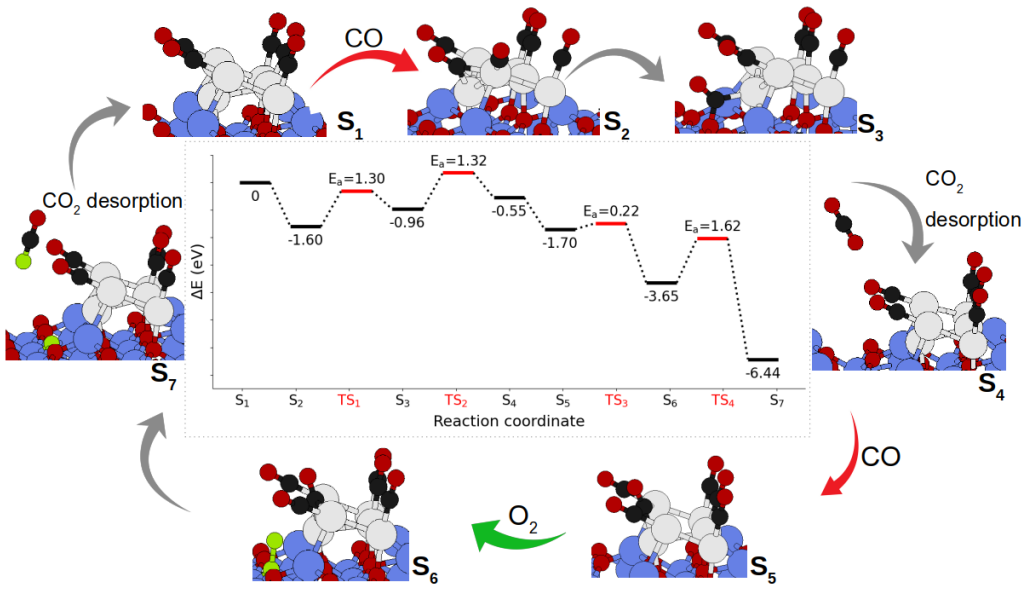

Figure 26: Energy profile of MvK mechanism for CO oxidation on Pt_6 cluster supported on Co_3O_4.

CO_2 desorption: the Last step of the first half-cycle of CO oxidation is CO_2 desorption from the system through an activated step. This step implies overcoming a barrier of 0.31 and 0.64 eV for clusters supported on TiO_2 (See Figure 25, S_4). Energetically, desorption of CO_2 is slightly exothermic on Pt_6/TiO_2,

but it costs almost 0.5 eV on Pt_4/TiO_2 and Pt_6/Co_3O_4. These predictions are made at T=0; at finite temperatures, however, the entropic effect would increase which in turn leads to a more negative chemical potential. This effect enters equation 2.3.6 and increases the Gibbs free energy of the system with adsorbed CO_2. Hence, Δ G of the CO_2 desorption would increase and this process would be thermodynamically more favorable. Desorption of the first CO_2 from Pt_6/Co_3O_4 (Figure 26, S_4) shows higher activation energy (E_a = 1.32 eV). In spite of what is reported in another computational work [63], that first half of the cycle on $Pt_4/TiO_2(101)$ was found to be endothermic by 0.27 eV, we found it to be exothermic on all the clusters in present work.

Abstracting one oxygen from lattice leaves behind a vacancy, and hence the cluster undergoes a notable structural deformation and becomes attracted to the vacancy to compensate for the absence of oxygen.

O_2 adsorption and dissociation: To close the catalytic cycle and regenerate the catalyst, the surface was re-oxidized by gas-phase molecular oxygen. On Pt_4/TiO_2, since the vacancy is located under the cluster and it is not accessible, we tried an alternative path and replenished the vacancy with adjacent oxygen from the lattice, and then filled the latter with gas-phase oxygen. Migration of the nearest lattice oxygen to fill the oxygen vacancy possesses a barrier of 1.49 eV (Figure 25.b, $S_5 \longrightarrow S_6$). The new vacancy adjacent to the cluster is now exposed to molecular oxygen from the environment.

Adsorption of O_2 nearby the vacancy is non-activated and quite exothermic by at least 1 eV on clusters supported on TiO_2; however a small activation barrier was predicted on Pt_6/Co_3O_4, i.e. E_a = 0.22 eV (see Figure 26, $S_5 \longrightarrow S_6$).

A possible path for filling the oxygen vacancy could follow these steps: 1) adsorption of molecular oxygen, 2) dissociation

of molecular oxygen, 3) filling the vacancy. Except for Pt_6/TiO_2 on which dissociation of O_2 had a negligible barrier of 0.13 eV (Figure 25. S_7), step 2 was not found as an intermediate on Pt_4/TiO_2 and Pt_6/Co_3O_4. This step was predicted to be highly exothermic on Pt_6/TiO_2 by releasing 3 eV energy. The existence of an O_v assists O_2 dissociation by electronically enriching O_2 and elongating O-O bond to 1.42 Å(O-O bond length in gas-phase is 1.23 Å). This is in line with another DFT study of Pt particles on mesoporous TiO_2, on which O-O bond length was increased to 1.48 Å after adsorption of O_2 [66].

A relatively higher barrier (0.41 eV) was predicted for O_2 dissociation on $Pd/CeO_2(100)$ which was comparable to the formation of CO_2 (0.5 eV) on the same system [171].

On Fe_2O_3 supported Pt NPs, O_2 dissociation turned out to be the rate-determining step of CO oxidation through the MvK mechanism [150].

In an experimental work on Au/TiO_2 system, the reduced system was re-oxidized by O_2 pulses at different temperatures (-20 to +240 °C); it was observed that O_2 consumption did not change remarkably as the temperature increased [168]. DFT calculations on the same system revealed that filling the vacancies is barrierless because of the coexistence of adjacent vacancies in the lattice, and in the case of a single oxygen vacancy this step is activated by a small barrier of 0.16 eV.

Formation and desorption of second CO_2: After adsorption and dissociation of molecular O_2, the first atomic oxygen recreates the stoichiometric surface, the second oxygen is adsorbed on the surface as an adatom, oxidizing the catalyst. The second oxygen may react with an adsorbed CO molecule or a second O_v. Furthermore, we also considered the possibility of the formation of the second oxygen vacancy around Pt_6/TiO_2. The minimum cost to remove the second oxygen around the cluster is about 3 eV, which makes it thermodynamically unfa-

vorable. Hence, we skip investigating multiple oxygen vacancies and consider the possibility that the remained atomic oxygen is not consumed to fill another vacancy, but to react with a second CO from another CO_2.

Formation of the second CO_2 with chemisorbed atomic oxygen on Pt_6/TiO_2 was predicted to have an energy barrier close to Pt_4/TiO_2: 0.87 and 0.75 eV, respectively (see Figure 25, S_8).

The last step which is desorption of the CO_2 molecule has a barrier lower than 1 eV on clusters supported on TiO_2, S_9, and then the catalytic cycle is closed by adsorbing a CO molecule.

Formation and desorption of the second CO_2 occur in one step on Pt_6/Co_3O_4; this step (Figure 26, $S_6 \longrightarrow S_7$) is associated with the highest energy barrier on Pt_6/Co_3O_4 (1.62 eV).

5.5 CO oxidation on supported single Pt

In the case of a single Pt atom catalyst, we examined two structures: 1) a single Pt adsorbed on the surface (Pt_1- adatom) and 2) a metal atom of the lattice was substituted by single-atom Pt. This means substituting a Ti from TiO_2 and Co from Co_3O_4 slab with Pt. On TiO_2, Pt will be coordinated with five and six oxygen atoms from the lattice (referred to as Pt_1(5c), Pt_1(6c)). On Co_3O_4, there are two types of cobalt atoms: Co^{+2} and Co^{+3}, and substituting Pt with these cobalt atoms results in three coordinated (Pt_1(3c)) and six coordinated (Pt_1(6c)) Pt atoms. This selection is based on the phase diagram in Figure 27 which is computed using ab initio thermodynamics. Different possibilities regarding the substitution of Pt_1 on brookite and Co_3O_4 were considered, including substitution with Ti (Co), O, and Ti (Co) in presence of oxygen vacancy.

In Figure 27, all the free energy values were compared to the energy of Pt_1- adatom, which is the horizontal axis of the plot. Within the range of interest of chemical potential, Pt_1 substi-

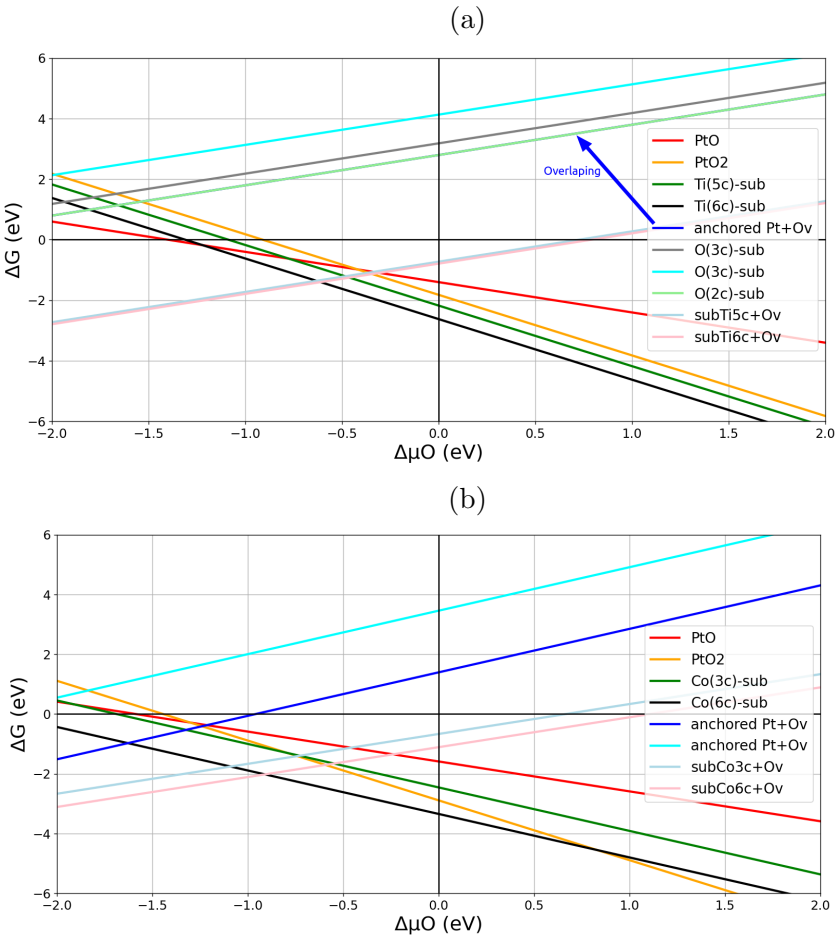

Figure 27: Gibbs free energy of different models as a function of oxygen chemical potential. Pt_1 was adsorbed/ substituted at different sites in presence or absence of oxygen vacancy (O_v) on the surface of a) brookite TiO_2 and b) Co_3O_4 .

tuting by 5 and 6- coordinated Ti atoms are stable phases. On rutile (110) nanowires, the favorable configuration for Pt was substituting a five-fold coordinated Ti atom [56]. This is similar to what was reported in another DFT simulation on CeO_2 which atomic Pt preferred to substitute Ce atoms [172]. We also simulate the reaction on Pt_1-adatom, since experimentally it is a possible and common phase.

First, we discuss the oxidation reaction over Pt_1- adatom,

Pt_1(5c), and Pt_1(3c). CO oxidation on Pt_1(6c) will be discussed later.

Fig. 28 depicts the configurations and potential energy diagram of the oxidation reaction of CO on Pt_1- adatom. Adsorption of Pt_1- adatom on TiO_2 pushes one of the bridge lattice oxygen atoms upward, as shown in Figure 28.a, S_1. After adsorption of CO, his oxygen is the easiest one around the Pt-adatom to remove, with $FE_{O_v} \sim 0.9$ eV. We checked the possibility of creating another oxygen vacancy on the reduced system; removing the second oxygen was endothermic by 2.6 eV, and since the activation barrier of CO_2 formation would be $\geq$ 2.6 eV, hence we skipped simulating this path.

Formation of first CO_2 (S_3) is slightly exothermic on TiO_2 with a barrier of only 0.6 eV, while on Co_3O_4 is more endothermic ($\sim$ 1eV). Sequential desorption of CO_2 (S_4) requires the highest E_a in the catalytic cycle on both types of supports: 1.09 eV on TiO_2 and 1.67 eV on Co_3O_4. Formation and desorption of the second CO_2 occur spontaneously on TiO_2 (28.a, $S_6 \longrightarrow S_7$); however on Co_3O_4 in addition of these steps which take place sequentially, an extra step involving the dissociation of O_2 and filling the vacancy ($E_a = 0.89$ eV). In the second half of the cycle on Co_3O_4, the formation of CO_2 drops the energy of the system to $\sim$ -7 eV, showing that at DFT condition this intermediate is highly stable (S_8). This is similar to what happens on Pt_4/TiO_2 (S_8), but desorption of this CO_2 is not the most demanding step of the reaction on either of these systems.

The rate-determining step for CO oxidation by the MvK mechanism on Pt clusters supported on TiO_2 was found to be CO_2 formation. However, the bottleneck of oxidation reaction on Co_3O_4 supported cluster as well as Pt_1- adatom is desorption of CO_2. In the case of a single-atom catalyst, the reaction proceeds slower on Co_3O_4 rather than TiO_2. We assume there is a single rate-determining step and the only parameter con-

trolling the kinetics is the height of the largest barrier; on TiO_2 this barrier is 1.46 eV, on Co_3O_4 this barrier is 1.62 eV. Hence on this basis, one could predict CO oxidation to be slower on Co_3O_4 compared to TiO_2.

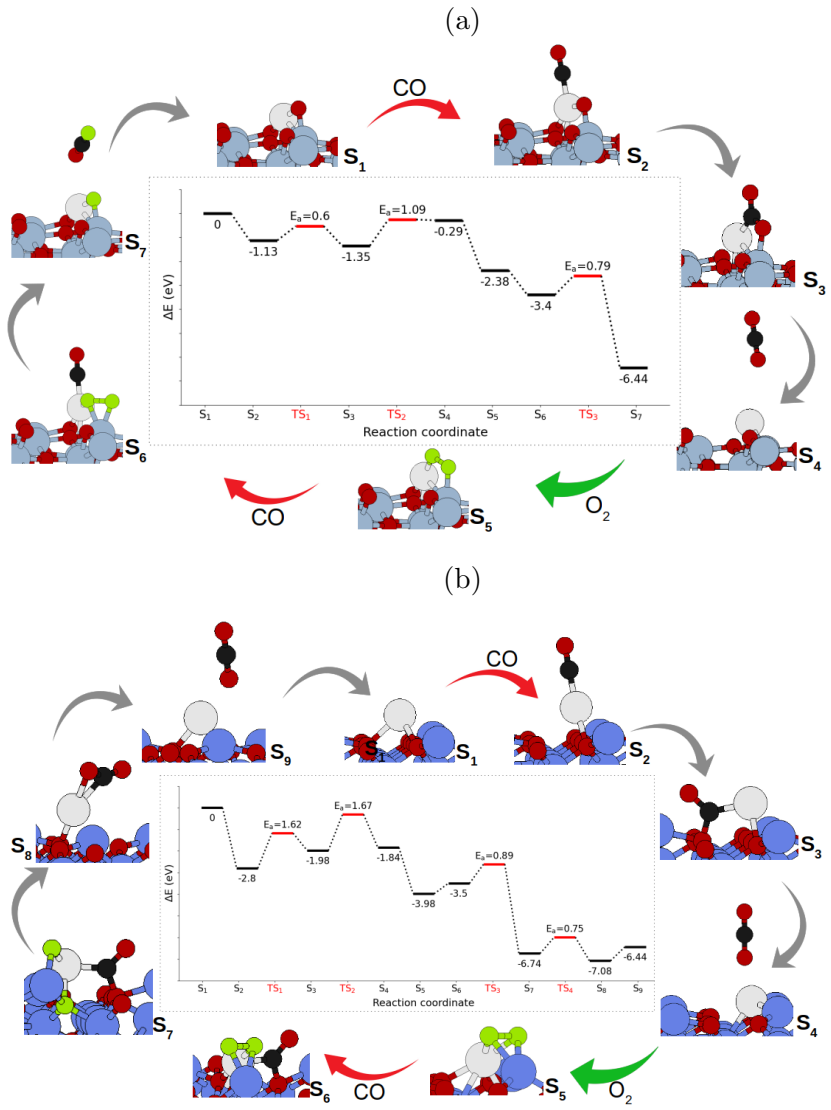

Figure 28: Catalytic cycle and energy diagram of CO oxidation on a) Pt_1-adatom/TiO_2 and b)Pt_1- adatom/Co_3O_4 systems.

In spite of the reasonable barrier, we predicted for the first step of the MvK on Pt_1/brookite, Selin Bac and others [173] re-

ported a substantial energy barrier for CO_2 formation on Pt_1/rutile: 3.12 and 2.18 eV, depending on CO or O_2 migrating towards the other species. Further, they closed the cycle by co-adsorbing two CO molecules on the reduced system, so the formation of the second CO_2 took place with the assistance of another CO. But CO- assisted MvK resulted in even higher energy barriers for CO_2 formation and desorption ($\geq$ 3eV).

On $Pt_1(5c)/TiO_2$, similar to the MvK mechanism on TiO_2 supported Pt clusters, the most demanding step was predicted to be forming CO_2 with lattice oxygen. However, E_a of this step does not exceed $\sim$ 1 eV which is close to the highest E_a on Pt_1-adatom, see 29.a, $S_2 \longrightarrow S_3$. Moreover, same as Pt_1-adatom, formation, and desorption of the second CO_2 is simultaneous on $Pt_1(5c)/TiO_2$ with an E_a of 0.68 eV which is comparable with E_a of the same step on Pt- adatom (0.79 eV). Although the rate-determining step is not the same on Pt- adatom, and $Pt_1(5c)$, the highest energy barriers on these two systems are almost identical, 1.09 and 0.99 eV respectively. Substituting a 3-fold Co with Pt leads to a reaction path (see Figure 29, b) which displays the lowest activation barrier relative to Pt cluster and Pt adatom on Co_3O_4. In this case, it is possible to co-adsorb two CO molecules on a Pt atom, and this structure is slightly more favorable than adsorbing one CO. First CO reacts with lattice oxygen, and formation and desorption of CO_2 have almost the same energy barrier (0.6 $\sim$ 0.69 eV). Here, the other CO molecule acts as a spectator and does not interact directly in the oxidation reaction. Hence, the next step (S_5) is adsorbing another CO and then molecular oxygen to fill the lattice vacancy. Adsorption of oxygen is an activated step with 0.36 eV activation energy. While the formation of the second CO_2 has the highest barrier in the cycle (0.77 eV), removing it is not activated and is highly exothermic.

The energy barrier to form and desorb CO_2 on $Pt_1/CeO_2(110)$

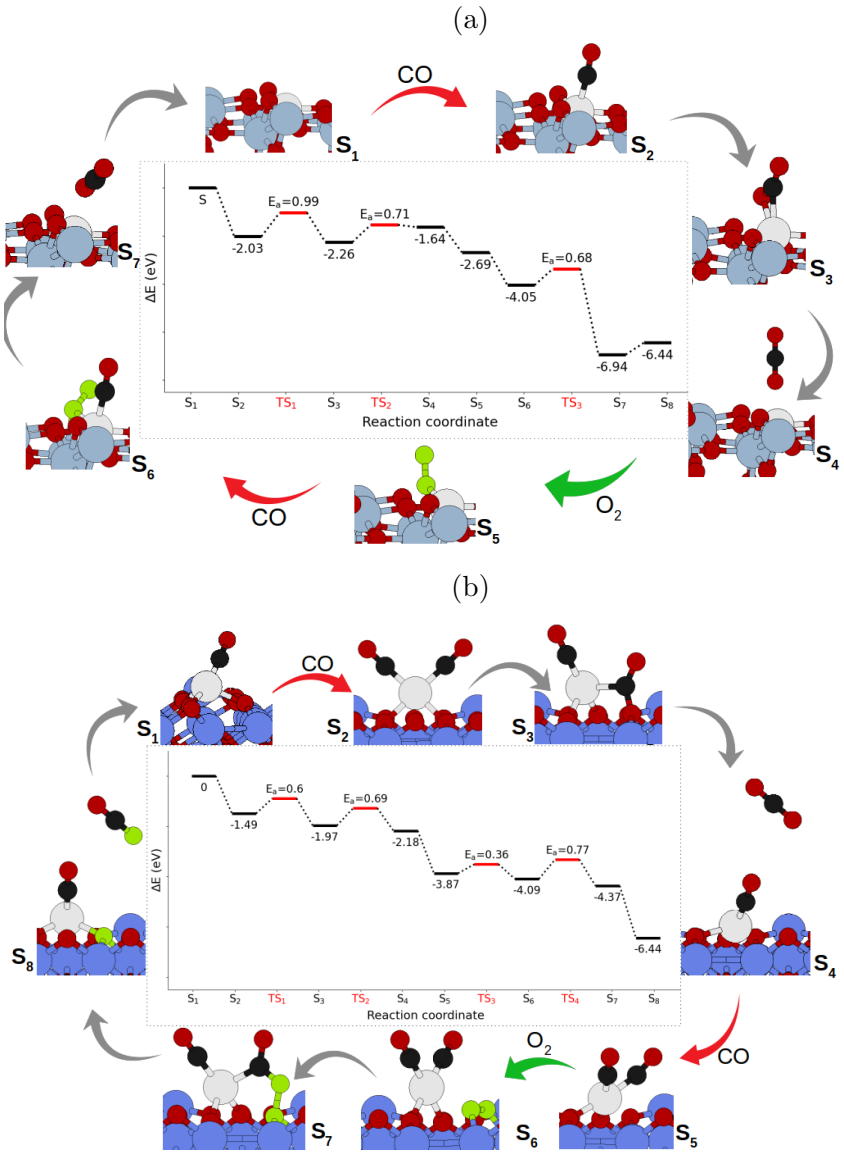

Figure 29: Catalytic cycle and energy diagram of CO oxidation on a) $Pt_1(5c)/TiO_2$ and b)$Pt_1(3c)/CoO_4$ systems.

was predicted to be 1.31 eV if the oxidation reaction goes through MvK mechanism [174]. On the same support but exposing (111) termination, the predicted activation energy was even higher (2.38 eV) [175].

By replacing a fully coordinated metallic atom of the surface

with a single Pt, CO (g) reacts dissociatively with oxygen from the system and forms CO_2 (g).

This mechanism takes similar steps over Pt_1(6c) on titanium and cobalt oxide. CO (g) approaches the oxygen atom which is bonded on top of Pt_1(6c). To remove this oxygen, 1.83 eV energy is required on TiO_2. On Co_3O_4 however, $E_{form_{O_v}}$ associated with this oxygen is 2.22 eV, which is more than $E_{form_{O_v}}$ on pristine Co_3O_4. A recent study on the interaction between Pt atom and rutile (110) revealed that substituting a 6- coordinated Ti with Pt makes the formation of oxygen vacancy easier and stabilizes the oxygen vacancy against migration [176]. In the case of Pt_1 on CeO_2, removal of lattice oxygen was 1 eV more endothermic in presence of a single Pt- adatom compared to bare CeO_2. However, doping CeO_2 with atomic Pt made it easy to remove the oxygen at the vicinity of Pt [174].

Local optimization of the catalyst with a CO molecule adsorbed on lattice oxygen (*CO) leads to simultaneous formation and desorption of CO_2. Adsorption, formation, and desorption of CO_2(g) happen in one step on both supports, with the formation of $^*CO_2$ being the transition state. The activation energy corresponding to this step is higher on Co_3O_4 (0.70 eV) than on TiO_2 (0.48 eV). Sequential adsorption of O_2 and filling the vacancy is non-activated and reduces the energy of both systems to lower than -2 eV. After filling the oxygen vacancy, one atomic oxygen is chemisorbed on the surface which readily reacts with another CO (g) to form and leave the system as CO_2. Formation and desorption of the second CO_2 are associated with moderate energy barriers on both supports: 0.38 and 0.32 eV on TiO_2 and Co_3O_4, respectively.

The reaction paths of CO oxidation assisted by Pt-substituted on both oxides are depicted in Figure 30

As one can see, the catalytic performance of Pt_1 is different on two different types of supports in this work. An experimen-

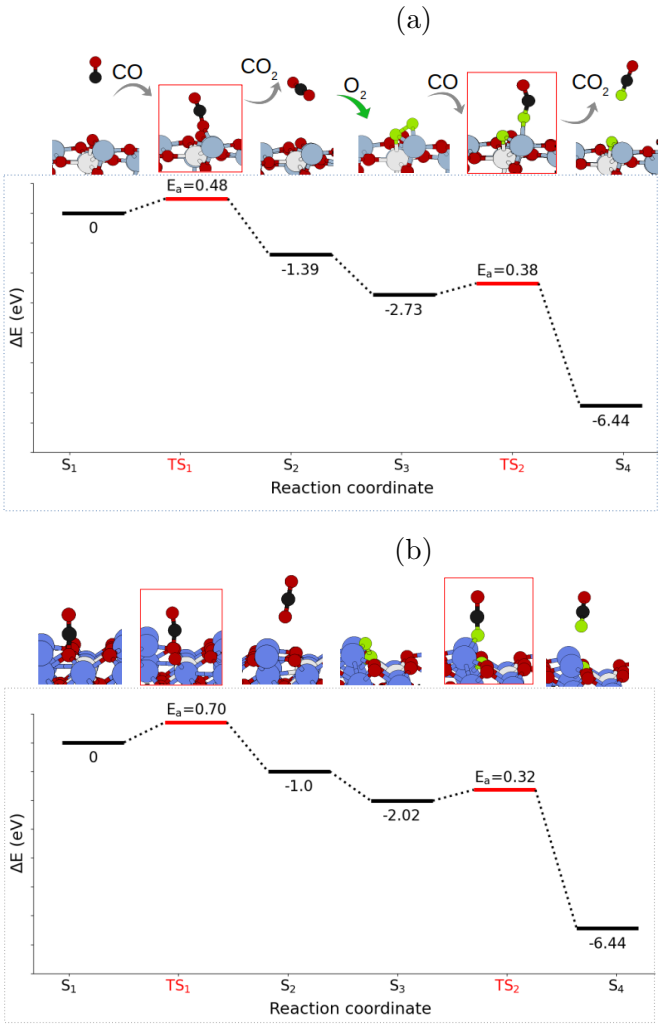

Figure 30: CO oxidation on oxides doped with Pt_1(6c) on a) TiO_2 and b) Co_3O_4.

tal study on Pt_1 adsorbed on surfaces with different reducibility supports our findings: SACs were synthesized on highly reducible Fe_2O_3, reducible ZnO, and irreducible Al_2O_3. It was found that the reaction rate on a single Pt relates to the reducibility of the supporting surface [177].

In a theoretical work on Pt_1/CeO_2, the stable structure was found to be Pt substituting a 6- coordinated Ce atom. In this simulation, two CO molecules form CO_2 with lattice oxygen

atoms sequentially, and then two vacancies are filled via dissociative adsorption of one molecular oxygen which is the rate-determining step of the cycle [172].

In an experimental investigation on Pt_1/rutile with Pt substituting a Ti atom, the highest barrier associated with CO conversion was found to be 22.7 KJ/mol^{-1} ($\sim$ 0.2 eV), which was in line with the computed barrier from DFT simulation of the same system (19 KJ/mol^{-1}) [56]; these results are numerically comparable with our findings. In general, reverse spillover of lattice oxygen to interfacial sites of the heterogeneous catalysts was found to be the rate-limiting step of the oxidation reaction rather than O_2 dissociation [12].

The role of cluster size, as well as type of support, was investigated for CO oxidation via the MvK mechanism on Pt catalysts. If Pt clusters are oxidized before the catalytic reaction, they would be mostly reduced upon exposure to CO. As for the MvK mechanism, removing the lattice oxygen by CO to form CO_2 was found to be a common rate-determining step of CO oxidation on supported Pt clusters, whereas desorption of CO_2 product was the demanding step on single-atom Pt catalysts. The activation barriers will drop in case of substituting a metallic lattice atom with atomic Pt, especially for highly coordinated lattice atoms.

6 CO oxidation via Langmuir Hinshelwood

The present chapter investigates the oxidation of CO on Pt clusters via LH oxidation mechanism, in which both reactants chemisorb on the catalyst before reacting. The Kinetics of CO oxidation is discussed on Pt clusters as well as single-atom Pt catalysts.

6.1 CO oxidation on supported Pt_x clusters

The second oxidation mechanism that we considered for the CO oxidation on Pt catalysts is the Langmuir Hinshelwood (LH). In analogy to section 5, oxidation reaction was modeled on Pt_6 and Pt_4 clusters supported on TiO_2 as well as Pt_6 supported on Co_3O_4. LH mechanism was also investigated over single Pt catalysts as adatom and substituted. Unlike the MvK mechanism, with the conventional LH scheme, the role of lattice oxygen in oxidation is excluded, and the CO oxidation reaction takes place via the coadsorption of CO and O_2.

CO oxidation on Pt clusters on TiO_2 and Co_3O_4 via LH mechanism takes place as displayed in Figure 31 and 32 according to following steps:

CO adsorption on Pt cluster: First step of the cycle is the non-activated adsorption of the last CO on Pt clusters, so the clusters are fully (1 CO per Pt) covered by CO.

O_2 adsorption: We tried to find an adsorption site on the clusters, but since they are already fully covered by CO, adsorption of gas-phase O_2 was not possible. Therefore, we probed the interfacial sites and perimeter of the clusters and interfacial sites between the surface and clusters, and interfacial sites were found to be favorable sites for adsorption of O_2. There is experimental evidence that confirms the reactivity of interfacial sites between

Pt particles and surface [166, 60]. Similar to CO adsorption, adsorption of O_2 is energetically favorable and non-activated (step S_3 in Figure 31.a and b and Figure 32).

O_2 dissociation: On TiO_2 supported clusters, dissociation of O_2 is an activated step, and is associated with an energy barrier of 1.35 eV on Pt_6 and 0.66 eV on Pt_4 (Figure 31.a and b, S_4). Dissociation of O_2 on Pt_6 exhibits the highest energy barrier in the cycle. However, this step did not appear as an intermediate on Pt_6/Co_3O_4.

Formation of CO_2: After dissociation of O_2, a CO molecule diffuses towards the atomic oxygen to form CO_2 (S_5 in Figure 31, S_4 in Figure 32). This step is activated by 0.9 and 0.67 eV on Pt_6 and Pt_4, respectively. Although CO_2 formation is exothermic on TiO_2, this step is endothermic on Co_3O_4, which can be attributed to the simultaneous dissociation of O_2 prior to CO_2 formation. Moreover, E_a of this step on Co_3O_4 is 0.82 eV, as the highest energy barrier of the whole cycle on Pt_6/Co_3O_4.

Desorption of CO_2: Formed CO_2 from the previous step is still adsorbed to the system. To remove this product from the catalyst, one should overcome a similar, small barrier (< 0.2 eV) on both types of supports (step S_6 on TiO_2, S_5 on Co_3O_4). This step leaves behind the catalyst with atomic oxygen which is still chemisorbed in the system.

CO adsorption: Since adsorption of CO is very favorable and non-activated as well, the catalyst would gain another CO from the ambient. This step is substantially exothermic on all systems by releasing at least 2 eV energy.

Formation of second CO_2: Next step on all Pt systems is formation of another CO_2 with retained atomic oxygen on the cluster (step S_8 on TiO_2, S_7 on Co_3O_4). While the formation of the second CO_2 has a moderate E_a on Pt_6/Co_3O_4, E_a on Pt_6/TiO_2 was found to be 1.16 eV; a remarkable E_a of 1.72 eV was predicted on Pt_4/TiO_2 as well. The huge activation

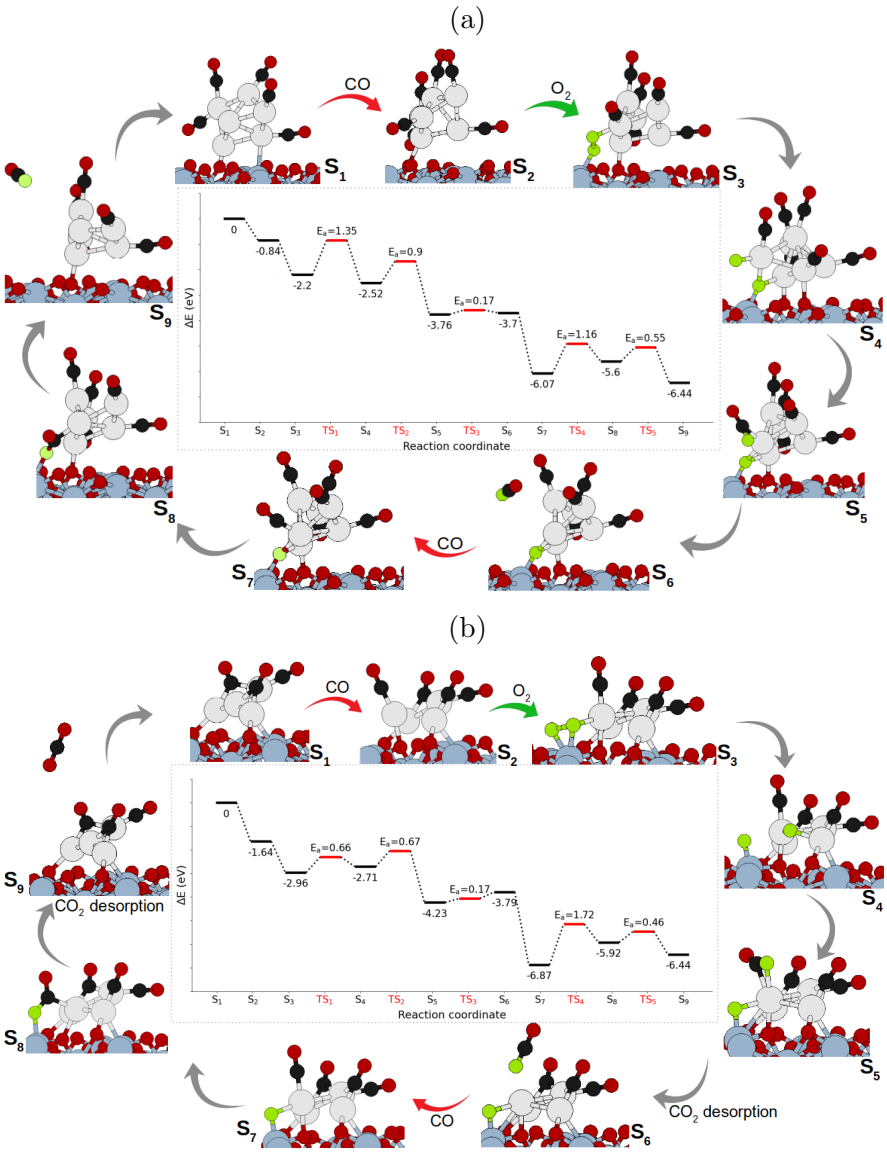

Figure 31: Steps of CO oxidation over a) Pt_6 and b) Pt_4 supported on TiO_2 via LH mechanism.

energy regarding desorption of CO_2 makes this step the most demanding step of CO oxidation on Pt_4/TiO_2.

Desorption of second CO_2: Desorption of second CO_2 is just slightly more difficult than first CO_2 on Co_3O_4. On TiO_2 however, the removal of the second CO_2 is more demanding than

the first CO_2 ($\sim$ 0.5 eV compared to 0.2 eV). This last step closes the cycle and recreates the catalyst.

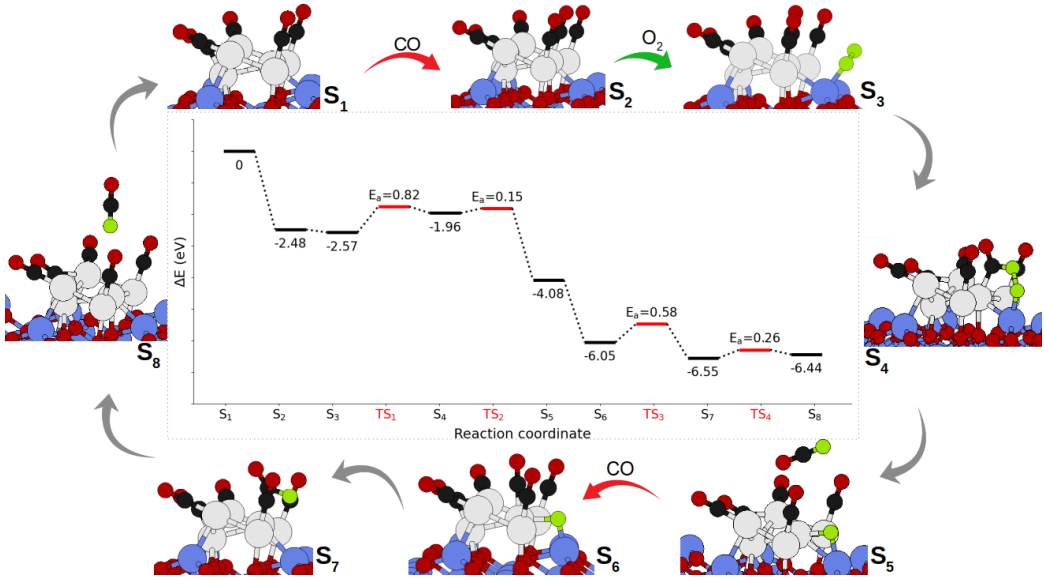

Figure 32: CO oxidation through LH mechanism over Pt_6/Co_3O_4.

6.2 CO oxidation on supported single Pt

In addition to Pt clusters, we examined CO oxidation over a single Pt-adatom on both surfaces. We also checked the possibility of CO oxidation on Pt_1-5c via LH; we found out that the first part of the cycle is highly endothermic. Since E_a of an elementary step is equal to or more than the ΔE of the elementary step, therefore oxidation would be kinetically unfavorable.

The possible oxidation path and energy profile of the reaction on Pt_1 on both supports are displayed in Figure 33. The initial step of the catalytic cycle is the adsorption of CO ($S_1 \longrightarrow S_2$) which is more exothermic on Co_3O_4 by more than 1 eV. For an oxidation reaction going through the LH channel, the next step would be the adsorption of O_2 from the environment (S_3). The order of adsorption for O_2 and CO was reported to be ineffective

on the turnover frequency of the reaction [173]. Similar to what we found on Pt clusters, the adsorption of molecular oxygen on a single Pt is also non-activated or has a negligible activation barrier. On TiO_2, Pt adhesion to the surface is more perturbed by the adsorption of O_2 at the interface. Adsorption of O_2 adjacent to Pt-adatom leads to the up-moving of Pt where Pt is only bonded to one oxygen from the lattice and increasing bond length of O-O to 1.41 Å.

Dissociation of O_2 was not found as an activated intermediate on Pt_1/both types of supports. The first activated step of LH on Pt_1 is spontaneous dissociation of O_2 and succeeding formation of CO_2 from coadsorbed species. This step (S_4) is exothermic on TiO_2 and endothermic on Co_3O_4. But, compared to the moderate value of E_a on TiO_2 (0.86 eV), E_a of 1.98 eV is remarkably high on Co_3O_4. For the same reaction step on rutile, E_a was reported to be close to what we found on brookite [173]. The previous step is followed by the removal of the first CO_2, which releases more than 1 eV energy on Co_3O_4 by overcoming a small energy barrier ($\sim$ 0.3 eV); it faces no energy barrier on TiO_2 but is slightly uphill in free energy.

Adsorbing another CO on the catalyst is highly favorable, especially for Co_3O_4 on which the free energy of the system drops to less than -7 eV. As a result, the formation of the second CO_2 requires overcoming a much higher E_a of $\sim$ 1.4 eV on Co_3O_4, whereas the same reaction step has an energy barrier of 0.67 eV on TiO_2. However, to remove the second CO_2 and close the cycle, a substantial barrier of 1.34 eV should be overcome on TiO_2, almost twice the E_a of 0.67 eV on Co_3O_4. The bottleneck of the second half of the cycle was found to be the formation of CO_2 on rutile, with an associated energy barrier of 1.58 eV [173].

Considering our simulations on Pt_1 adsorbed on TiO_2 and Co_3O_4, one can see that the highest energy barrier on TiO_2

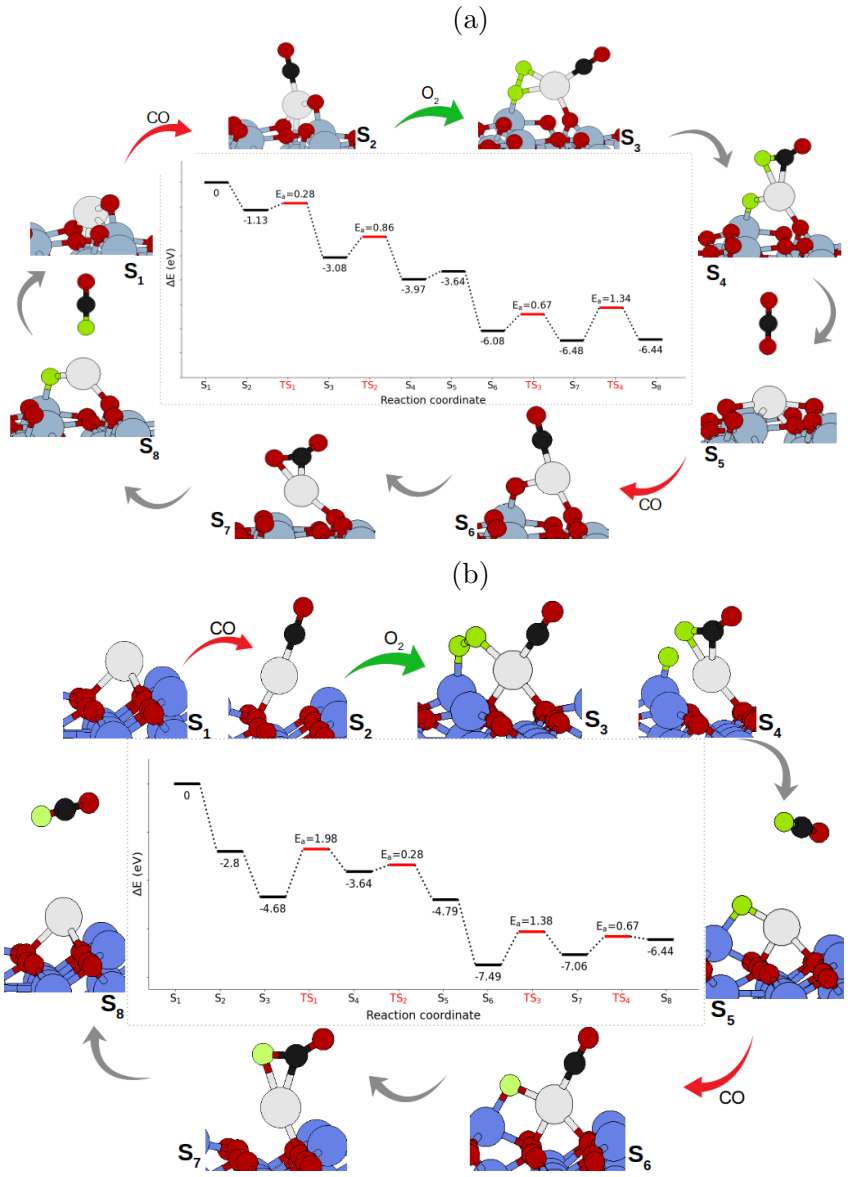

Figure 33: LH mechanism for CO oxidation on Pt- adatom supported on the surface of a) TiO_2 and b) Co_3O_4.

is almost 1.3 eV corresponding to the removal of the second CO_2; whereas on Co_3O_4 breaking O-O bond and forming CO_2 is kinetically hindered by a high activation energy of $\sim$ 2 eV. As a result, if oxidation of CO goes through the LH channel, most probably Pt_1/Co_3O_4 will perform much slower.

A non-MvK oxidation path was reported on Pt_1 supported on irreducible Al_2O_3 [178, 158]; but according to the results found in the present work, MvK is predicted to be an easier reaction channel than LH on Pt_1 if supported on reducible brookite. Another ab initio study on irreducible θ -Al_2O_3 (010), predicted a derivation of LH for CO oxidation on Pt_1: Adsorption of O_2 was more favorable than CO, and hence adsorption of CO on oxidized Pt_1 led to the formation of carbonate (-CO_3). Removal of formed carbonate is highly endothermic, and unless the reaction is run at high temperature, the catalyst would be covered by CO_2 [179]. This indicates the crucial role of the type of supporting surface in the CO oxidation mechanism. Another DFT work on reducible Pt_1/CeO_2 (110) is in agreement with our findings: although the highest activation energy was predicted to be 1.31 eV for the MvK mechanism, it increased to 2.15 eV if the reaction proceed via LH mechanism [174].

Comparing the intrinsic activation barriers of LH mechanism on Pt systems with different sizes, we notice that on TiO_2, Pt_6 and Pt_1 would perform similarly. However, Pt_4 shows a higher E_a than Pt_6 via the LH mechanism. In agreement with our findings, Pt_1/FeO_x had a higher rate and TOF for CO oxidation via LH mechanism than Pt clusters and Pt NPs [53].

On the other hand, CO oxidation on Pt_x/Co_3O_4 occurs on Pt_6 cluster with a mild value of activation energy, whereas Pt_1 does not sound to be an efficient catalyst for CO oxidation. This is vividly another evidence that the catalytic behavior of Pt systems is dictated by the type of support and the number of Pt atoms encompassed in the catalyst.

7 Discussion, conclusions, and outlook

7.1 Discussion

The present work is a thorough investigation of the catalytic performance of supported Pt systems on metal oxides. It was found that the catalytic behavior of Pt systems is governed by cluster size, type of support, and oxidation state of the cluster.

Our simulations show that on Pt catalysts supported on reducible surfaces such as TiO_2 and Co_3O_4, conversion of CO into CO_2 can involve oxygen atoms from the lattice. Adsorption of metallic particles induces/ promotes the catalytic activity on the metal oxide surface. Our findings are another proof of the pivotal role of metallic clusters in CO oxidation on metal oxide supports. CO_2 production on TiO_2 and Fe_3O_4 was not observed prior to adsorption of a metallic particle like Pt and Au [180, 161, 168, 66, 161].

Further, our investigation implicitly reveals the significant role of reducible supports in CO conversion reaction. We found MvK and LH oxidation mechanisms to be thermodynamically and kinetically possible on Pt catalysts supported on reducible brookite TiO_2 and Co_3O_4. For the MvK oxidation mechanism, Pt catalysts supported on TiO_2, both Pt_6 and Pt_1 adatom were found to be more active catalysts than Pt_4. In the case of the MvK, Pt catalysts supported by Co_3O_4 have lower activation energy only if a single atom Pt substitutes one 3-coordinated Co atom from the lattice.

For the LH mechanism, while Pt_6 is more active on Co_3O_4, Pt_1 adatom/Co_3O_4 shows a high barrier for CO oxidation.

Moreover, if the oxidation reaction is assisted by Pt clusters on TiO_2, the activation barriers are quite similar for MvK and LH. This does not apply to single Pt on TiO_2 or Pt catalysts supported on Co_3O_4.

In the case of irreducible surfaces such as Al_2O_3 which act as a spectator during CO oxidation, MvK was not detected as a possible mechanism [178]. Oxidation of CO into CO_2 was experimentally observed via both LH and MvK mechanisms on TiO_2 supported Pt clusters, but CO_2 production via MvK demanded higher temperature. Moreover, CO and O_2 molecules were isotopically labeled, and it was found that only 20 % of produced CO_2 was a result of the lattice oxygen incorporation and the rest of produced CO_2 was the outcome of LH mechanism [60].

We found that for Pt clusters, the activation of the lattice oxygen is the slowest step on TiO_2, but removing CO_2 is the demanding step on Co_3O_4. The latter was found to be the most demanding step also on Pt- adatom catalysts supported on both oxides. In this scenario (MvK mechanism), Pt clusters (Pt_6) are less efficient catalysts compared to Pt_1 (adsorbed as adatom or substituted) on TiO_2. Whereas on Co_3O_4, the energy barrier for oxidation of CO was found to be higher on Pt_1 adatom rather than Pt_6. This finding is supported by experimental investigation on Pt catalysts adsorbed on anatase which demonstrated that Pt_1 is at least 4 times more active than Pt clusters ($\sim$ 1 nm) in the oxidation of CO [50].

To obtain a better insight regarding the effect of cluster size on oxidation reaction, in addition to Pt_6, we also modeled CO oxidation on Pt_4/TiO_2. In this case, we found higher activation barriers on the smaller cluster, indicating a possible decay in the catalytic performance of the smaller Pt systems in subnano scale. By computing the change of the energy of the system for the initial steps of the oxidation reaction, we found that the energetics of the reaction is not favorable on Pt_4 supported on Co_3O_4. Hence, we skipped performing further simulations over Pt_4/Co_3O_4. An experimental comparison showed that while smaller Au particles (< 5 nm) supported on anatase exhibited remarkable performance in CO conversion, the catalytic

performance of Pt NPs deteriorated as their size decreased to less than one nanometer [9].

We checked the possibility of CO conversion on a pre-partially oxidized Pt cluster; most probably the partially oxidized cluster will be reduced and the clusters will be mostly metallic. However, it is possible that some oxygen atoms remain on the clusters since the barriers to activate these chemisorbed atomic oxygens are higher. In this scenario, we examined oxidation of CO through LH on a partially oxidized cluster and found it hardly possible due to unfavorable adsorption of O_2 (g) on such a system. It was experimentally observed that preoxidized Pt clusters were partially reduced when exposed to CO, yet showed much less reactivity regarding CO oxidation rather than metallic clusters; CO remained adsorbed on partially oxidized cluster until temperature raised to more than 160 °C.

Oxidation of CO over cobalt oxide-supported Pt particles has been rarely studied. Pt particles supported on mesoporous Co_3O_4 exhibited remarkable activity relative to other reducible oxides [46]. Hence, there is not much theoretical or experimental evidence for us to make a comparison. Our simulations and findings suggest that Pt clusters are possibly active catalysts when supported on Co_3O_4. In addition, in spite of many theoretical and experimental works supporting the idea of Pt_1 being a good catalyst, our findings predict that probably this is not the case on Co_3O_4. Single Pt catalyst was active only when substituting an atom from the lattice. This could be an initial idea for further investigations.

Further, we tried to complete our study by finding a descriptor in order to explain the different behaviors of Pt catalysts.

Experimentally, it has been proposed that cationic Pt atoms are active sites for CO oxidation [50]. An experimental work by Beniya et. al. [181] on Pt_n clusters, $7 \leq n \leq 35$, supported on non-reducible Al_2O_3 showed a reduced catalytic activity with a

decrease in the size of the clusters. They attributed this activity quenching to an increased number of cationic Pt atoms (CN $\leq$ 5) in smaller clusters. Undercoordinated Pt atoms in contact with the support had a partial positive charge, which decreased their tendency for oxygen. While they used a method based on bond energy to predict a low CO oxidation activity and oxygen affinity for Pt atoms at the perimeter of the cluster in contact with TiO_2, we found the interface of clusters and support to be favorable sites for adsorption and dissociation of O_2. In a more recent work [60], same authors reported a more detailed study on CO oxidation on rutile TiO_2 supported Pt clusters: they claimed a correlation between the number of edge Pt atoms with CN$\geq$6 and the number of produced CO_2 molecules through MvK mechanism; the number of these Pt atoms with maximum coordination number decreased with increase in cluster size. In the present work, however, considering the small size and 3D structure of Pt systems, and also the fluxionality of the clusters, we can not claim the same.

Another possibility is to find a linear correlation between activation energy and adsorption energy of reactants, known as the Brønsted–Evans–Polanyi relation [182]. Here we considered the change in free energy corresponding to dissociative adsorption of O_2 on Pt systems and the activation barrier of sequential dissociation of O_2. As depicted in Figure 34, there is no linear relation between activation energy and adsorption energy of molecular oxygen; also no size-dependent relation was found.

We only have three data points on TiO_2, and for Co_3O_4 two data points are insufficient to establish a trend, hence it was not possible for us to check this relation on Co_3O_4.

In general, the application of metallic single-atom and clusters in the conversion of CO into CO_2 has been studied for different metals on different supports [183]. The findings of the present work highlight the potential of Pt nanocatalysts for the

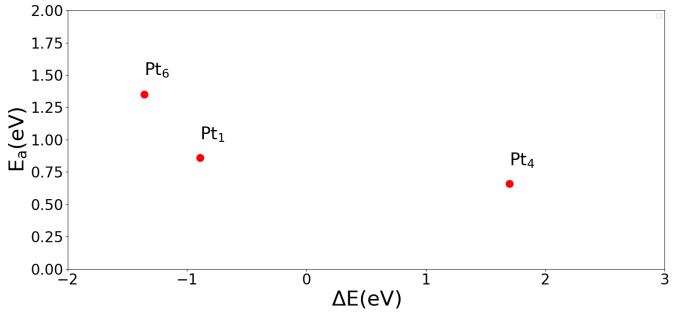

Figure 34: Calculated activation energies (E_a) and dissociative chemisorption energies (ΔE) of O_2 for Pt catalysts on TiO_2.

oxidation of CO(g), which is one of the gaseous products of exhaust emissions. This work presents a report regarding the catalytic performance of different sizes of Pt clusters, which could be of interest when synthesizing and tailoring nanocatalysts. Moreover, a comparative, detailed study of different configurations of single-atom catalysts was provided, which could be useful in explaining the experimental observations.

7.2 Conclusions and outlook

In this thesis, we performed a theoretical investigation within the framework of DFT on the oxidation and catalytic behavior of nanoscale Pt clusters supported on the surface of brookite $TiO_2(210)$ and $Co_3O_4(111)$.

To study the oxidation of Pt clusters, we interfaced a genetic algorithm with QE and found the possible global minima of metallic and oxide clusters in the gas-phase and on both surfaces. Then, using the definition of formation energy, we studied the oxidation of Pt clusters for different cluster sizes. We found that Pt nanoclusters show much more affinity for oxidation compared to bulk Pt. Also, smaller Pt clusters were found to be easier to oxidize than larger clusters. Gas-phase Pt clusters form the most stable oxides; however, adsorption on the supporting

surface hindered their oxidation to some extent. While oxidation of smaller clusters was easier on Co_3O_4 than TiO_2, for larger clusters the type of support had a negligible impact on the oxidation of clusters, especially in a highly oxidative environment. Ab initio thermodynamics calculations showed that higher pressure of oxygen and lower temperatures favor the oxidation of Pt clusters.

Bader charge analysis was used to study the interaction between the clusters and the surfaces. It was found that the amount of transferred charge from clusters to either of the surfaces in this work was very small. Thus, we did not find a remarkable charge transfer between metallic clusters and supporting oxides.

Next, we moved one step forward to study not only thermodynamics but also the kinetics of a reaction over Pt cluster catalysts. Oxidation of carbon monoxide was selected as the chemical reaction to be modeled on these catalysts. Adsorption sites of CO and O_2 on the catalysts as well as their relative coverage in reaction conditions were found. Then, the conversion of CO into CO_2 was examined over Pt clusters via the MvK and LH oxidation mechanism. It was predicted that on TiO_2 a larger cluster can perform better than a small cluster in the oxidation of CO. However, atomic Pt catalysts showed much higher activity on TiO_2 than Pt clusters. The opposite was predicted on Co_3O_4, meaning that a Pt cluster is a reasonable catalyst on Co_3O_4 but a single-atom Pt is not predicted to be efficient for CO oxidation. Only by doping the Co_3O_4 surface with single atom Pt, CO oxidation is possible with a lower activation barrier.

To have a more complete picture of the catalytic activity of Pt clusters supported on brookite, we plan to calculate the reaction rate of CO oxidation over Pt clusters.

A further step that one can consider is to study larger sub-

nano Pt_x clusters on this surface; since in this work, we predicted smaller Pt_x clusters show relatively higher activation energies. Moreover, our model does not consider the effect of other adsorbates from the ambient, such as hydroxyl group, water, etc. One can consider these factors to obtain a more realistic image of the catalytic activities of Pt clusters.

Also, our simulations on Co_3O_4 are just an initial investigation of Pt_x/Co_3O_4 catalysts. We only considered Pt_6 and Pt_1, while the activity of other Pt_x systems on Co_3O_4 remains to be studied.

References

[1] Hans-Joachim Freund et al. “CO Oxidation as a Prototypical Reaction for Heterogeneous Processes”. In: *Angewandte Chemie International Edition* 50.43 (2011), pp. 10064–10094.

[2] Arthur B. Ray and F. O. Anderegg. “The Oxidation of Carbon Monoxide by Passage with Oxygen or Air Through the Silent Discharge and over Ozone Decomposing Catalysts”. In: *Journal of the American Chemical Society* 43.5 (1921), pp. 967–978.

[3] R. Imbihl, M. P. Cox, and G. Ertl. “Kinetic oscillations in the catalytic CO oxidation on Pt(100): Experiments”. In: *The Journal of Chemical Physics* 84.6 (1986), pp. 3519–3534.

[4] S Wehner, F Baumann, and J Küppers. “Kinetic hysteresis in the CO oxidation reaction on Ir(111) surfaces”. In: *Chemical Physics Letters* 370.1 (2003), pp. 126–131.

[5] You Zhou, Zongyuan Wang, and Changjun Liu. “Perspective on CO oxidation over Pd-based catalysts”. In: *Catalysis Science Technology.* 5 (1 2015), pp. 69–81.

[6] Johan Gustafson et al. “The Role of Oxides in Catalytic CO Oxidation over Rhodium and Palladium”. In: *ACS Catalysis.* 8.5 (2018), pp. 4438–4445.

[7] Bjørk Hammer and Jens K. Nørskov. “Why gold is the noblest of all the metals”. In: *Nature* 376 (1995), pp. 238–240.

[8] M. Haruta et al. “Gold catalysts prepared by coprecipitation for low-temperature oxidation of hydrogen and of carbon monoxide”. In: *Journal of Catalysis* 115.2 (1989), pp. 301–309.

[9] Sergey N. Rashkeev et al. “Role of the nanoscale in catalytic CO oxidation by supported Au and Pt nanostructures”. In: *Physical Review B* 76 (3 2007), p. 035438.

[10] Geo Jong Kim, Dong Wook Kwon, and Sung Chang Hong. “Effect of Pt Particle Size and Valence State on the Performance of Pt/TiO2 Catalysts for CO Oxidation at Room Temperature”. In: *The Journal of Physical Chemistry C* 120.32 (2016), pp. 17996–18004.

[11] Hee Chan Song et al. “The effect of the oxidation states of supported oxides on catalytic activity: CO oxidation studies on Pt/cobalt oxide”. In: *Chem. Commun.* 55 (64 2019), pp. 9503–9506.

[12] Antonio Ruiz Puigdollers et al. “Increasing Oxide Reducibility: The Role of Metal/Oxide Interfaces in the Formation of Oxygen Vacancies”. In: *ACS Catalysis.* 7.10 (2017), pp. 6493–6513.

[13] Daniel Widmann et al. “How Temperature Affects the Mechanism of CO Oxidation on Au/TiO2: A Combined EPR and TAP Reactor Study of the Reactive Removal of TiO2 Surface Lattice Oxygen in Au/TiO2 by CO”. In: *ACS Catalysis* 6.8 (2016), pp. 5005–5011.

[14] Lichen Liu and Avelino Corma. “Metal Catalysts for Heterogeneous Catalysis: From Single Atoms to Nanoclusters and Nanoparticles”. In: *Chem. Rev.* 118.10 (2018), pp. 4981–5079.

[15] D.S. Afanasev et al. “High activity in CO oxidation of Ag nanoparticles supported on fumed silica”. In: *Catalysis Communications* 22 (2012), pp. 43–47.

[16] Nihong An et al. “Size Effects of Platinum Colloid Particles on the Structure and CO Oxidation Properties of Supported Pt/Fe2O3 Catalysts”. In: *The Journal of Physical Chemistry C* 117.41 (2013), pp. 21254–21262.

[17] Jin-Xun Liu et al. “Optimum Particle Size for Gold-Catalyzed CO Oxidation”. In: *The Journal of Physical Chemistry C* 122.15 (2018), pp. 8327–8340.

[18] Peter D. Clark et al. “Oxidation of CO in the presence of SO2 using gold supported on La2O3/TiO2 nanofibers”. In: *Catalysis Today* 207 (2013), pp. 212–219.

[19] Xuebi Du et al. “Controlled synthesis of Pd/CoOx–InOx nanofibers for low-temperature CO oxidation reaction”. In: *New J. Chem.* 43 (37 2019), pp. 14872–14882.

[20] Kamran Qadir et al. “Deactivation of Ru Catalysts under Catalytic CO Oxidation by Formation of Bulk Ru Oxide Probed with Ambient Pressure XPS”. In: *The Journal of Physical Chemistry C* 117.25 (2013), pp. 13108–13113.

[21] Hyun You Kim, Hyuck Mo Lee, and Graeme Henkelman. “CO Oxidation Mechanism on CeO2-Supported Au Nanoparticles”. In: *Journal of the American Chemical Society* 134.3 (2012), pp. 1560–1570.

[22] Zhi-Pan Liu, P. Hu, and Ali Alavi. “Catalytic Role of Gold in Gold-Based Catalysts: A Density Functional Theory Study on the CO Oxidation on Gold”. In: *Journal of the American Chemical Society* 124.49 (2002), pp. 14770–14779.

[23] Bor-Rong Chen et al. "Morphology and CO Oxidation Activity of Pd Nanoparticles on SrTiO3 Nanopolyhedra". In: *ACS Catalysis* 8.6 (2018), pp. 4751–4760.

[24] Ayman D. Allian et al. "Chemisorption of CO and Mechanism of CO Oxidation on Supported Platinum Nanoclusters". In: *Journal of the American Chemical Society* 133.12 (2011), pp. 4498–4517.

[25] Michael Sushchikh et al. "Size and pressure independent kinetics of CO oxidation on alumina-supported iridium nanoparticles". In: *International Journal of Chemical Kinetics* 40.12 (2008), pp. 826–830.

[26] Paul A. DeSario et al. "Low-temperature CO oxidation at persistent low-valent Cu nanoparticles on TiO2 aerogels". In: *Applied Catalysis B: Environmental* 252 (2019), pp. 205–213.

[27] Maximilian Lamoth et al. "Supported Ag Nanoparticles and Clusters for CO Oxidation: Size Effects and Influence of the Silver–Oxygen Interactions". In: *ACS Applied Nano Materials* 2.5 (2019), pp. 2909–2920.

[28] Hyunwoo Ha et al. "Catalytic CO Oxidation by CO-Saturated Au Nanoparticles Supported on CeO2: Effect of CO Coverage". In: *The Journal of Physical Chemistry C* 121.48 (2017), pp. 26895–26902.

[29] M. Haruta et al. "Low-Temperature Oxidation of CO over Gold Supported on TiO2, -Fe2O3, and Co3O4". In: *Journal of Catalysis* 144.1 (1993), pp. 175–192.

[30] Isabel Xiaoye Green et al. "Spectroscopic observation of dual catalytic sites during oxidation of CO on a Au/TiO catalyst". In: *Science (New York, N.Y.)* 333 (2011), pp. 736–739.

[31] Mingshu Chen and D. Wayne Goodman. "Catalytically Active Gold: From Nanoparticles to Ultrathin Films". In: *Accounts of Chemical Research* 39.10 (2006), pp. 739–746.

[32] Masatake Midorigaoka Haruta. "Size- and support-dependency in the catalysis of gold". In: *Catalysis Today* 36 (1997), pp. 153–166.

[33] Sang Hoon Joo et al. "Size Effect of Ruthenium Nanoparticles in Catalytic Carbon Monoxide Oxidation". In: *Nano Letters* 10.7 (2010), pp. 2709–2713.

[34] Kamran Qadir et al. "Intrinsic Relation between Catalytic Activity of CO Oxidation on Ru Nanoparticles and Ru Oxides Uncovered with Ambient Pressure XPS". In: *Nano Letters* 12.11 (2012), pp. 5761–5768.

[35] Da-bin QI et al. "Catalytic oxidation of CO on Pd38 cluster and Pd slab, a computational study". In: *Journal of Fuel Chemistry and Technology* 48.4 (2020), pp. 432–439.

[36] I. Stará, V. Nehasil, and V. Matolín. "The influence of particle size on CO oxidation on Pd/alumina model catalyst". In: *Surface Science* 331-333 (1995), pp. 173–177.

[37] Yingzhi Li et al. "CO oxidation over graphene supported palladium catalyst". In: *Applied Catalysis B: Environmental* 125 (2012), pp. 189–196.

[38] Giulia Spezzati et al. "CO oxidation by Pd supported on CeO2(100) and CeO2(111) facets". In: *Applied Catalysis B: Environmental* 243 (2019), pp. 36–46.

[39] Wasim Ullah Khan et al. "Catalytically active interfaces in titania nanorod-supported copper catalysts for CO oxidation". In: *Nano Research* 13 (2020), pp. 533–542.

[40] Andrew J. Maynes et al. "Electronic Metal–Support Interactions in the Activation of CO Oxidation over a Cu/TiO2 Aerogel Catalyst". In: *The Journal of Physical Chemistry C* 124.39 (2020), pp. 21491–21501.

[41] Wolf Vielstich, Arnold Lamm, and Hubert Gasteiger, eds. *Handbook of fuel cells. Fundamentals, technology, applications.* West Sussex: Wiley, 2003.

[42] Matteo Farnesi Camellone et al. "Catalytic Proton Dynamics at the Water/Solid Interface of Ceria-Supported Pt Clusters". In: *J. Am. Chem. Soc.* 138.36 (2016), pp. 11560–11567.

[43] Jan Kašpar, Paolo Fornasiero, and Neal Hickey. "Automotive Catalytic Converters: Current Status and some Perspectives". In: *Catal. Today.* 77.4 (2003), pp. 419–449.

[44] René Kopelent et al. "Enhanced Reducibility of the Ceria–Tin Oxide Solid Solution Modifies the CO Oxidation Mechanism at the Platinum–Oxide Interface". In: *ACS Catalysis.* 11.15 (2021), pp. 9435–9449.

[45] Mohamed N. Marei et al. "Comparative Study of the Catalytic Oxidation of Hydrocarbons on Platinum and Palladium Wires and Nanoparticles". In: *Energy Fuels* 36.4 (2022).

[46] Kwangjin An et al. “Enhanced CO Oxidation Rates at the Interface of Mesoporous Oxides and Pt Nanoparticles”. In: *Journal of the American Chemical Society* 135.44 (2013), pp. 16689–16696.

[47] Jiaojiao Song et al. “Dispersion and support dictated properties and activities of Pt/metal oxide catalysts in heterogeneous CO oxidation”. In: *Nano Research.* 14.12 (2021), pp. 4841–4847.

[48] Matteo Cargnello et al. “Control of Metal Nanocrystal Size Reveals Metal-Support Interface Role for Ceria Catalysts”. In: *Science* 341.6147 (2013), pp. 771–773.

[49] Zihao Li et al. “Catalytic oxidation of CO over Pt/Fe3O4 catalysts: Tuning O2 activation and CO adsorption”. In: *Frontiers of Environmental Science Engineering* 14 (2020).

[50] Leo DeRita et al. “Catalyst Architecture for Stable Single Atom Dispersion Enables Site-Specific Spectroscopic and Reactivity Measurements of CO Adsorbed to Pt Atoms, Oxidized Pt Clusters, and Metallic Pt Clusters on TiO2”. In: *Journal of the American Chemical Society* 139.40 (2017), pp. 14150–14165.

[51] Alejandro Peña-Torres et al. “Indirect mechanism of Au adatom diffusion on the Si(100) surface”. In: *Physical Review B* 105 (20 2022), p. 205411.

[52] Jin-Xia Liang et al. “Theoretical and Experimental Investigations on Single-Atom Catalysis: Ir1/FeOx for CO Oxidation”. In: *The Journal of Physical Chemistry C* 118.38 (2014), pp. 21945–21951.

[53] Botao Qiao et al. “Single-atom catalysis of CO oxidation using Pt1/FeOx”. In: *Nature Chemistry* 3.8 (2011), pp. 634–641.

[54] Jinxia Liang et al. “Catalytic ativities of single-atom catalysts for CO oxidation: Pt1/FeOx vs. Fe1/FeOx”. In: *Chinese Journal of Catalysis* 38.9 (2017), pp. 1566–1573.

[55] Joseph D. Kistler et al. “A Single-Site Platinum CO Oxidation Catalyst in Zeolite KLTL: Microscopic and Spectroscopic Determination of the Locations of the Platinum Atoms”. In: *Angewandte Chemie International Edition* 53.34 (2014), pp. 8904–8907.

[56] Son Hoang et al. “Activating low-temperature diesel oxidation by single-atom Pt on TiO2 nanowire array”. In: *Nature Communications.* 11.1 (2020), p. 1062.

[57] Florian Maurer et al. “Tracking the formation, fate and consequence for catalytic activity of Pt single sites on CeO2”. In: *Nat Catal* 3.10 (2020).

[58] U. Heiz et al. “Catalytic Oxidation of Carbon Monoxide on Monodispersed Platinum Clusters: Each Atom Counts”. In: *Journal of the American Chemical Society* 121.13 (1999), pp. 3214–3217.

[59] Qiuxia Cai, Xinde Wang, and Jian-guo Wang. “Distinctions between Supported Au and Pt Catalysts for CO Oxidation: Insights from DFT Study”. In: *The Journal of Physical Chemistry C* 117.41 (2013), pp. 21331–21336.

[60] Atsushi Beniya et al. “Insight for Designing Mass-Efficient Metal-Oxide-Supported Heterogeneous Catalyst from the Identification of the Catalytically Active Edge Sites Using Isotopically Labeled 13CO and 18O2”. In: *ACS Catalysis* 12.3 (2022), pp. 1977–1985.

[61] Sebastian Kaiser et al. “Cluster Catalysis with Lattice Oxygen: Tracing Oxygen Transport from a Magnetite (001) Support onto Small Pt Clusters”. In: *ACS Catalysis* 11.15 (2021), pp. 9519–9529.

[62] Ye Xu et al. “A first-principles investigation of the effect of Pt cluster size on CO and NO oxidation intermediates and energetics”. In: *Physical Chemistry Chemical Physics.* 10 (39 2008), pp. 6009–6018.

[63] Ho Viet Thang and Gianfranco Pacchioni. “CO Oxidation Promoted by a Pt4/TiO2 Catalyst: Role of Lattice Oxygen at the Metal/Oxide Interface”. In: *Catal Lett* 149.2 (2019), pp. 390–398.

[64] Noemi Bosio et al. “Interface Reactions Dominate Low-Temperature CO Oxidation Activity over Pt/CeO2”. In: *The Journal of Physical Chemistry C* 126.38 (2022), pp. 16164–16171.

[65] Na Li et al. “Kinetic study and the effect of particle size on low temperature CO oxidation over Pt/TiO2 catalysts”. In: *Applied Catalysis B: Environmental* 142-143 (2013), pp. 523–532.

[66] Sunyoung Oh et al. “Oxygen activation on the interface between Pt nanoparticles and mesoporous defective TiO2 during CO oxidation”. In: *J. Chem. Phys.* 151.23 (2019), p. 234716.

[67] Xiaomei Yu et al. “Observation of Temperature-dependent Kinetics for Catalytic CO Oxidation over TiO_2-supported Pt Catalysts”. In: *Chemical Physics. Letter.* 685 (2017), pp. 282–287.

[68] Hideto Yoshida, Hiroki Omote, and Seiji Takeda. "Oxidation and reduction processes of platinum nanoparticles observed at the atomic scale by environmental transmission electron microscopy". In: *Nanoscale* 6 (21 2014), pp. 13113–13118.

[69] Lan Zhang et al. "High Active Platinum Clusters on Titanium Dioxide Supports toward Carbon Monoxide Oxidation". In: *App. Catal. B* 266 (2020), p. 118629.

[70] Jun Ke et al. "Strong Local Coordination Structure Effects on Subnanometer PtO_x Clusters over CeO_2 Nanowires Probed by Low-Temperature CO Oxidation". In: *ACS Catalysis.* 5.9 (2015), pp. 5164–5173.

[71] Ye Xu, William A. Shelton, and William F. Schneider. "Thermodynamic Equilibrium Compositions, Structures, and Reaction Energies of Pt_xO_y (x = 13) Clusters Predicted from First Principles". In: *The Journal of Physical Chemistry . B* 110.33 (2006), pp. 16591–16599.

[72] Ye Xu, William A. Shelton, and William F. Schneider. "Effect of Particle Size on the Oxidizability of Platinum Clusters". In: *The Journal of Physical Chemistry . A* 110.17 (2006), pp. 5839–5846.

[73] Nisha Mammen et al. "Reversing Size-Dependent Trends in the Oxidation of Copper Clusters through Support Effects". In: *Eur. J. Inorg. Chem.* 2018.1 (2018), pp. 16–22.

[74] Ye Xu et al. "A First-Principles Investigation of the Effect of Pt Cluster Size on CO and NO Oxidation Intermediates and Energetics". In: *Physical Chemistry Chemical Physics.* 10.39 (2008), p. 6009.

[75] Andrii Tovt et al. "Ultimate Dispersion of Metallic and Ionic Platinum on Ceria". In: *J. Mater. Chem. A* 7 (21 2019), pp. 13019–13028.

[76] Yun Zhou et al. "Growth of Pt Particles on the Anatase TiO2 (101) Surface". In: *The Journal of Physical Chemistry C* 116.22 (2012), pp. 12114–12123.

[77] T. Schalow et al. "CO oxidation on partially oxidized Pd nanoparticles". In: *Journal of Catalysis* 242.1 (2006), pp. 58–70.

[78] Akhil S. Nair et al. "Relativistic Effects in Platinum Nanocluster Catalysis: A Statistical Ensemble-Based Analysis". In: *The Journal of Physical Chemistry .* 126.8 (2022), pp. 1345–1359.

[79] Honghong Wang, Taicheng An, and Annabella Selloni. "Effect of reducible oxide–metal cluster charge transfer on the structure and reactivity of adsorbed Au and Pt atoms and clusters on anatase TiO2". In: *The Journal of Chemical Physics* 146.18 (2017), p. 184703.

[80] Simon Bonanni et al. “Overcoming the Strong MetalSupport Interaction State: CO Oxidation on TiO2(110)-Supported Pt Nanoclusters”. In: *ACS Catalysis.* 1.4 (2011), pp. 385–389.

[81] M. Born and R. Oppenheimer. “Zur Quantentheorie der Molekeln”. In: *Annalen der Physik* 389.20 (1927), pp. 457–484.

[82] W. Kohn and L. J. Sham. “Self-Consistent Equations Including Exchange and Correlation Effects”. In: *Physical Review* 140 (4A 1965), A1133–A1138.

[83] David C. Langreth and M. J. Mehl. “Beyond the local-density approximation in calculations of ground-state electronic properties”. In: *Physical Review B* 28 (4 1983), pp. 1809–1834.

[84] John P. Perdew, Kieron Burke, and Matthias Ernzerhof. “Generalized Gradient Approximation Made Simple”. In: *Physical Review. Letter.* 77.18 (1996), pp. 3865–3868.

[85] A. D. Becke. “Density-functional exchange-energy approximation with correct asymptotic behavior”. In: *Physical Review. A* 38 (6 1988), pp. 3098–3100.

[86] Yue Wang and John P. Perdew. “Spin scaling of the electron-gas correlation energy in the high-density limit”. In: *Physical Review B* 43 (11 1991), pp. 8911–8916.

[87] John P. Perdew, Kieron Burke, and Yue Wang. “Generalized gradient approximation for the exchange-correlation hole of a many-electron system”. In: *Physical Review B* 54 (23 1996), pp. 16533–16539.

[88] Hendrik J. Monkhorst and James D. Pack. “Special points for Brillouin-zone integrations”. In: *Physical Review B* 13 (12 1976), pp. 5188–5192.

[89] Richard M Martin. *Electronic structure: basic theory and practical methods.* 2020. ISBN: 9780511805769.

[90] D. R. Hamann, M. Schlüter, and C. Chiang. “Norm-Conserving Pseudopotentials”. In: *Physical Review. Letter.* 43 (20 1979), pp. 1494–1497.

[91] Matteo Cococcioni and Stefano de Gironcoli. “Linear response approach to the calculation of the effective interaction parameters in the LDA + U method”. In: *Physical Review B* 71 (3 2005), p. 035105.

[92] Marçal Capdevila-Cortada, Zbigniew Łodziana, and Núria López. “Performance of DFT+U Approaches in the Study of Catalytic Materials”. In: *ACS Catalysis.* 6.12 (2016), pp. 8370–8379.

[93] Aron J. Cohen, Paula Mori-Sánchez, and Weitao Yang. "Insights into Current Limitations of Density Functional Theory". In: *Science* 321.5890 (2008), pp. 792–794. DOI: 10.1126/science.1158722. eprint: https://www.science.org/doi/pdf/10.1126/science.1158722. URL: https://www.science.org/doi/abs/10.1126/science.1158722.

[94] Jürgen Gräfenstein, Elfi Kraka, and Dieter Cremer. "The impact of the self-interaction error on the density functional theory description of dissociating radical cations: Ionic and covalent dissociation limits". In: *The Journal of Chemical Physics* 120.2 (2004), pp. 524–539.

[95] Marcus Lundberg and Per E. M. Siegbahn. "Quantifying the effects of the self-interaction error in DFT: When do the delocalized states appear?" In: *The Journal of Chemical Physics* 122.22 (2005), p. 224103.

[96] Adrienn Ruzsinszky et al. "Density functionals that are one- and two- are not always many-electron self-interaction-free, as shown for H2+, He2+, LiH+, and Ne2+". In: *The Journal of Chemical Physics* 126.10 (2007), p. 104102.

[97] V. I. Anisimov et al. "Density-functional theory and NiO photoemission spectra". In: *Physical Review B* 48 (23 1993), pp. 16929–16934.

[98] S. L. Dudarev et al. "Electron-energy-loss spectra and the structural stability of nickel oxide: An LSDA+U study". In: *Physical Review B* 57 (3 1998), pp. 1505–1509.

[99] Yaroslava Lykhach et al. "Quantitative Analysis of the Oxidation State of Cobalt Oxides by Resonant Photoemission Spectroscopy". In: *The Journal of Physical Chemistry . Letter.* 10.20 (2019), pp. 6129–6136.

[100] Zhenpeng Hu and Horia Metiu. "Choice of U for DFT+U Calculations for Titanium Oxides". In: *The Journal of Physical Chemistry C* 115.13 (2011), pp. 5841–5845.

[101] R. Car and M. Parrinello. "Unified Approach for Molecular Dynamics and Density-Functional Theory". In: *Physical Review. Letter.* 55 (22 1985), pp. 2471–2474.

[102] David J. Wales and Jonathan P. K. Doye. "Global Optimization by Basin-Hopping and the Lowest Energy Structures of Lennard-Jones Clusters Containing up to 110 Atoms". In: *The Journal of Physical Chemistry A* 101.28 (1997), pp. 5111–5116.

[103] W. D. Luedtke and Uzi Landman. "Structure and Thermodynamics of Self-Assembled Monolayers on Gold Nanocrystallites". In: *The Journal of Physical Chemistry B* 102.34 (1998), pp. 6566–6572.

[104] Lasse B. Vilhelmsen and Bjørk Hammer. "A Genetic Algorithm for First Principles Global Structure Optimization of Supported Nano Structures". In: *The Journal of Physical Chemistry Letters* 141.4 (2014), p. 044711.

[105] Ask Hjorth Larsen et al. "The Atomic Simulation Environment—a Python Library for working with Atoms". In: *Journal of Physics: Condensed Matter* 29.27 (2017), p. 273002.

[106] Lasse B. Vilhelmsen and Bjørk Hammer. "Systematic Study of Au_6 to Au_{12} Gold Clusters on MgO(100) F Centers Using Density-Functional Theory". In: *Physical Review. Letter.* 108.12 (2012), p. 126101.

[107] F. Rieboldt et al. "Nucleation and Growth of Pt Nanoparticles on Reduced and Oxidized Rutile TiO_2 (110)". In: *The Journal of Chemical Physics.* 141.21 (2014), p. 214702.

[108] Thomas Reichenbach et al. "Effects of Gas-Phase Conditions and Particle Size on the Properties of Cu(111)-Supported ZnyOx Particles Revealed by Global Optimization and Ab Initio Thermodynamics". In: *The Journal of Chemical Physics. C* 123.51 (2019), pp. 30903–30916.

[109] Karsten Reuter and Matthias Scheffler. "Composition, Structure, and Stability of RuO_2(110) as a Function of Oxygen Pressure". In: *Physical Review B* 65.3 (2001), p. 035406.

[110] D.A. McQuarrie and M.Q.D. A. *Statistical Mechanics.* Chemistry Series. 1975. ISBN: 9780060443665.

[111] Thomas C. Allison. *NIST-JANAF Thermochemical Tables - SRD 13.* 2013. DOI: 10.18434/T42S31.

[112] John A. Keith et al. "Combining Machine Learning and Computational Chemistry for Predictive Insights Into Chemical Systems". In: *Chemical Reviews* 121.16 (2021), pp. 9816–9872.

[113] Daniel Sheppard, Rye Terrell, and Graeme Henkelman. "Optimization methods for finding minimum energy paths". In: *The Journal of Chemical Physics* 128.13 (2008), p. 134106.

[114] Bruce J Berne, Giovanni Ciccotti, and David F Coker. *Classical and Quantum Dynamics in Condensed Phase Simulations.* 1998.

[115] Graeme Henkelman, Blas P. Uberuaga, and Hannes Jónsson. "A climbing image nudged elastic band method for finding saddle points and minimum energy paths". In: *The Journal of Chemical Physics* 113.22 (2000), pp. 9901–9904.

[116] Paolo Giannozzi et al. "QUANTUM ESPRESSO: a Modular and Open-source Software Project for Quantum Simulations of Materials". In: *J. Phys.: Condens. Matter* 21.39 (2009), p. 395502.

[117] N. W. Ashcroft and N. D. Mermin. *Solid State Physics*. Holt-Saunders, 1976.

[118] J. R. McBride et al. "Growth and Characterization of Reactively Sputtered Thin-film Platinum Oxides". In: *International Journal of Applied Physics* . 69.3 (1991), pp. 1596–1604.

[119] K.-J. Range et al. "-PtO_2: High Pressure Synthesis of Single Crystals and Structure Refinement". In: *Materials Research Bulletin.* 22.11 (1987), pp. 1541–1547.

[120] Charles Kittel. 8th ed. Wiley, 2004. ISBN: 9780471415268.

[121] Ricardo K. Nomiyama, Maurício J. Piotrowski, and Juarez L. F. Da Silva. "Bulk structures of PtO and PtO_2 from Density Functional Calculations". In: *Physical Review B.* 84.10 (2011), p. 100101.

[122] George Yan and Philippe Sautet. "Surface Structure of Co_3O_4 (111) under Reactive Gas-Phase Environments". In: *ACS Catalysis.* 9.7 (2019), pp. 6380–6392.

[123] P W Tasker. "The stability of ionic crystal surfaces". In: *Journal of Physics C: Solid State Physics* 12.22 (1979), pp. 4977–4984.

[124] Donato Fantauzzi et al. "Development of a ReaxFF Potential for Pt–O Systems describing the Energetics and Dynamics of Pt-oxide Formation". In: *Physical Chemistry Chemical Physics.* 16.42 (2014), pp. 23118–23133.

[125] Manh-Thuong Nguyen, Matteo Farnesi Camellone, and Ralph Gebauer. "On the Electronic, Structural, and Thermodynamic Properties of Au Supported on $\alpha - Fe_2O_3$ Surfaces and their Interaction with CO". In: *Chemical Physics.* 143.3 (2015), p. 034704.

[126] Satish K Gupta, Bianca M Nappi, and Karl A Gingerich. "Mass spectrometric study of the stabilities of the gaseous molecules diatomic platinum and platinum-yttrium". In: *Inorganic Chemistry* 20.4 (1981), pp. 966–969.

[127] D. Majumdar, Dingguo Dai, and K. Balasubramanian. "Theoretical Study of the Electronic States of Platinum Trimer (Pt_3)". In: *Chemical Physics.* 113.18 (2000), pp. 7919–7927.

[128] Ali Sebetci and Ziya B. Güvenç. "Energetics and Structures of Small Clusters: Pt_N, N=2–21". In: *Surface Science.* 525.1 (2003), pp. 66–84.

[129] Lauro Oliver Paz-Borbón et al. "2D–3D Structural Transition in Subnanometer Pt_N Clusters Supported on $CeO_2(111)$". In: *Physical Chemistry Chemical Physics.* 19 (27 2017), pp. 17845–17855.

[130] Li Xiao and Lichang Wang. "Structures of Platinum Clusters: Planar or Spherical?" In: *The Journal of Physical Chemistry . A* 108.41 (2004), pp. 8605–8614.

[131] Christian Kerpal et al. "Structures of Platinum Oxide Clusters in the Gas Phase". In: *The Journal of Physical Chemistry . A* 117.6 (2013), pp. 1233–1239.

[132] Alexios Chatzigoulas et al. "NanoCrystal: A Web-Based Crystallographic Tool for the Construction of Nanoparticles Based on Their Crystal Habit". In: *Journal of Chemical Information and Modeling.* 58.12 (2018), pp. 2380–2386.

[133] You Han, Chang-jun Liu, and Qingfeng Ge. "Interaction of Pt Clusters with the Anatase $TiO_2(101)$ Surface: A First Principles Study". In: *The Journal of Physical Chemistry .* 110.14 (2006), pp. 7463–7472.

[134] De-en Jiang, Steven H. Overbury, and Sheng Dai. "Structures and Energetics of Pt Clusters on TiO_2: Interplay between Metal–Metal Bonds and Metal–Oxygen Bonds". In: *The Journal of Physical Chemistry . C* 116.41 (2012), pp. 21880–21885.

[135] Yoshihide Watanabe et al. "Size-Dependent Catalytic Activity and Geometries of Size-selected Pt Clusters on $TiO_2(110)$ Surfaces". In: *Catalysis Science and Technology.* 1 (8 2011), pp. 1490–1495.

[136] Raina Wanbayor and Vithaya Ruangpornvisuti. "A periodic DFT Study on Binding of Pd, Pt and Au on the Anatase $TiO_2(001)$ Surface and Adsorption of CO on the TiO_2 Surface-Supported Pd, Pt and Au". In: *Applied Surface Science.* 258.7 (2012), pp. 3298–3301.

[137] Rajkumar Jana et al. "Pt/Co_3O_4 Surpasses Benchmark Pt/C: An Approach Toward Next Generation Hydrogen Evolution Electrocatalyst". In: *ACS Applied Energy Materials.* 2.8 (2019), pp. 5613–5621.

[138] N. Seriani et al. "Density Functional Theory study of Platinum Oxides: From Infinite Crystals to Nanoscopic Particles". In: *Physical Review B* 76.15 (2007), p. 155421.

[139] Yaroslava Lykhach et al. "Interplay Between the Metal-Support Interaction and Stability in $Pt/Co_3O_4(111)$ Model Catalysts". In: *The Journal of Physical Chemistry Letters* 6 (45 2018), pp. 23078–23086.

[140] L. K. Ono et al. “Formation and Thermal Stability of Platinum Oxides on Size-Selected Platinum Nanoparticles: Support Effects”. In: *The Journal of Physical Chemistry . C* 114.50 (2010), pp. 22119–22133.

[141] Luis K. Ono et al. “Oxygen Chemisorption, Formation, and Thermal Stability of Pt Oxides on Pt Nanoparticles Supported on SiO_2 /Si(001): Size Effects”. In: *The Journal of Physical Chemistry . C* 115.34 (Sept. 1, 2011), pp. 16856–16866.

[142] Eero Holmström et al. “Hydration Structure of Brookite TiO_2 (210)”. In: *The Journal of Physical Chemistry . C* 121.38 (2017), pp. 20790–20801.

[143] Graeme Henkelman, Andri Arnaldsson, and Hannes Jónsson. “A Fast and Robust Algorithm for Bader Decomposition of Charge Density”. In: *Computational Materials Science.* 36.3 (2006), pp. 354–360.

[144] Salai Cheettu Ammal and Andreas Heyden. “Modeling the Noble Metal/TiO_2 (110) Interface with Hybrid DFT Functionals: A Periodic Electrostatic Embedded Cluster Model Study”. In: *Chemical Physics.* 133.16 (2010), p. 164703.

[145] Jonas Ø. Hansen et al. “Enhanced Bonding of Silver Nanoparticles on Oxidized TiO_2 (110)”. In: *The Journal of Physical Chemistry . C* 114.40 (2010), pp. 16964–16972.

[146] B. Hammer and J.K. Nørskov. “Electronic factors determining the reactivity of metal surfaces”. In: *Surface Science* 343.3 (1995), pp. 211–220.

[147] B. Hammer and J. K. Norskov. “Why gold is the noblest of all the metals”. In: *Nature* 376.6537 (1995), pp. 238–240.

[148] B. Hammer and J.K. Nørskov. “Theoretical surface science and catalysis—calculations and concepts”. In: *Impact of Surface Science on Catalysis*. Vol. 45. Advances in Catalysis. Academic Press, 2000, pp. 71–129.

[149] Hsin-Yi Tiffany Chen, Sergio Tosoni, and Gianfranco Pacchioni. “Adsorption of Ruthenium Atoms and Clusters on Anatase TiO2 and Tetragonal ZrO2(101) Surfaces: A Comparative DFT Study”. In: *The Journal of Physical Chemistry C* 119.20 (2015), pp. 10856–10868.

[150] Zihao Li et al. “Catalytic oxidation of CO over Pt/Fe3O4 catalysts: Tuning O2 activation and CO adsorption”. In: *Frontiers of Environmental Science Engineering.* 14.4 (2020), p. 65.

[151] Piero Ferrari et al. “Controlling the Adsorption of Carbon Monoxide on Platinum Clusters by Dopant-Induced Electronic Structure Modification”. In: *Angewandte Chemie International Edition* 55.37 (2016), pp. 11059–11063.

[152] Benjamin Demirdjian et al. “CO and O $_2$ Adsorption and CO Oxidation on Pt Nanoparticles by Indirect Nanoplasmonic Sensing”. In: *ACS Omega* 6.20 (2021), pp. 13398–13405.

[153] Roland Bliem et al. “Dual role of CO in the stability of subnano Pt clusters at the Fe $_3$ O $_4$ (001) surface”. In: *Proceedings of the National Academy of Sciences of the United States of America.* 113.32 (2016), pp. 8921–8926.

[154] G. S. Blackman et al. “Mix of Molecular Adsorption Sites Detected for Disordered CO on Pt(111) by Diffuse Low-Energy Electron Diffraction”. In: *Physical Review. Letter.* 61.20 (1988), pp. 2352–2355.

[155] G. T. Kasun Kalhara Gunasooriya and Mark Saeys. “CO Adsorption Site Preference on Platinum: Charge Is the Essence”. In: *ACS Catalysis.* 8.5 (2018), pp. 3770–3774.

[156] Fuzhu Liu et al. “CO Oxidation over Strained Pt(100) Surface: A DFT Study”. In: *The Journal of Physical Chemistry . C* 119.27 (2015), pp. 15500–15505.

[157] L. O. Paz-Borbon et al. “Chemisorption of CO and H on Pd, Pt and Au nanoclusters: a DFT approach”. In: *European Physical Journal D* 52.1-3 (2009), pp. 131–134.

[158] Hongwei Gao. “CO oxidation mechanism on the -Al2O3 supported single Pt atom: First principle study”. In: *Applied Surface Science* 379 (2016), pp. 347–357.

[159] P. Ferstl et al. “Adsorption and Activation of CO on Co3O4(111) Thin Films”. In: *The Journal of Physical Chemistry C* 119.29 (2015), pp. 16688–16699.

[160] Peter Broqvist, Itai Panas, and Hans Persson. “A DFT Study on CO Oxidation over Co3O4”. In: *Journal of Catalysis* 210.1 (2002), pp. 198–206.

[161] Sebastian Kaiser et al. “Cluster Catalysis with Lattice Oxygen: Tracing Oxygen Transport from a Magnetite (001) Support onto Small Pt Clusters”. In: *ACS Catalysis.* 11.15 (2021), pp. 9519–9529.

[162] Alexis Sangnier et al. “Thermokinetic and Spectroscopic Mapping of Carbon Monoxide Adsorption on Highly Dispersed Pt/-Al2O3”. In: *ACS Catalysis.* 11.21 (2021), pp. 13280–13293.

[163] Jagdeep Singh et al. “Electronic structure of alumina-supported monometallic Pt and bimetallic PtSn catalysts under hydrogen and carbon monoxide environment”. In: *Physical Chemistry Chemical Physics.* 12.21 (2010), p. 5668.

[164] Prasenjit Ghosh, Matteo Farnesi Camellone, and Stefano Fabris. “Fluxionality of Au Clusters at Ceria Surfaces during CO Oxidation: Relationships among Reactivity, Size, Cohesion, and Surface Defects from DFT Simulations”. In: *The Journal of Physical Chemistry . Letter.* 4.14 (2013), pp. 2256–2263.

[165] Hu Zhou, Xianlang Chen, and Jianguo Wang. “CO oxidation over supported Pt clusters at different CO coverage”. In: *International Journal of Quantum Chemistry* 116.12 (2016), pp. 939–944.

[166] Yubing Lu et al. “Origin of the High CO Oxidation Activity on CeO2 Supported Pt Nanoparticles: Weaker Binding of CO or Facile Oxygen Transfer from the Support?” In: *ChemCatChem* 12.6 (2020), pp. 1726–1733.

[167] Xiaomei Yu et al. “Observation of temperature-dependent kinetics for catalytic CO oxidation over TiO2-supported Pt catalysts”. In: *Chemical Physics Letters* 685 (2017), pp. 282–287.

[168] Philomena Schlexer et al. “CO Oxidation on a Au/TiO $_2$ Nanoparticle Catalyst via the Au-Assisted Mars–van Krevelen Mechanism”. In: *ACS Catalysis.* 8.7 (2018), pp. 6513–6525.

[169] M.G. Sanchez and J.L. Gazquez. “Oxygen vacancy model in strong metal-support interaction”. In: *Journal of Catalysis* 104.1 (1987), pp. 120–135.

[170] Hsin-Yi Tiffany Chen, Sergio Tosoni, and Gianfranco Pacchioni. “Adsorption of Ruthenium Atoms and Clusters on Anatase TiO $_2$ and Tetragonal ZrO $_2$ (101) Surfaces: A Comparative DFT Study”. In: *The Journal of Physical Chemistry . C* 119.20 (2015), pp. 10856–10868.

[171] Linxi Wang et al. “Emergent Behavior in Oxidation Catalysis over Single-Atom Pd on a Reducible CeO2 Support via Mixed Redox Cycles”. In: *ACS Catalysis* 12.20 (2022), pp. 12927–12941.

[172] Hui Wang et al. "Surpassing the single-atom catalytic activity limit through paired Pt-O-Pt ensemble built from isolated Pt1 atoms". In: *Nature Communications.* 10.1 (2019), p. 3808.

[173] Selin Bac and Shaama Mallikarjun Sharada. "CO Oxidation with Atomically Dispersed Catalysts: Insights from the Energetic Span Model". In: *ACS Catalysis.* (2022), pp. 2064–2076.

[174] Yan-Yang Qin and Ya-Qiong Su. "A DFT Study on Heterogeneous Pt/CeO2(110) Single Atom Catalysts for CO Oxidation". In: *ChemCatChem* 13.17 (2021), pp. 3857–3863.

[175] Ya-Qiong Su et al. "Theoretical Approach To Predict the Stability of Supported Single-Atom Catalysts". In: *ACS Catalysis* 9.4 (2019), pp. 3289–3297.

[176] Xiaoyang Wang et al. "Interplay between invasive single atom Pt and native oxygen vacancy in rutile TiO2(110) surface: A theoretical study". In: *Nano Research.* 15.1 (2022), pp. 669–676.

[177] Yang Lou and Jingyue Liu. "CO Oxidation on Metal Oxide Supported Single Pt atoms: The Role of the Support". In: *Industrial and Engineering Chemistry Research* 56.24 (2017), pp. 6916–6925.

[178] Melanie Moses-DeBusk et al. "CO Oxidation on Supported Single Pt Atoms: Experimental and ab Initio Density Functional Studies of CO Interaction with Pt Atom on -Al2O3 (010) Surface". In: *J. Am. Chem. Soc.* 135.34 (2013), pp. 12634–12645.

[179] Melanie Moses-DeBusk et al. "CO Oxidation on Supported Single Pt Atoms: Experimental and ab Initio Density Functional Studies of CO Interaction with Pt Atom on -Al2O3(010) Surface". In: *Journal of the American Chemical Society* 135.34 (2013), pp. 12634–12645.

[180] Xueyuan Wu, Annabella Selloni, and Saroj K. Nayak. "First principles study of CO oxidation on TiO2(110): The role of surface oxygen vacancies". In: *The Journal of Chemical Physics* 120.9 (2004), pp. 4512–4516.

[181] Atsushi Beniya et al. "CO oxidation activity of non-reducible oxide-supported mass-selected few-atom Pt single-clusters". In: *Nature Communications.* 11.1 (2020), p. 1888.

[182] T. Bligaard et al. "The Brønsted–Evans–Polanyi relation and the volcano curve in heterogeneous catalysis". In: *Journal of Catalysis* 224.1 (2004), pp. 206–217.

[183] Francis Doherty et al. “Nanocluster and single-atom catalysts for thermocatalytic conversion of CO and CO2”. In: *Catal. Sci. Technol.* 10 (17 2020), pp. 5772–5791.

A Appendix

A sample of the GA input file in combination with Quantum ESPRESSO on a parallel machine, using communication via sockets is as follow:

ASE input file for generating the starting population

```
from ase.ga.data import PrepareDB
from ase import Atoms
from ase.lattice.cubic import FaceCenteredCubic
from ase.ga.startgenerator import StartGenerator
from ase.ga.utilities import closest_distances_generator
from ase.ga.utilities import get_all_atom_types
from ase.constraints import FixAtoms
import numpy as np

db_file = 'gadb.db'

slab=Atoms(cell=[15.0,15.0,15.0], pbc=[1,1,1])

p0 = np.array([5.0, 5.0, 5.0])
v1 = np.array([3.5, 0.0, 0.0])
v2 = np.array([0.0, 3.5, 0.0])
v3 = np.array([0.0, 0.0, 3.5])

atom_numbers = 6 * [78]

cd = closest_distances_generator(atom_numbers=atom_numbers,
                                 ratio_of_covalent_radii=0.7)

sg = StartGenerator(slab,
                    atom_numbers=atom_numbers,
                    closest_allowed_distances=cd,
                    box_to_place_in=[p0, [v1, v2, v3]])

population_size = 20
starting_population = [sg.get_new_candidate() for i in range(population_size)]

d = PrepareDB(db_file_name=db_file,
              simulation_cell=slab,
              stoichiometry=atom_numbers)

for a in starting_population:
    d.add_unrelaxed_candidate(a)
```

ASE input file for relaxing the candidates

```
from random import random
from ase.io import write
import time
from ase.ga.data import DataConnection
from ase.ga.population import Population
from ase.ga.standard_comparators import InteratomicDistanceComparator
from ase.ga.cutandsplicepairing import CutAndSplicePairing
from ase.ga.offspring_creator import OperationSelector
from ase.ga.standardmutations import MirrorMutation
from ase.ga.standardmutations import RattleMutation
from ase.ga.standardmutations import PermutationMutation
from ase.ga.utilities import closest_distances_generator
from ase.ga.utilities import get_all_atom_types

def jtg(job_prefix, traj_file, job_id):
    s = '#!/bin/bash\n'
    s += '#SBATCH --nodes=1\n'
    s += '#SBATCH --ntasks-per-node=4\n'
    s += '#SBATCH --ntasks-per-socket=4\n'
    s += '#SBATCH --cpus-per-task=8\n'
    s += '#SBATCH --gres=gpu:1\n'
    s += '#SBATCH --mem=60000MB\n'
    s += '#SBATCH --time 12:00:00\n'
    s += '#SBATCH --job-name={0}\n'.format(job_prefix)
    s += '#SBATCH -A Project name\n'
    s += '#SBATCH -p m100_usr_prod\n'
    s += 'module load profile/chem-phys\n'
    s += 'module load python/3.8.2\n'

    s += 'export OMP_NUM_THREADS=2\n'
    s += 'python3 local_calc.py {0} {1}\n'.format(traj_file, job_id)
    return s

population_size = 20
mutation_probability = 0.3
da = DataConnection('gadb.db')
tmp_folder = 'tmp_folder'
pbs_run = PBSQueueRun_SP(da,
                         tmp_folder=tmp_folder,
                         job_prefix='SOCKET',
                         n_simul=10,
                         job_template_generator=jtg,
                         qsub_command='sbatch',
                         qstat_command='squeue')

atom_numbers_to_optimize = da.get_atom_numbers_to_optimize()
n_to_optimize = len(atom_numbers_to_optimize)
slab = da.get_slab()
all_atom_types = get_all_atom_types(slab, atom_numbers_to_optimize)
blmin = closest_distances_generator(all_atom_types,
                                    ratio_of_covalent_radii=0.7)

comp = InteratomicDistanceComparator(n_top=n_to_optimize,
                                     pair_cor_cum_diff=0.015,
                                     pair_cor_max=0.7,
```

```
                                    dE=0.02,
                                    mic=False)
pairing = CutAndSplicePairing(slab, n_to_optimize, blmin)
mutations = OperationSelector([1., 1., 0.],
                              [MirrorMutation(blmin, n_to_optimize),
                               RattleMutation(blmin, n_to_optimize),
                               PermutationMutation(n_to_optimize)])

print('N. of unrelaxed: ', da.get_number_of_unrelaxed_candidates())
while (da.get_number_of_unrelaxed_candidates() > 0 and
       not pbs_run.enough_jobs_running()):
    print('N unrelaxed: ', da.get_number_of_unrelaxed_candidates())
    print('N running  : ', pbs_run.number_of_jobs_running())
    a = da.get_an_unrelaxed_candidate()
    pbs_run.relax(a)
    time.sleep(1.)

population = Population(data_connection=da,
                        population_size=population_size,
                        comparator=comp)

print('Len curr pop:', len(population.get_current_population()))
while (not pbs_run.enough_jobs_running() and len(population.get_current_population()) > 2):
    a1, a2 = population.get_two_candidates()
    a3, desc = pairing.get_new_individual([a1, a2])
    if a3 is None:
        continue
    da.add_unrelaxed_candidate(a3, description=desc)

    if random() < mutation_probability:
        a3_mut, desc = mutations.get_new_individual([a3])
        if a3_mut is not None:
            da.add_unrelaxed_step(a3_mut, desc)
            a3 = a3_mut
    print('N running  : ', pbs_run.number_of_jobs_running())
    pbs_run.relax(a3)
    time.sleep(1.)
print('Done')
write('all_candidates.traj', da.get_all_relaxed_candidates())
```

ASE input file to run a GA calculation with QUANTUM ESPRESSO on a parallel machine via sockets

```
from ase.optimize import BFGS
from ase.calculators.espresso import Espresso
from ase.io import read, write
from ase.ga.relax_attaches import VariansBreak
from ase.calculators.socketio import SocketIOCalculator
import sys

fname = sys.argv[1]
job_id = sys.argv[2]
print('Now relaxing {0}'.format(fname))
print('Job_ID: {0}'.format(job_id))
a = read(fname)
label_file = 'espresso_{0}'.format(job_id)
tmp_qe = 'tmp_{0}'.format(job_id)
print('tmp dir: {0}'.format(tmp_qe))
pseudopotentials = {'Pt': 'pt_pbe_v1.4.uspp.F.UPF'}

input_data = { 'control': {'restart_mode' : 'from_scratch',
                           'pseudo_dir' : './pseudo',
                           'outdir' : tmp_qe,
                           'max_seconds' : 13500},
               'electrons': {'mixing_beta': 0.7,
                             'electron_maxstep': 100,
                             'conv_thr' : 1.0e-07,
                             'scf_must_converge': False},
               'system': {'ecutwfc': 25,
                          'ecutrho': 200,
                          'occupations' : 'smearing',
                          'smearing': 'mv',
                          'degauss': 0.01}}

unixsocket = 'ase_espresso_{0}'.format(job_id)
command = ('mpirun -gpu --map-by socket:PE=2 --rank-by core
            pw.x < espresso_{0}.pwi --ipi {unixsocket}:UNIX
            espresso_{0}.pwo'.format(job_id,unixsocket=unixsocket))

espresso_calc = Espresso(command=command,
                         pseudopotentials=pseudopotentials,
                         label=label_file, stress=False, tprnfor=True, input_data=input_data)

dyn = BFGS(a, trajectory='opt_{0}.traj'.format(job_id), logfile='opt_{0}.log'.format(job_id))
with SocketIOCalculator(espresso_calc, log=sys.stdout,
                        unixsocket=unixsocket) as socket_calc:
     a.calc = socket_calc
     vb = VariansBreak(a, dyn)
     dyn.attach(vb.write)
     dyn.run(fmax=0.05, steps=300)
     socket_calc.close()

a.info['key_value_pairs']['raw_score'] = -a.get_potential_energy()
write(fname[:-5] + '_done.traj', a)
print('Done relaxing {0}'.format(fname))
```